White Beam Synchrotron X-ray Topography and micro-Raman Spectroscopy Characterization of Crystal Materials

A Thesis

Submitted to
Dublin City University

For the degree of
Doctor of Philosophy (Ph.D.)

By
Weimin Chen, Ph.D., *M. Eng., B. Eng.*

School of Electronic Engineering
Dublin City University

Research Supervisor

Dr. Patrick J. McNally, *BE, ScM, PhD, CPhys, MInstP, CEng, MIEI, SMIEEE*

May 2003

DECLARATION

I hereby certify that this material, which I now submit for assessment on the programme of study leading to the award of Ph.D. is entirely my own work and has not been taken from the work of others save and to the extent that such work has been cited and acknowledged within the text of my work.

Signed: _____   ID No.: 99145075

Weimin Chen

Date: 10 May 2003

ACKNOWLEDGEMENTS

CONTENTS

3 WHITE BEAM SYNCHROTRON X-RAY TOPOGRAPHY EXPERIMENTAL RESULTS   57

4 RAMAN SPECTROSCOPY   91

White Beam Synchrotron X-ray Topography and micro-Raman Spectroscopy Characterization of Crystal Materials

Weimin Chen

Abstract

The White Beam Synchrotron X-Ray Topography (WBSXRT) technique was used to assess sapphire wafer quality. The dislocation distribution, dislocation density, Burgers vectors of selected dislocations and stacking faults in the sapphire wafers were studied. A correlation between the sapphire quality and its performance as an X-ray backscattering mirror was established in this study. The results reveal the high quality of the inspected Heat-Exchanger Method produced sapphire wafers and their subsequent improved performance as Bragg backscattering mirrors.

Wing tilts in the epitaxial lateral overgrowth (ELO) of GaN on sapphire substrates using a SiO_2 mask were observed and measured with the WBSXT method. The wing tilt increases as the fill factor (ratio of stripe opening width to stripe period) increases and asymmetric wing tilts are observed in all samples with different fill factors. The crystal misorientation in the window regions and beneath the seed layer is approximately an order of magnitude less than the wing tilt.

A regular wave-like two dimensional stress distribution was observed in the ELO GaN epilayer by using high resolution micro-Raman spectroscopy (μRS). The average compressive stress in the ELO GaN was around 450~460 MPa, and the coalesced region between two ELO wings usually exhibits a lower compressive stress by about 60 MPa compared to the average stress in the epilayer. The ELO process increases the residual compressive stress in the GaN epilayer.

The stress in both device silicon cap layers and the underlying $Si_{1-x}Ge_x$ virtual substrates was characterized with μRS using both the 488 nm Ar^+ visible laser and 325 nm HeCd UV laser sources. The $Si_{0.70}Ge_{0.30}$ capping layer at the virtual substrate is fully unstrained as the result of formation two perpendicular <110> misfit crosshatches, while the top silicon cap layer is in extremely high tension with a measured tensile stress of 2.4 GPa.

1 X-Ray Topography

1.1 Description of X-ray topography

X-ray topography (XRT) is a non-destructive X-ray imaging technique based on the difference in reflecting power (according to Bragg's law $\lambda = 2\ d_{hkl}\ \sin\theta$, with λ = X-ray wavelength, d_{hkl} = lattice plane spacing, θ= Bragg angle) between perfect and imperfect crystal regions [1]. It is suitable for studying the character and distribution of crystallographic defects in large, nearly perfect, single crystal materials. Defects, such as dislocations, typically appear as dark lines in topographs [2], as the curved crystal planes around a defect reflect the divergent rays that are not reflected by the surrounding perfect region, thus the integrated intensity around the defects is larger than elsewhere. The principle is shown schematically in Fig. 1.1. As an example, Fig. 1.2 shows two topographs corresponding to two premium grade sapphire wafers produced with the Heat-Exchanger Method (HEM) [3-4] at Crystal System Inc. (CSI). These two topographs were obtained from two wafers cut from different boules of sapphire with the white beam synchrotron large area back reflection method at Beamline F1, HASYLAB (Hamburg Synchrotron Radiation Laboratory), DESY (Deutsches Elektronen-Synchrotron). In the topograph of the first HEM sapphire wafer, many curved dislocations were observed, while in the second HEM wafer, no dislocations were detected at all. Despite the fact that many dislocations exist in the first sapphire wafer, its quality is still quite good compared to the usual commercially available sapphire wafers [4-5].

The contrast of defects (imperfections) is affected by several physical factors in the experiment which include x-ray wavelength, the amount of collimation, specimen absorption, the scattering factor of a particular Bragg reflection, geometry of the experiment and the ratio of the source-specimen distance to the specimen-detector distance. The diffracted intensity can lie somewhere between the two extremes of an "ideally perfect crystal" and that of an "ideally imperfect crystal". The latter term is somewhat harder in practice to realize. The diffracting power of imperfect crystals is usually much higher than that from perfect crystals [6].

XRT provides a two-dimensional map of the defect content in a single crystal. It is mainly used for the study of dislocations, planar defects, stacking faults, domain
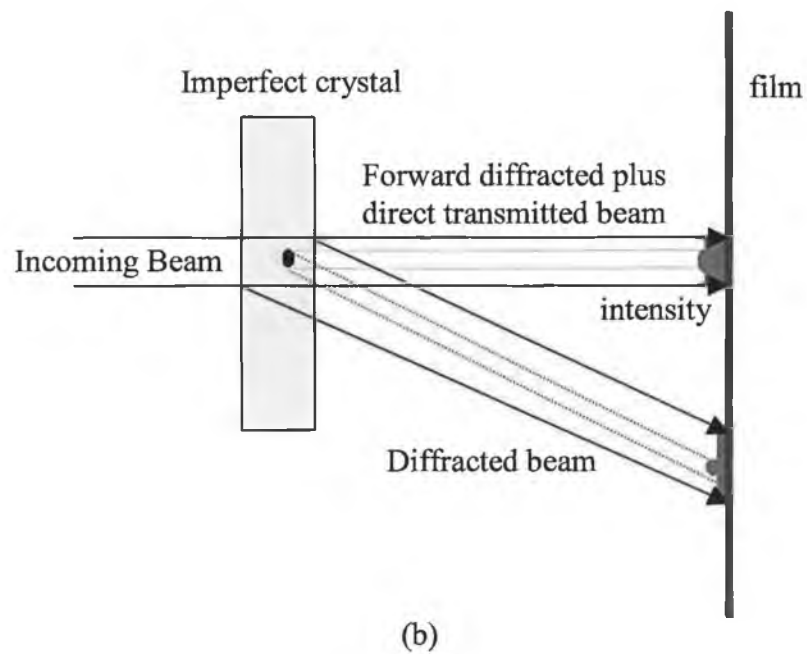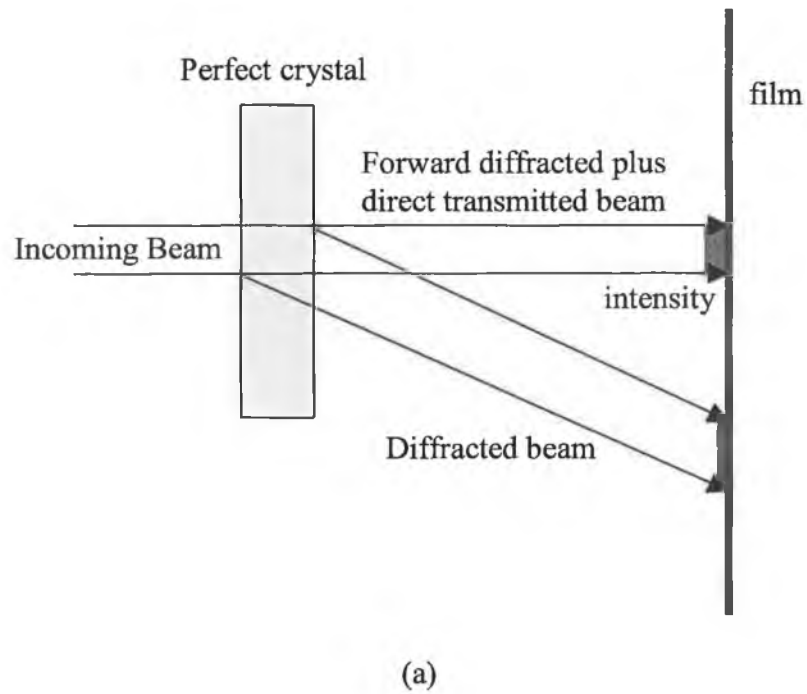
Figure 1.1: Basic principle of X-ray diffraction topography for an extended (homogeneous) beam. Situation for: a) perfect and b) imperfect crystals. Due to the high intensity of the direct transmitted beam, the defect image is usually immersed in the strong black background, and the defect contrast is very low and can hardly be discerned. Thus other reflections are always used for the interpretation of defects in the studied sample.
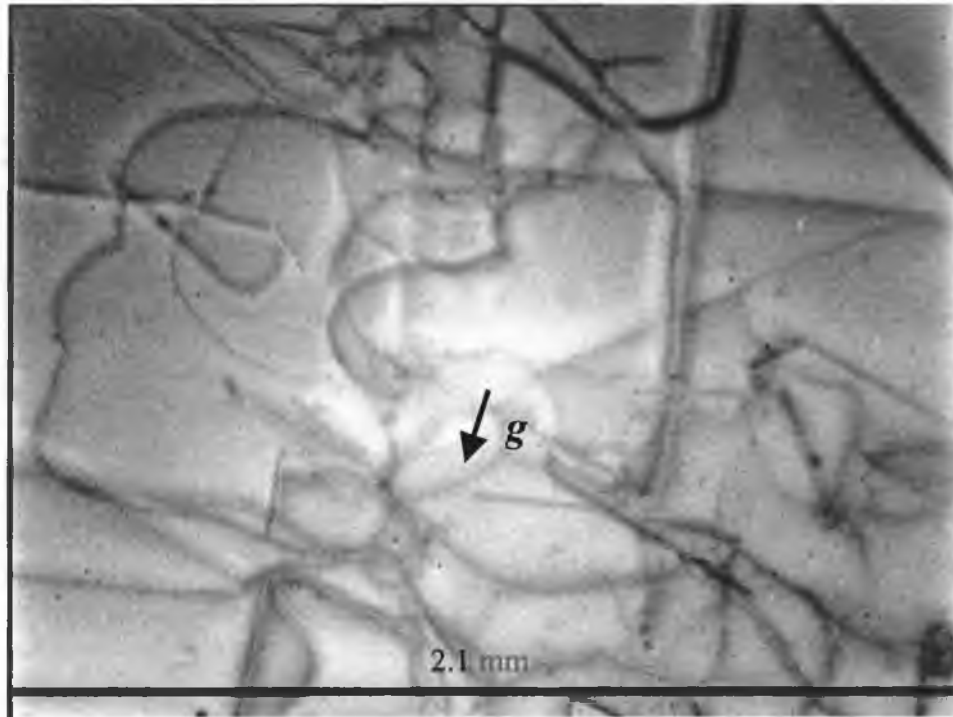
(a)
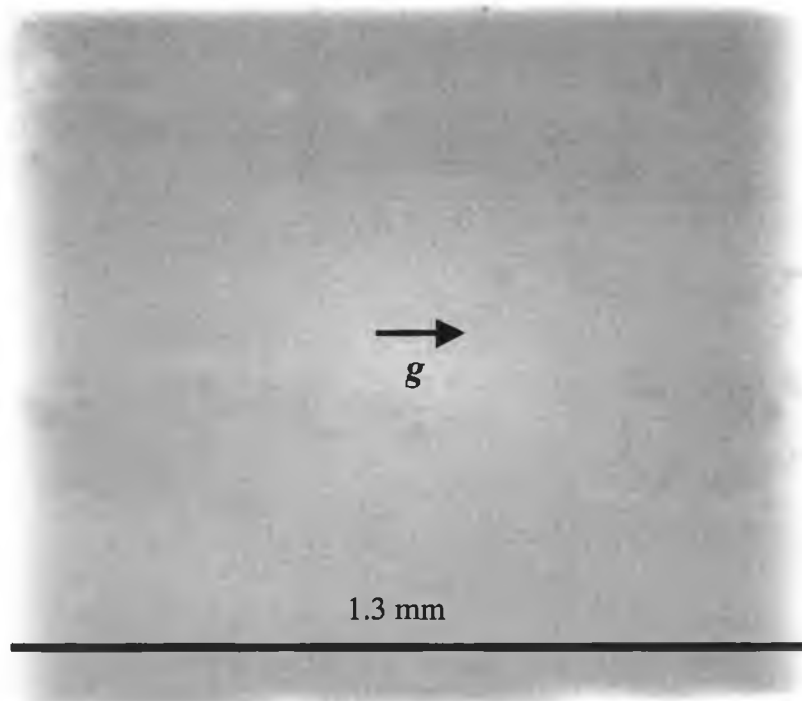
(b)

Figure 1.2: Synchrotron white beam back reflection X-ray topographs for (a) a HEM sapphire wafer containing dislocations, $01\bar{1}8$ reflection; (b) a perfect HEM sapphire wafer, $1\bar{1}08$ reflection. The diffraction vector $\bar{g}$ is defined as the vector that is perpendicular to its corresponding Bragg planes with a length equal to the reciprocal of the interplanar spacing.
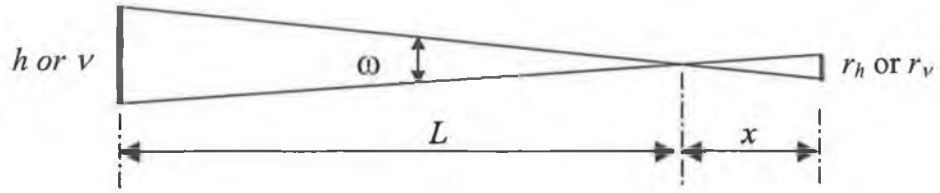
Figure 1.3: Schematics for geometrical resolution in X-ray topograph.

walls in ferroelectric and magnetic materials, growth defects, large precipitates, etc [7]. As dislocations have important effects on the semiconductor materials and devices, they are carefully studied in a selection of crystal materials in this study. The basic theory of dislocations, their effects on semiconductor devices and related information will be introduced briefly in chapter 2.

The spatial resolution of X-ray topography depends on many factors, for example, distance from the X-ray source to the sample, distance from the sample to the detector (usually high resolution or standard X-ray film), divergence of the X-ray source, X-ray beam size and the detector resolution. The horizontal (r_h) and vertical (r_v) resolutions can be expressed as [2]:

$$r_h = x\frac{h}{L} \tag{1.1}$$

$$r_v = x\frac{v}{L} \tag{1.2}$$

where x is the distance from sample to detector; L is the distance from X-ray source to sample; h and v are the horizontal and vertical dimensions of the source. The schematics for geometrical resolution are shown in Fig. 1.3. However if the natural divergence of the synchrotron X-ray beam, Ω, is smaller than $\frac{h}{L}$ or $\frac{v}{L}$, then the resolution is equal to $\Omega \cdot x$ [14].

For topography experiments in beamline F1, HASYLAB, in this study, L is about 33 metres, x is about 50 to 90 millmetres [3-5, 8]. The full width at half maximum horizontal and vertical dimensions of the source are 1.224 mm and 0.510 mm, respectively [9]. Thus the theoretical horizontal and vertical resolution for topographs obtained at Beamline F1 are estimated to be: 2 to 3 microns along the horizontal direction and 0.8 to 1.4 microns along the vertical direction. Because of its resolution limitation, X-ray topography is suitable for studying single crystals with a

low density of imperfections. Typically the maximum defect density that can be studied is $\sim 10^4 \text{cm}^{-2}$. For example, it is not easy to discern each dislocation line in a modified Czochralski method produced sapphire wafer, which has a dislocation density of 9 x 10^4cm^{-2}[4]. If the dislocation density increases further, only black and featureless topograph will be obtained [5, 8], and the individual dislocation contrast disappears from the corresponding topograph because the resolution of the topograph is not high enough. One such topograph is shown in Fig. 1.4, which is taken from an ELO GaN epilayer, wherein the dislocation density in the ELO GaN epilayer is believed to be around 10^7cm^{-2}[8, 10-12].

However this resolution can be much improved by extending the distance from source to sample. For example, in Spring8, this distance is 1 km for the topography beamline [13].

In the x-ray topography technique , the defect is only active through the strain introduced in the host lattice, and the additional variation of departure $\delta(\Delta\theta)$ from the Bragg incidence in the defected region is [1]:

$$\delta(\Delta\theta) = \frac{\lambda}{\sin 2\theta} \frac{\partial}{\partial S_h} (\vec{g} \bullet \vec{b}) \qquad (1.3)$$
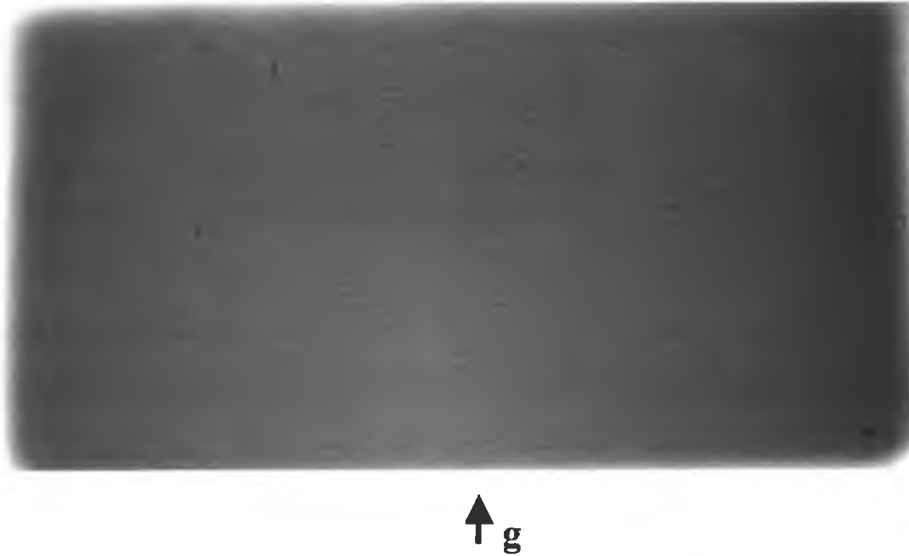
Figure 1.4: Synchrotron white beam large area transmission $1\bar{2}1\bar{2}$ topograph of epitaxial lateral overgrown GaN epilayer (the dimension for this topograph is 3.5 mm x 2 mm).

where θ is the Bragg angle for the corresponding reflection; S_h is the coordinate along the reflected direction; $\bar{g}$ is the diffraction vector; and $\bar{b}$ is the displacement field of the defect. It can be seen from equation (1.3) that if the defect displacement field is normal to the diffraction vector $\bar{g}$, the defects will not be detected in the corresponding reflection. Thus by checking the extinction of defect images from several reflections, it is possible to determine the Burgers vectors or fault vectors for dislocations or stacking faults [3].

Table 1.1[6] A chronological summary of the topographic techniques employed by various workers with laboratory equipment. The table shows whether a white radiation beam or single wavelength x-rays were used in the investigation and the type of experimental arrangement used to obtain the topographs.

Year	Author	Continuous Radiation	Characteristic Wavelength	Transmission	Reflection
1931	Berg		√	×	√
1944	Ramachandran	√		√	
1945	Barrett		√ Co	×	√ (SC)
1945	Wooster & Wooster		√ Cu		√ (DS)
1949	Guinier & Tennevin	√		√	
1952	Bond & Andrus		√ Cu K_α		√ (DC)
1954	Schulz	√			√
1957	Lang		√ Ag K_α		(SC)
1958	Newkirk		√ Cr K_α		√ (SC)
1958	Lang				
1958	Bonse & Klapper		√		(DC)
1959	Newkirk, Lang				

Abbreviations in parenthesis: SC – slit collimated, DS – diverging source, DC-double crystal technique

1.3 Description of synchrotron X-ray production

Synchrotron radiation is produced when energetic charged particles (electrons or positrons) are accelerated to near the velocity of light in a curved path. The charged particles are kept in the orbit by the magnetic field, B, perpendicular to the plane of the orbit, i.e. the Lorentz force applied to the charges must be equal to the centripetal force. The applied magnetic field B can be expressed as [14]:

$$B = \frac{m\gamma c}{Re} \qquad (1.4)$$

where $\gamma = \frac{E}{mc^2}$, E is the energy of the particles, e is their charge and m is the rest mass of the charged particle, R is the radius of the orbit and c is the velocity of light. The storage ring is composed of an alternation of bending magnets and insertion devices which are inserted in the straight sections of the storage ring.

Synchrotron radiation was first observed by scientists in the General Electric laboratory around 1947 [14]. As this kind of radiation was first observed in a synchrotron, it was named "synchrotron radiation". The theory for the electromagnetic radiation emission by a charged particle moving along a circular orbit at speeds close to light was developed by Schwinger [14-15] a little later. The power radiated by a charged particle at speed of v in a solid angle 4π can be expressed:

$$P = \frac{2}{3} \frac{e^2 c}{R^2} \left(\frac{v}{c}\right)^4 \gamma^4 \qquad (1.5)$$

P decreases very rapidly with the mass of the particle, so only electrons or positrons are used as the charged particles for synchrotron radiation. The synchrotron source used in this study uses radiation emitted by positrons in the DORIS III storage ring in HASYLAB.

Energy lost by the electric charges is supplied once or more per revolution by an oscillating radio frequency electric field along the orbit [14]. The beam current decays exponentially by collisions with residual gas molecules in the ultra-high vacuum system, thus regular new charge injection is necessary in order to maintain high X-ray intensity. A schematic for the generation of synchrotron radiation is shown in Fig. 1.5, but actually the orbit of storage ring is not circular. It consists of dipole bending magnets separated by straight sections with insertion devices. Beamlines are constructed to extract the beams from the tangent points of
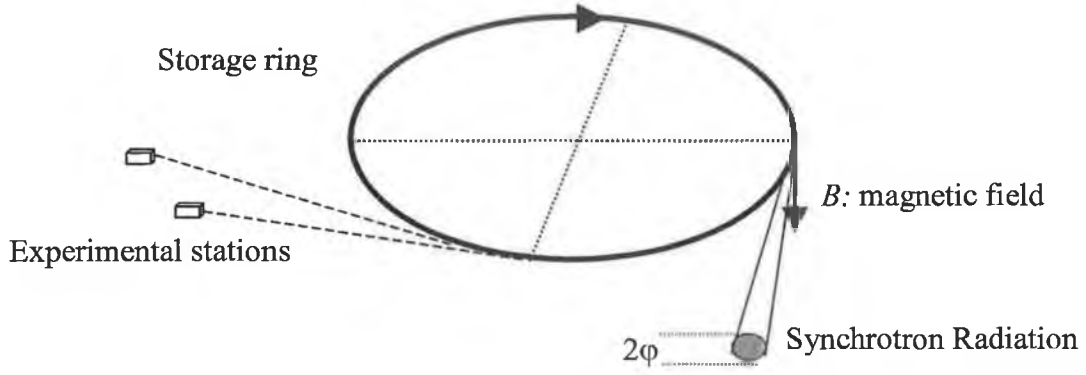
Figure 1.5: Schematics for Synchrotron radiation.

the bending magnets or from insertion devices within the straight sections [16].

A typical insertion device is comprised of rows of magnets with alternating polarity and is installed in a straight section of the electron orbit. The orientation of the magnetic fields is perpendicular to the trajectory of the particles, therefore the relativistic charged particles wiggle around their mean path. Corresponding to weak and strong magnetic fields, there are two types of insertion devices : the undulator or the wiggler. The schematics for synchrotron radiation produced in the bending magnetic and undulator configurations are shown in Fig. 1.6.

For the bending magnet, the stored charges run in a circular orbit and emit synchrotron radiation with a continuous spectrum when they encounter the bending magnet. In the case of insertion devices, the charges are deflected with a small radius of curvature by a succession of dipole magnets of alternating sense. The particle beam wiggles with a large deviation angle in a wiggler because of the strong magnetic fields, and as a result, bright and spectrally continuous light with short wavelengths is obtained. In the undulator, the electron beam wiggles with a small deviation angle, and as a result, ultra-bright and quasi-monochromatic light is obtained via an interference effect [14, 16].

The natural vertical divergence of the radiation (see Fig. 1.5) from the synchrotron is about:

$$2\varphi \approx 2\gamma^{-1}. \tag{1.6}$$

Since the energy of the positrons in DORIS III is about 4.45 GeV [9], the vertical divergence for the synchrotron radiation is estimated to be about 110μrad.

(a)

(b)
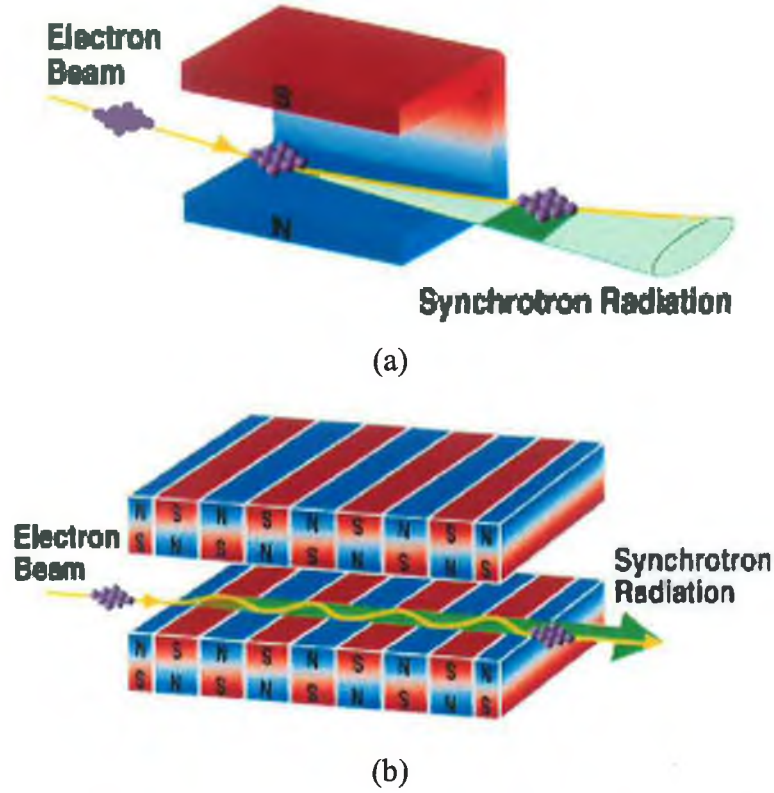
Figure 1.6: Schematics for synchrotron radiation produced by a: a) bending magnet, b) undulator [13].

The horizontal divergence of the synchrotron radiation is usually determined by the slit before the beam arriving at the sample [14, 16].

The synchrotron radiation possesses many properties which simply cannot be achieved using conventional radiation sources such as X-ray tubes.

The radiation from the synchrotron source is continuous in wavelength, usually extending from the infrared to the hard X-rays with a broad maximum in the number of emitted photons close to the critical wavelength λ_c (Å) given by [14]:

$$\lambda_c = \tfrac{4}{3} \pi R \gamma^{-3} \qquad (1.7)$$

After replacing the constants by their numerical values, the critical wavelength can be written as:

$$\lambda_c = \frac{18.64}{BE^2} \qquad (1.8)$$

and its corresponding critical energy E_c can be expressed as:

$$E_c = 0.665 BE^2 \qquad (1.9)$$

In (1.8) and (1.9) λ_c is in Å, E_c is in KeV. $B = \frac{3.34E}{R}$ in Tesla (T), E is the kinetic energy of the accelerated particles expressed in GeV and R the bending radius in the magnet expressed in metres. The critical wavelength λ_c is defined as that wavelength such that half of the total power emitted by the synchrotron is at wavelengths $\lambda \angle \lambda_c$.

For the DORIS III bending magnetic storage ring, the usual energy E for positrons is 4.45 GeV, R=12.1849 m, and B=1.2182 T, thus yielding a normal critical wavelength λ_c=0.7717 Å and a critical energy E_c=16.04 KeV. At higher energies with wavelengths shorter than λ_c, the radiation intensity falls fast, but at lower energies, the radiation intensity changes more slowly. In fact it decreases only by a factor of 10 over a wavelength range up to $1000\lambda_c$ [14].

The spectrum produced by a wiggler is similar to that from a bending magnet except that the wavelength is shifted to a shorter value because of the higher magnetic fields in the wiggler.

The spectrum from the undulator is much different. Radiation from it has a smaller divergence than that from the wiggler. Beams are emitted by the individual pole interface of the undulator, and the radiation is emitted along the undulator axis and is quasi-monochromatic. The spectrum consists of the sum of a fundamental line and its harmonics. The beam frequency from the undulator is tuneable; it can range from very narrow band, even monochromatic radiation, to a continuous spectrum similar to those from bending magnets and wigglers. As the spectrum from an undulator varies rather fast as a function of angle, this means that the beam arriving at the sample has a different spectral characteristic at every point. The synchrotron X-ray source from the undulator is not suitable for X-ray topography unless a long beamline is used [16].

Compared to the traditional laboratory X-ray source, the brightness of the synchrotron radiation source could be 10^3 to 10^8 times higher or even more, where the brightness is defined as the flux of photons emitted by the source per solid angle and per bandwidth. It is expressed in units of photons $s^{-1}mrad^{-2}(0.1\%\delta\lambda/\lambda)^{-1}$[14]. In some cases, another parameter, brilliance, is used to indicate the synchrotron radiation intensity. This is defined as brightness per unit transverse area of the source, which is expressed as photons $s^{-1}mrad^{-2}mm^{-2}(0.1\%\delta\lambda/\lambda)^{-1}$.

The typical synchrotron spectra for HASYLAB-DESY are shown in Fig. 1.7. The low wavelength fall-off is determined by the energy of the electron or positron beam and the radius of curvature at the point of emission.

Modern synchrotron radiation facilities, such as HASYLAB, are composed of a large range of advanced equipment which occupies a large area. Large funding for maintenance and operation is needed, and certainly a lot of interesting and useful scientific results can be obtained from these facilities by researchers from all over the world.
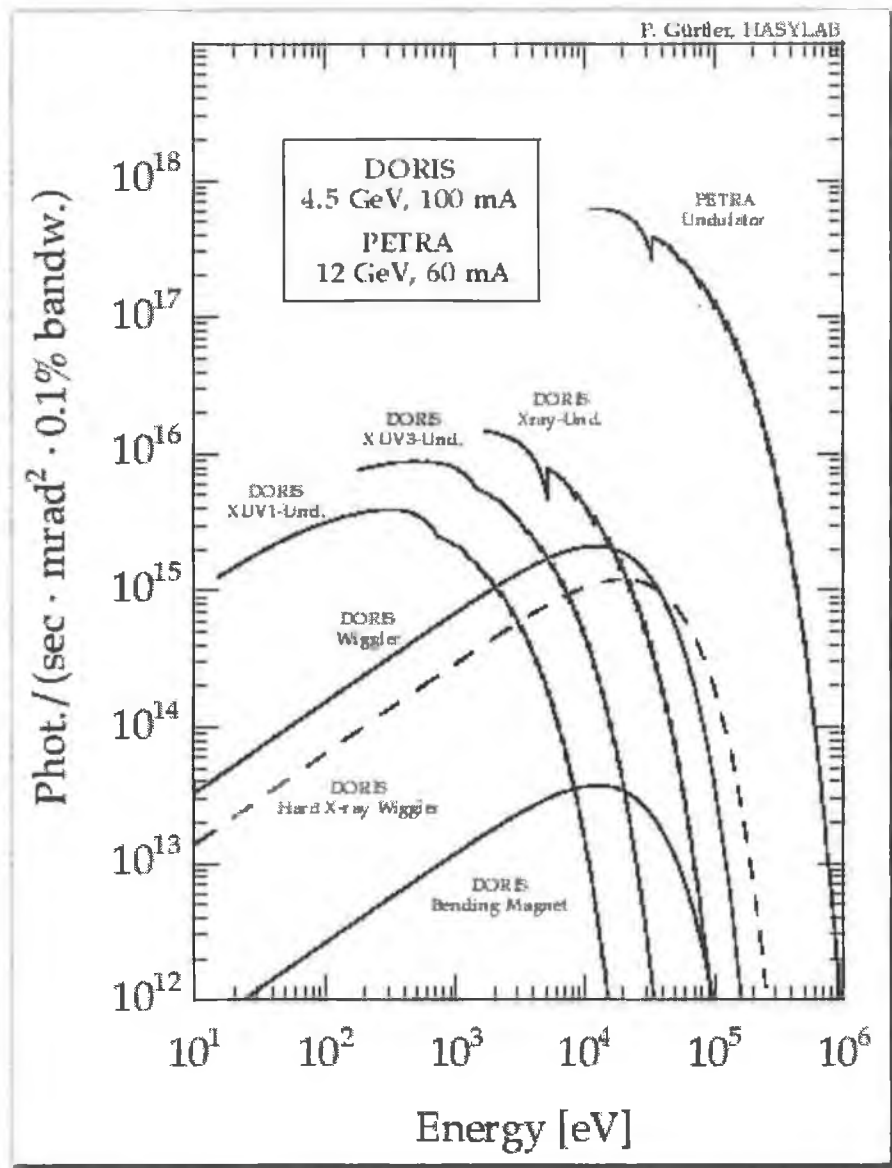
Figure 1.7: Spectral angular flux of insertion devices at DESY [9].

1.4 Features of Synchrotron X-ray topography

1.4.1 Conventional laboratory X-ray sources

The most common X-ray source in the laboratory is the high vacuum tube with an anode and cathode under high voltage, usually around 20-50 kV. Electrons are emitted from the cathode and moved to the anode with high energy, $E \approx e.V$, where e is the charge of electron and V is the applied voltage. The anode is usually referred as the target. The emitted spectrum is the superposition of a continuous white spectrum and a few characteristic lines. The characteristic lines are specific for each anode metal [14]. The usual anode metals are Cu, W, Fe or Mo, etc. The continuous spectrum emitted by the anode is due to the slowing down of electrons in the anode from the cathode, which is normally referred to as bremsstrahlung, this German term "bremsstrahlung" meaning "braking radiation". The highest frequency for bremsstrahlung is:

$$\nu_{max} = \frac{e.V}{h} \qquad (1.10)$$

where h=6.625 x 10^{-34}J.s is the Planck constant. If greater X-ray intensity is required, then higher voltage is necessary. However when electrons hit the target, most of the energy from the electrons is transferred into heat. In order to keep the equipment working properly, the target needs to be cooled effectively; usually it is cooled with water. For even higher power X-ray generators, the anode target is rotated for more effective cooling.

The characteristic lines result from the decay of excited states of the element constituting the metal anode of the tube. As the elements can exist in different states (such as the ground state, lower excited state, etc.), after decay, photons of different energies are consequently emitted, and as a result X-rays with different wavelengths are generated. The energy gaps between different electron states are specific for each element, thus characteristic lines are produced. The laboratory X-ray source is unpolarized and can be considered as a sum of incoherent spherical waves emitted by the different points of the anode. The smallest dimension of the focus from a laboratory X-ray generator for high resolution topography is of the order of 10-100 μm [14].

1.4.2 Advantages of white beam synchrotron X-ray topography

The advantages of white beam synchrotron x-ray sources over the traditional laboratory x-ray source are [1, 7, 14, 16]:

1) High brilliance, ranging from 10^{14} photons $s^{-1}mrad^{-2}mm^{-2}(0.1\%\delta\lambda/\lambda)^{-1}$ for a bending magnet to 10^{19} to 10^{21} photons $s^{-1}mrad^{-2}mm^{-2}(0.1\%\delta\lambda/\lambda)^{-1}$ for undulators. This implies much shorter exposure time, usually in the range of a few seconds for standard X-ray recording films and a few minutes for high resolution films.

2) White spectrum available for bending magnets and wigglers, and possibly monochromatic use with undulators.

3) Narrow divergence (in the 10^{-4} rad. range).

4) Small beam size possible, which can be a few tens of microns vertically and one or two hundred microns horizontally.

5) Very low emittance, as a consequence of the small source size and the small beam divergence.

6) Long source to sample distances possible. For example, it is up to 1000 metres for some beamlines at Spring-8, thus enabling more complicated equipment to be placed between the sample and source, e.g. for *in situ* measurements.

7) Nearly pure linear polarization.

8) Less stringent requirement for sample positioning (a fraction of a degree, while it is a few seconds of arc in laboratory set-ups working with characteristic lines).

9) Compared to Lang topography, no need for scanning since the instantaneous image is two dimensional.

10) Simultaneous recording of many reflections with different diffraction vectors for white beams.

11) Ability to obtain homogeneous images for warped samples or crystals presenting a subgrain structure because of the simultaneous satisfaction of Bragg's law for different regions.

Due to the increasing availability of synchrotron X-ray sources, the applications of topographic techniques have grown considerably. These can now be applied to study, under reasonable conditions, very weak reflections, weak distortions, *in-situ* crystal growth, defect nucleation and movement in crystals and thin films, dynamics of domains, phase transitions, etc. [1, 33]. The new features of

third generation synchrotrons provide even more possibilities for the application of these techniques. Some of these features (high intensity, high energy photons in the beam) extended substantially the previous possibilities (investigation of heavier or thicker crystals, study of dynamical phenomena with smaller typical times) and have also enhanced the spatial resolution (weak beam technique, systematic use of section topographs) [33]. The small angular size of the source δ leads to a very high geometrical resolutions.

1.4.3 Disadvantages of white beam synchrotron X-ray topography

Despite the many advantages of this technique, like every other technique, white beam synchrotron x-ray topography has its disadvantages. These are listed as follows [1]:

1) radiation damage;

2) heat damage;

3) high fluorescence background from the sample or its immediate surroundings;

4) problems with the superposition of several harmonics in each diffracted spot, λ, $\lambda/2$, $\lambda/3$... (see Section 1.6)

1.5 Typical experimental set-ups and procedures for white beam synchrotron X-ray topography

Two main experimental arrangements are employed in this study, i.e. set-ups for back reflection and transmission topography. In each set-up, there are two experimental methods, i.e. large area and section topography methods.

1.5.1 White beam Transmission topography

1.5.1.1 White beam large area transmission topography

Large area transmission (LAT) topography is one of the most commonly used techniques. In this technique, the recording film is put behind the studied sample in the transmission method.

When a single crystal is immersed in a white X-ray beam a number of lattice planes (hkl) select out of the continuous spectrum the proper wavelengths to be reflected according to Bragg's Law. A beam diffracted in a certain direction 2θ with respect to the incident beam has a spectrum of wavelengths λ, $\lambda/2$, $\lambda/3$, etc. corresponding to diffraction lattice planes (hkl), (2h 2k 2l), (3h 3k 3l) etc. The fundamental reflection hkl or its harmonics may, however, be structure factor forbidden (see later). This is the well-known Laue method.

Fig. 1.8 shows the typical experimental set-up for large area transmission topography. Due to the low divergence of the synchrotron radiation beam, each spot of this particular Laue pattern is itself a high-resolution topograph.
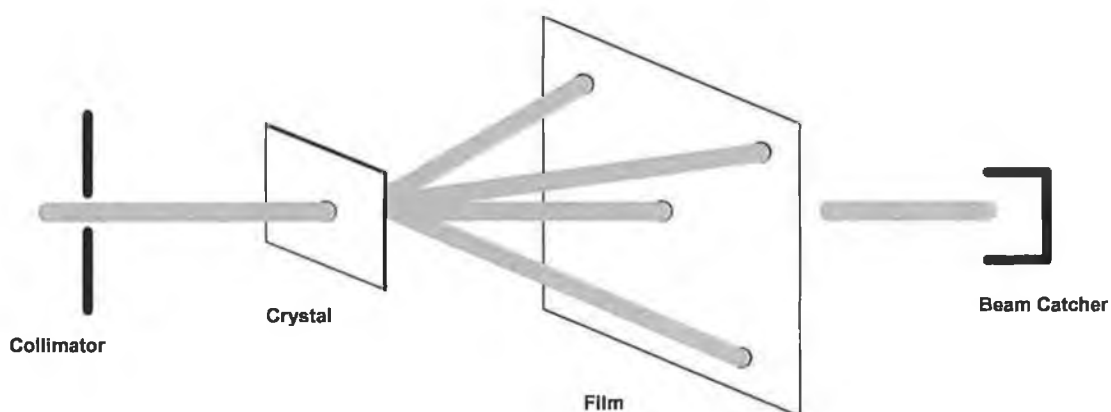
Figure 1.8: Schematic set-up for large area transmission topography.

1.5.1.2 White beam transmission topography in section topography (ST) mode

An arrangement similar to that for Large Area Topography is used, only in this case the incoming beam is collimated into a narrow ribbon by a slit typically 10-15 μm in width. Provided that the Bragg angle is not too small, the image gives detailed information about the energy flow within the crystal and direct depth information on the defects present in a particular crystal slice. The imaging mechanism for just two reflections is shown in Fig. 1.9.
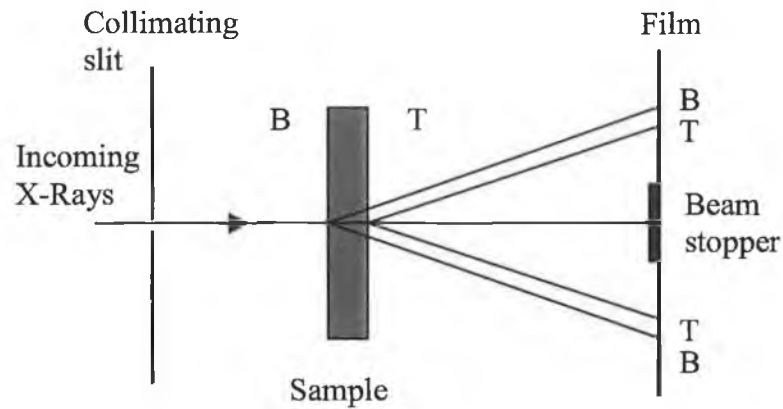
Figure 1.9: Schematic set-up for transmission section topography.

1.5.2 White beam back reflection topography

1.5.2.1 Large area white beam back reflection topography

In the large area back reflection topography (BRT) set-up, the incoming x-rays are perpendicular to the upper surface of the sample. This Bragg geometry is used to access information about the upper regions of the sample as illustrated in Fig. 1.10. Depending on the wavelength of the diffracted beam typical penetration depths, t_p, which will be introduced later in Section 1.6, can vary from <1 μm to >1000 μm in the studied sample. Penetration depths tend to be much smaller in unstrained perfect crystals, where the dynamical theory of diffraction applies. However, for imperfect or strained materials, e.g. GaN, GaAs, SiC, InP or silicon with circuit topography or strained epitaxial layers, conventional kinematical theory applies.
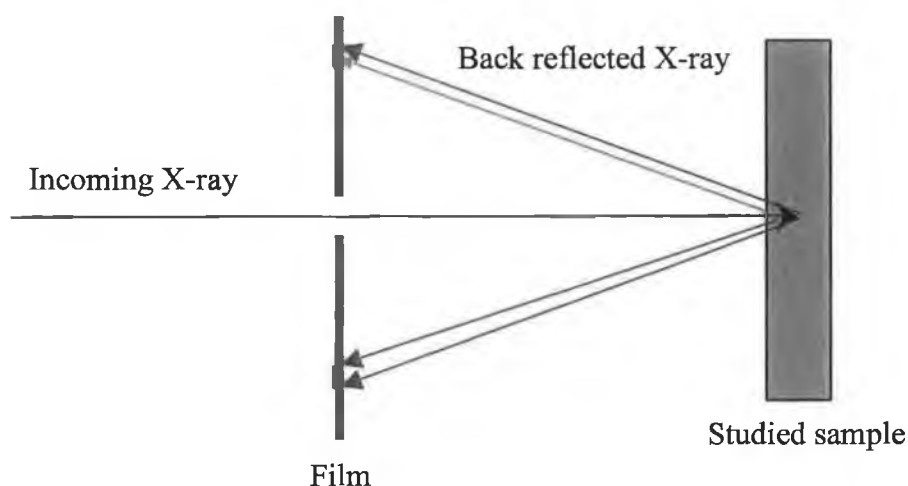
Figure 1.10: Schematic set-up for large area back reflection topography.

1.5.2.2 White beam back reflection section topography

The white beam back reflection section topography (BRST) technique is essentially similar to BRT, only in this case the incoming beam is again collimated into a narrow ribbon by the slit. A set of Bragg case section topograph images of sample cross-sections is produced. The schematic set-up is shown in Fig. 1.11.

In this study, the topographs were recorded on both standard Kodak Industrex SR film or high resolution Slavich VRP-M holographic film having an emulsion grain size of about 0.04 μm. The storage ring operated at a typical currents of 80-150 mA. The exposure time depends on the ring current and the film type. It is common practice to use the total integrated exposure as a benchmark and this is expressed as mA.min or mA.s. Thus if we have a beam current of 100 mA and expose the X-ray film for 60 s then the total integrated exposure is 6000 mA.s. Usually, the high resolution films need to be exposed for 60 times longer, i.e. if 10 mA.min is necessary for the high resolution film, then 10mA.s is enough for the standard film. The appropriate exposure time needs to be tested before the final topograph can be taken in order to optimize the topograph contrast. For section topography, exposures usually take about 10 times longer than large area topography.

The exposed films are developed and fixed in the dark room with standard procedures. In this process, the films are first soaked in the developer solution for about 5 minutes, then moved to the fixer solution for another 10 minutes; before moving to the fixer solution, they are soaked in the stop bath for a few seconds.
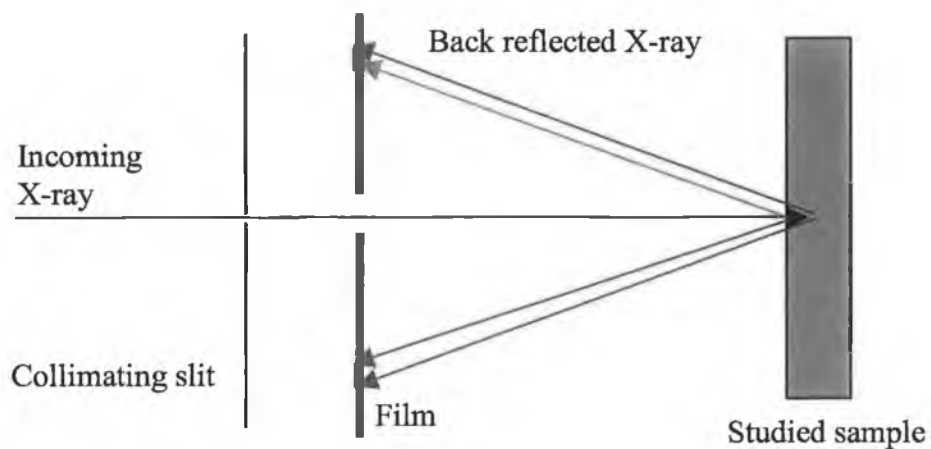
Figure 1.11: Schematic set-up for back reflection section topography.

Finally the films are washed in cold, running, filtered water for a few hours and dried in a dying cabinet.

The pictures, which appear in this study, have been generated on a system comprising of a CCD camera, frame-grabber and appropriate software.

1.6 Indexing the recorded diffraction pattern

One important step in the interpretation of X-ray topographs is the indexing of the diffraction pattern on the recorded film, through which the correct diffraction vectors g can be obtained. In many situations, for example in the determination of the Burgers vectors b of dislocations in this study or the assessment of stress [17-18], etc., a knowledge of the diffraction vector g is essential. In this study, a software package named OrientExpress [19] is used to obtain the correct indices. OrientExpress makes it possible to orient a single crystal of known unit cell dimensions from a single Laue pattern. This pattern can be registered on the X-ray film, a two-dimensional sensitive detector or bitmap picture.

The program first computes and displays the corresponding simulated Laue pattern or set of patterns, and then the correct solution is unambiguously obtained through a visual comparison of the experimental pattern with the set of simulated ones. In order to do the simulation, some information related to the crystal sample and experimental set-up must be input on the screen panel of the software, which includes:

1) The crystal system and space group.

2) The crystal unit parameters.

3) The sample to film distance and the angle between the film normal and the incoming X-ray direction; in this study, this angle is 0° for the transmission topography and 180° for the back reflection topography.

4) The wavelength range.

5) The dimension of the film.

6) The coordinates of a few strong reflection spots (i.e. darker spots on the film). Usually choosing 4 or 5 spots is better, if more spot coordinates are input, sometimes it is not easy to get the solution.

During simulation the distance between the film to sample should be adjusted slowly to arrive at a simulated pattern close to the experimental pattern, as the measurement for this distance may be slightly erroneous. Sometimes the step size for this distance adjustment can be around 0.05 mm or even smaller. After a similar simulation pattern is obtained, a rotation of this pattern along the X, Y and Z axis or
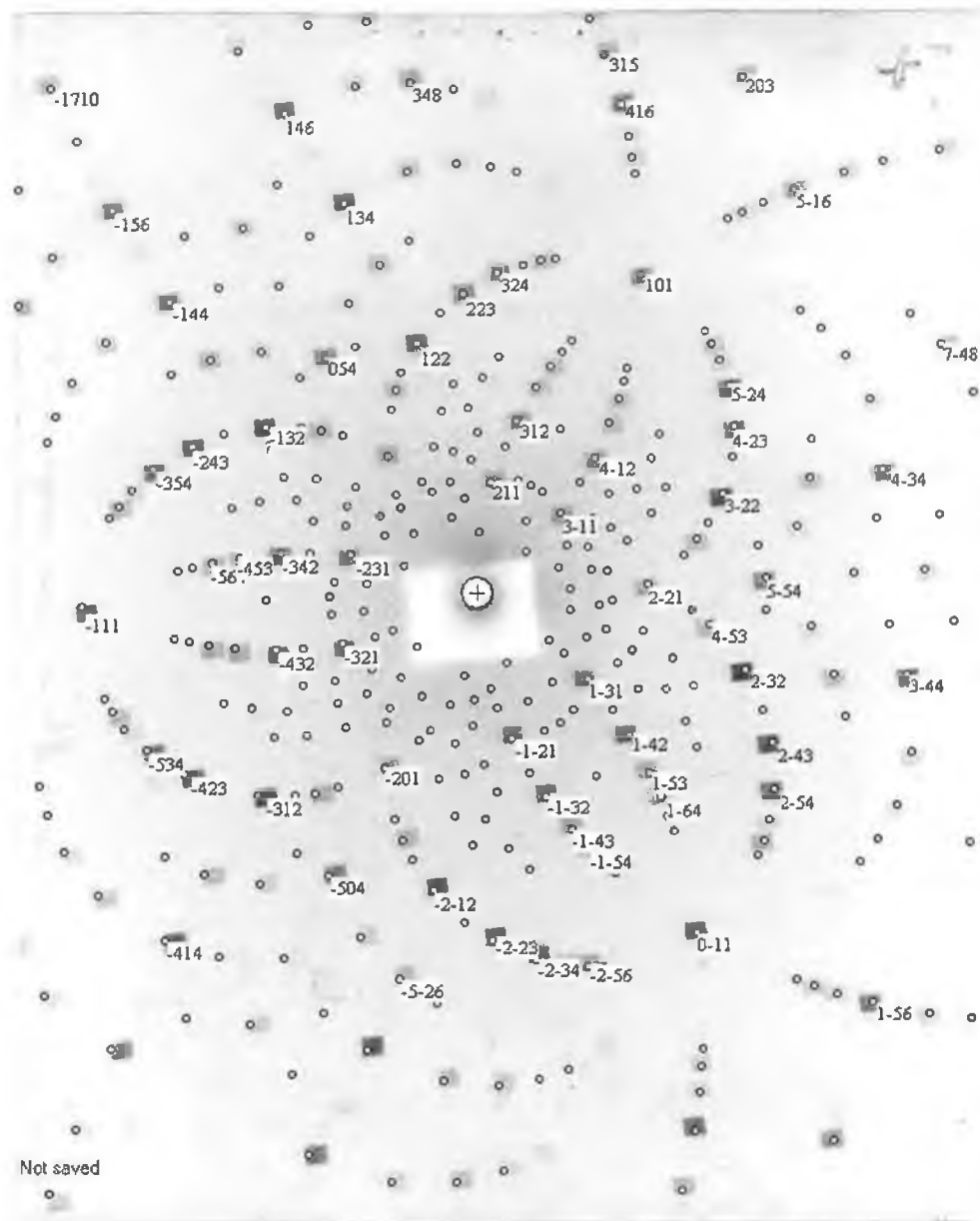
Figure 1.12: Example of experimental and simulated Laue pattern for sapphire single crystal. The black squares are experimental Laue spots, and the bright circles are simulated Laue spots. Note: only the fundamental harmonic index for the reflection spot appears on the simulated pattern.

their combination is also very effective.

Occasionally adjustment of the wavelength range may help the simulation. If some information about the crystal orientation is available, it may be easy to start from the known sample orientation or from the estimated orientation for the unknown orientation sample, then one can rotate the simulated pattern continuously until exact matches between the experiment and simulation are reached.

One such example is shown in Fig. 1.12, which shows that the simulated Laue pattern fits quite well with the experimental result. The indices for some reflection spots are also indicated in Fig. 1.12.

1.7 Penetration depth for X-rays

In the crystal samples, defects are usually distributed along different depths from the sample surface. Defect images appearing in the X-ray topographs, for example, for a back reflection topograph, are actually overlapping images of defects within a certain thickness from the surface. If the crystal sample is thick enough, defects in the deeper part of the sample cannot be detected, as the X-ray intensity will decrease due to absorption. It is therefore important to learn what is the depth within which the defects appear in the topograph, and this depth is defined by the X-ray penetration depth, t_p.

1.7.1 Penetration depth for large angle incidence topography

When the incident and exit angles are bigger than the critical angle ϕ_c for total reflection (ϕ_c is usually around a few tenths of degree), the kinematical penetration depth t_p, which is measured perpendicular to the surface, at which the intensity of the outgoing reflected beam has dropped to $1/e$ times of that of the incident beam due to absorption, can be expressed as [20]:

$$t_p = [\mu(\tfrac{1}{\sin\phi_0} + \tfrac{1}{\sin\phi_n})]^{-1} \tag{1.11}$$

where μ is the wavelength-dependent linear absorption coefficient for the material, whose value can be obtained from the wavelength-dependent attenuation length D of the material, which can be obtained from the literature [21], ϕ_0 is the incident angle, and ϕ_n is the exit angle.

The relationship between the effective linear absorption coefficient μ and the attenuation length D is:

$$\mu = \tfrac{1}{D} \tag{1.12}$$

1.7.2 Penetration depth for grazing incidence topography

When ϕ_0, $\phi_n \angle \phi_c$, i.e. in the grazing incidence geometry, (1.11) will be invalid, and the X-ray penetration depth is expressed via the general equation [22]:

$$t_p = \frac{\lambda}{4\pi(l_i + l_f)}$$ (1.13)

where

$$l_{i,f} = \frac{1}{\sqrt{2}}\{(2\delta - \sin^2 \alpha_{i,f}) + [(\sin^2 \alpha_{i,f} - 2\delta)^2 + (2\beta)^2]^{1/2}\}^{1/2}$$ (1.14)

For (1.13), λ is the vacuum wavelength,

$$\beta = \lambda\mu/(4\pi)$$ (1.15)

$$\delta = \overline{\rho}_e e^2 \lambda^2 /[2m_e \varepsilon_0 (2\pi c)^2]$$ (1.16)

where $\overline{\rho}_e$ is the number of electrons per unit volume, m_e is the electron mass and e is the elementary charge, ε_0 is the vacuum permittivity and c is the velocity of light.

For grazing incidence topography, the X-ray penetrates only a few nanometres of the sample. However when the incident angle ϕ_0 approaches the critical angle ϕ_c, the penetration depth increases rapidly, while the penetration depth increases much more slowly with the incident angle when it is larger than the critical angle. Descriptions and graphs indicating the relationship between the penetration depth and the incident angles can be found in the literature [20, 23]. As a specific sample, the penetration depth usually changes more obviously for some reflections [20], thus by combining different experimental set-ups (grazing incident and large angle incident) and selections of reflections, it is possible to study the defect distribution for different depths of the measured sample.

1.7.3 Calculation of the penetration depth for some reflections in sapphire crystal

For white beam synchrotron X-ray topography, the topographs are the result of overlapping images formed by several harmonics. The detector, i.e. the film for this study, records the integrated intensity. After considering the effect of the synchrotron X-ray source spectrum, the absorption of X-rays in the air, beryllium windows, aluminium filters, film envelopes and film emulsions (AgBr), and the structure factor for each harmonic, the contribution of each harmonic to the integrated contrast can be estimated [2, 20, 24-25]. If the contribution of harmonics is less than 5%, then usually they can be neglected in the integrated topograph intensity [18].

The number of photons absorbed in the recording film exposed during an X-ray topography experiment is [20]:

$$N_{abs}(\lambda) = f_1(\lambda)f_2(\lambda)f_3(\lambda)N_0(\lambda) \tag{1.17}$$

where $N_0(\lambda)$ is the spectral photon brightness of the synchrotron X-ray source at the orbit plane, which can be expressed as [20, 26]:

$$N_0(\lambda) = C(\tfrac{\lambda_c}{\lambda})^3 K^2{}_{2/3}(\tfrac{\lambda_c}{2\lambda}) \tag{1.18}$$

where C is a constant, $\gamma = \frac{E}{mc^2}$, $K_{2/3}$ is a modified Bessel function and λ_c has already been defined in equation (1.8).

The factor $f_1(\lambda)$ is calculated according to the following equation:

$$f_1(\lambda) = \prod_i e^{-\mu_i x_i} \tag{1.19}$$

where μ_i and x_i are the effective linear absorption coefficient and the effective thickness of the i-th absorption layer, respectively. $f_1(\lambda)$ is used to estimate contribution of the absorption effects of different materials, between the beryllium window and the envelope containing the film, to the topograph intensity. In this study, the absorption effects of air between the beryllium window and the film, the beryllium window itself, an aluminium foil in front of the film envelope and the envelope (paper) were considered. The effective thickness for each absorption layer in this study is given in Table 1.2.

$f_2(\lambda)$ is calculated according to the following equation [24]:

$$f_2(\lambda) = \kappa F_{hkl}\lambda^3 \tag{1.20}$$

where κ is a constant and F_{hkl} is the structure factor for each reflection and their harmonics, whose value can be calculated with a software package XRDIFF [27].

Table 1.2 Effective thickness for each absorption layer

Absorption Material	Beryllium window	Air	Aluminium	Envelope (Carbon)
Effective thickness	0.25 mm	25 or 30 cm	40 μm	200 μm

$f_3(\lambda)$ is used to calculate the absorption effect caused by the film emulsion (AgBr), i.e. taking into account the number of photons absorbed in the film. It is expressed as:

$$f_3(\lambda) = 1 - e^{-\mu_f \chi_f} \tag{1.21}$$

where μ_f and χ_f are the emulsion effective linear absorption coefficient and the effective thickness, respectively. In this study, the thickness of AgBr emulsion is estimated to be about 5 microns for the films.

In practice, for the calculation of the contribution of each harmonics, only the relative values of $f_1(\lambda)$, $f_2(\lambda)$, $f_3(\lambda)$ and $N_0(\lambda)$ are needed, so knowledge of the constants C and κ are unnecessary.

Figs. 1.12 –1.15 show graphs of the relationship between the attenuation length D and the X-ray energy for air, aluminium, carbon and beryllium as a function of X-ray photon energy [21].

The relationship between the X-ray energy E and its wavelength λ is expressed as:

$$E = \frac{1.24}{\lambda} \tag{1.22}$$

where E is in units of eV, and λ is in units of microns.

As shown in (1.17), in order to calculate the number of photons absorbed in the recording film in exposed during an X-ray topography experiment, the individual components of (1.17) need to be calculated first. Table 1.3a and Table 1.3b list the values used for the calculation of $\sum_{i=1}^{4} \mu_i \chi_i$, which is used for the calculation of the absorption factor $f_1(\lambda)$ for some reflections and their harmonics for a sapphire crystal. The wavelengths for reflections and their harmonics are calculated with XRDIFF also. It can be noticed that in Table 3a and Table 3b, some reflections appear to be missing. For example, for the 3 0 $\bar{3}$ 18 series of reflections, 1 0 $\bar{1}$ 6 and 2 0 $\bar{2}$ 12, etc. are not listed. This is due to the fact that these reflections are structure factor forbidden as the result of structural extinction effect [28].

The space group of sapphire crystal [29-31] is $R\bar{3}c$, and its reflection conditions are expressed as [32]:

$$hkil : -h + k + l = 3n \tag{1.23}$$

N1.5620.42C.0003Ar.0094 Density=0.1251E−02, Angle=90.deg

Figure 1.12: Relationship between the attenuation length and X-ray energy for air.

Be Density=1.848, Angle=90.deg
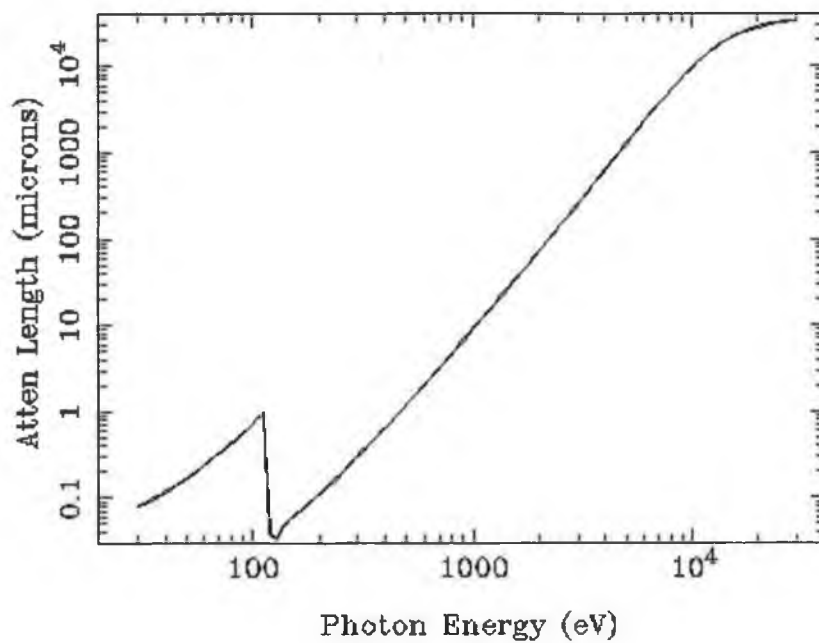
Figure 1.13: Relationship between the attenuation length and X-ray energy for beryllium.

Figure 1.14: Relationship between the attenuation length and X-ray energy for aluminum.

C Density=2.2, Angle=90.deg
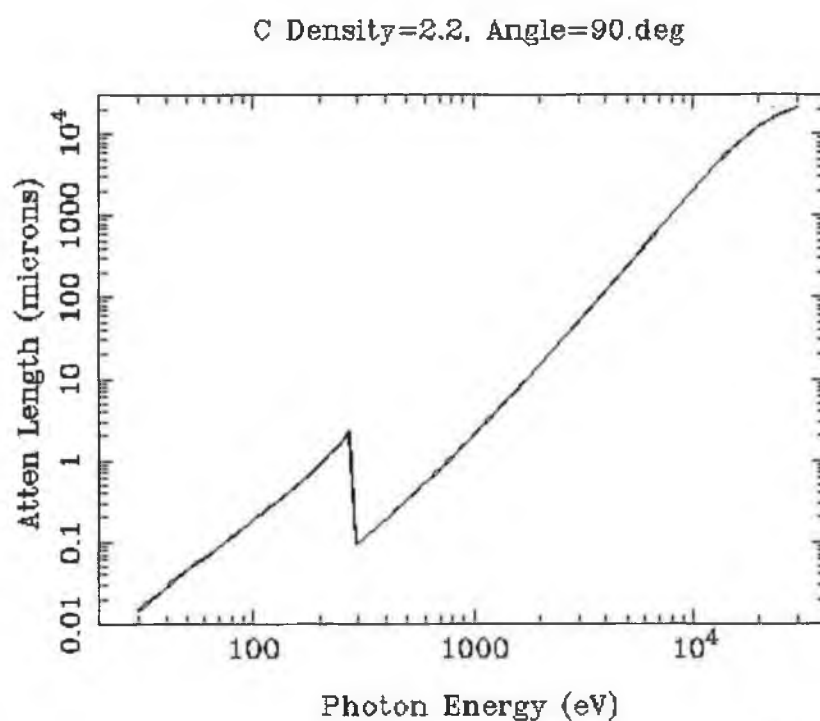
Figure 1.15: Relationship between the attenuation length and X-ray energy for carbon (paper).

Table 1.3a Calculation of the absorption effect caused by air, beryllium window, aluminum foil and envelope during white beam synchrotron X-ray back reflection topography exposure.

Index of reflection	X-Ray wavelength (Å)	$\mu_1\chi_1$ for air	$\mu_2\chi_2$ for Be	$\mu_3\chi_3$ for Al	$\mu_4\chi_4$ for C	$\sum\limits_{i=1}^{4}\mu_i\chi_i$
1 1 $\overline{2}$ 12	1.832	0.5837	0.0710	0.8273	0.3154	1.7974
2 2 $\overline{4}$ 24	0.916	0.0679	0.0076	0.1081	0.0336	0.2172
3 3 $\overline{6}$ 36	0.611	0.0184	0.0019	0.0313	0.0086	0.0602
4 4 $\overline{8}$ 48	0.458	0.0073	0.0007	0.0127	0.0032	0.0239
1 $\overline{2}$ 1 12	1.829	0.5837	0.0710	0.8273	0.3154	1.7974
2 $\overline{4}$ 2 24	0.914	0.0679	0.0076	0.1081	0.0336	0.2172
3 $\overline{6}$ 3 36	0.609	0.0184	0.0019	0.0313	0.0086	0.0602
4 $\overline{8}$ 4 48	0.457	0.0073	0.0007	0.0127	0.0032	0.0239
$\overline{1}$ 0 1 11	2.151	0.9554	0.1190	1.3100	0.5219	2.9063
$\overline{2}$ 0 2 22	1.076	0.1141	0.0128	0.1756	0.0573	0.3599
$\overline{3}$ 0 3 33	0.719	0.0500	0.0034	0.0520	0.0149	0.1204
$\overline{4}$ 0 4 44	0.514	0.0122	0.0013	0.0209	0.0055	0.0399
$\overline{5}$ 0 5 55	0.430	0.0060	0.0006	0.0105	0.0026	0.0197
2 $\overline{2}$ 0 22	1.082	0.1141	0.0128	0.1756	0.0573	0.3599
4 $\overline{4}$ 0 44	0.541	0.0125	0.0013	0.0215	0.0057	0.0410

Table 1.3b Calculation of the absorption effect caused by air, beryllium window, aluminum foil and envelope during white beam synchrotron X-ray back reflection topography exposure.

Index of reflection	X-Ray wavelength (Å)	$\mu_1\chi_1$ for air	$\mu_2\chi_2$ for Be	$\mu_3\chi_3$ for Al	$\mu_4\chi_4$ for C	$\sum_{i=1}^{4}\mu_i\chi_i$
1 0 $\bar{1}$ 7	3.035	2.2727	0.3706	3.5714	1.5528	7.7675
2 0 $\bar{2}$ 14	1.517	0.2809	0.0447	0.4843	0.1807	0.9906
3 0 $\bar{3}$ 21	1.012	0.0806	0.0165	0.1463	0.0527	0.2961
4 0 $\bar{4}$ 28	0.759	0.0357	0.0106	0.0623	0.0245	0.1331
5 0 $\bar{5}$ 35	0.607	0.0192	0.0087	0.0321	0.0154	0.0754
6 0 $\bar{6}$ 42	0.506	0.0132	0.0079	0.0189	0.0117	0.0517
7 0 $\bar{7}$ 49	0.433	0.0100	0.0076	0.0123	0.0099	0.0398
1 $\bar{1}$ 0 8	2.782	1.7607	0.2827	2.7972	1.1919	6.0325
2 $\bar{2}$ 0 16	1.391	0.2146	0.0351	0.3752	0.1379	0.7628
3 $\bar{3}$ 0 24	0.928	0.0630	0.0141	0.1132	0.0412	0.2315
4 $\bar{4}$ 0 32	0.696	0.0281	0.0097	0.0482	0.0201	0.1061
5 $\bar{5}$ 0 40	0.557	0.0163	0.0083	0.0249	0.0133	0.0628
6 $\bar{6}$ 0 48	0.464	0.0113	0.0077	0.0148	0.0106	0.0444
1 0 $\bar{1}$ 10	2.353	1.0638	0.1673	1.7316	0.7095	3.6722
2 0 $\bar{2}$ 20	1.176	0.1286	0.0230	0.2288	0.0824	0.4628
3 0 $\bar{3}$ 30	0.784	0.0389	0.0111	0.0688	0.0265	0.1453
4 0 $\bar{4}$ 40	0.588	0.0185	0.0086	0.0293	0.0146	0.0710
3 0 $\bar{3}$ 18	1.099	0.1046	0.0197	0.1871	0.0672	0.3786
6 0 $\bar{6}$ 36	0.550	0.0158	0.0082	0.0240	0.0131	0.0611
0 3 $\bar{3}$ 18	1.099	0.1046	0.0197	0.1871	0.0672	0.3786
0 6 $\bar{6}$ 36	0.550	0.0158	0.0082	0.0240	0.0131	0.0611

$$hki0: -h + k = 3n \tag{1.24}$$

$$hh2\bar{h}l: l = 3n \tag{1.25}$$

$$h\bar{h}0l: h + l = 3n, l = 2n \tag{1.26}$$

$$000l: l = 6n \tag{1.27}$$

$$h\bar{h}00: h = 3n \tag{1.28}$$

Thus some harmonics do not appear in the list of Tables 1.3a and 1.3b.

The process for the calculation of other components of eq. (1.17), *i.e.* $N_0(\lambda)$, $f_2(\lambda)$ and $f_3(\lambda)$, can be obtained via a similar method. Fig. 1.16 shows graph of the relationship between the attenuation length D and X-ray energy for AgBr, which is needed for the calculation of $f_3(\lambda)$ (see eq. 1.21).

After calculating the components of eq. (1.17), the relative contribution of each harmonic to the integrated topograph intensity can be estimated using the normalized number of photons, $N'_{abs}(\lambda)$, absorbed in the recording film during exposure. In this study $N'_{abs}(\lambda)$ is calculated by dividing $N_{abs}(\lambda)$ of each harmonic by the largest $N_{abs}(\lambda)$ value among all harmonics. Table 1.4a and Table 1.4b list the calculation results for sapphire back reflections listed in Tables 1.3a and 1.3b. The calculation results in Tables 1.4a and 1.4b indicate that for many reflections, such as the 1 0 $\bar{1}$ 10 reflection, the topograph contrast is actually a mixed contribution from several harmonics.

Eq. (1.11) indicates that in order to calculate the penetration depth, t_p, of the studied sample, its effective linear absorption coefficient μ must be known. In this study, the X- ray penetration depth in sapphire crystal is studied [4], and its effective linear absorption coefficient μ can be easily obtained from the relationship between the attenuation length D and X-ray energy for sapphire (see Fig. 1.17).

Fig. 1.18 shows the geometry of the X-ray reflection in topography experiments. For the large angle incident X-rays, in order to calculate the penetration depth, eq. (1.11) indicates that the incident angle ϕ_0 and exit angle ϕ_n of the X-rays should be known in addition to the effective linear absorption coefficient, μ, of the sample. As only the penetration depths for back reflection topographs are required in this study, eq. (1.11) can be expressed as:
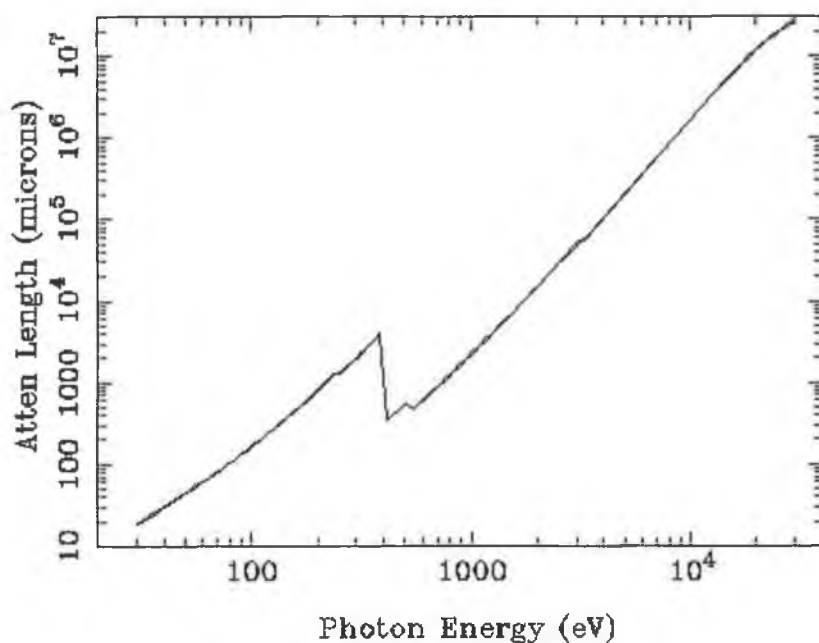
AgBr Density=6.473, Angle=90.deg
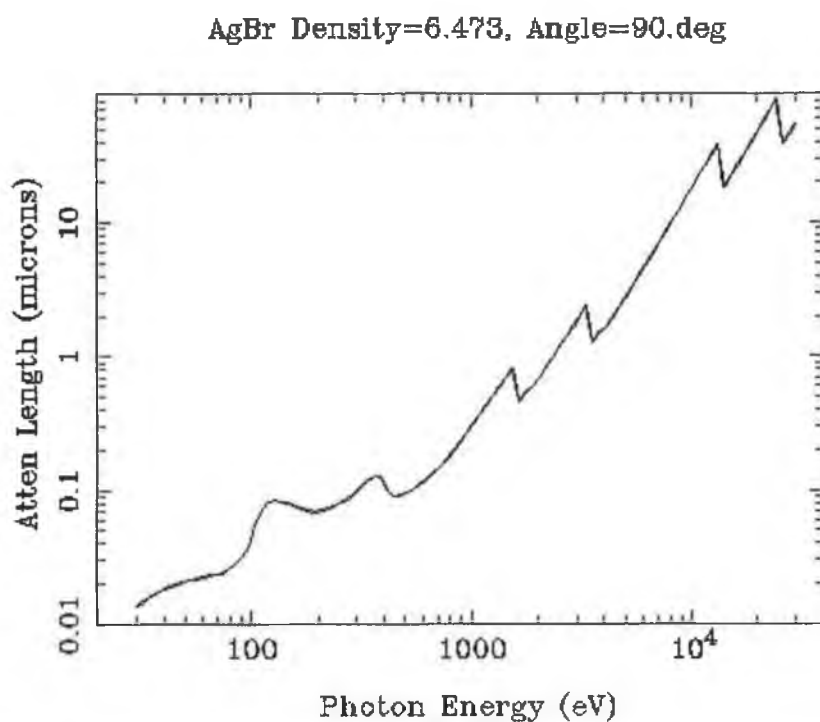
Figure 1.16: Relationship between the attenuation length and X-ray energy for AgBr.

Al2O3 Density=3.97, Angle=90.deg

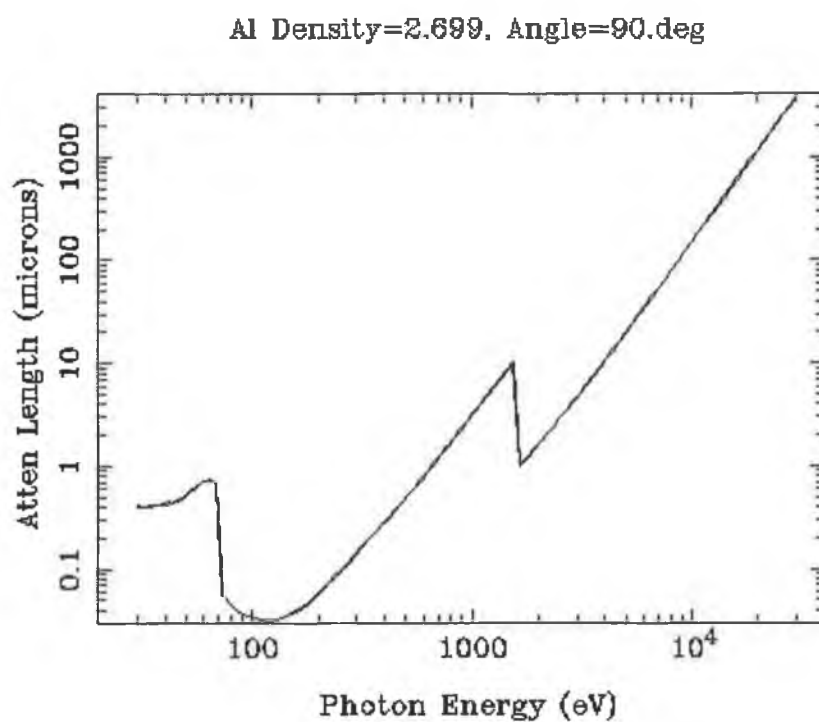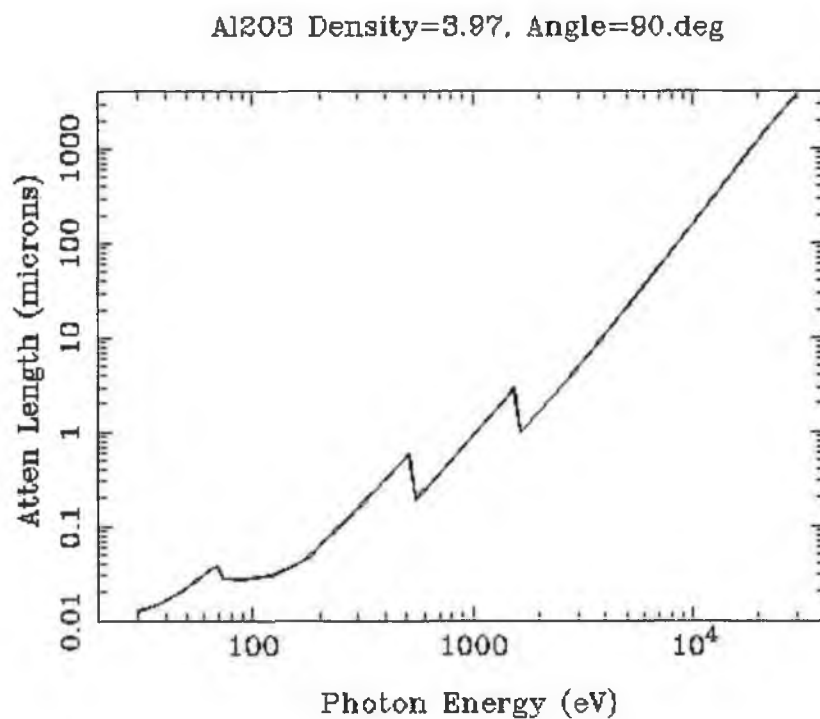**Figure 1.17:** Relationship between the attenuation length and X-ray energy for sapphire.

Table 1.4a Estimation of photon count absorbed by the film during a (0001) sapphire white beam synchrotron X-ray back reflection topography exposure.

Index of reflection	X-Ray wavelength (Å)	$N_0(\lambda)$	$f_1(\lambda)$	$f_2(\lambda)$	$f_3(\lambda)$	$N_{abs}(\lambda)$	$N'_{abs}(\lambda)$	t_p (μm)
1 1 $\bar{2}$ 12	1.832	0.547c	0.166	82.084k	0.549	4.083kc	0.794	21
2 2 $\bar{4}$ 24	0.916	1.251c	0.805	19.713k	0.259	5.140kc	1	163
3 3 $\bar{6}$ 36	0.611	1.731c	0.942	0.859k	0.096	0.134kc	0.026	
4 4 $\bar{8}$ 48	0.458	1.942c	0.976	0.634k	0.112	0.134kc	0.026	
1 $\bar{2}$ 1 12	1.829	0.549c	0.166	81.588k	0.549	4.071kc	0.796	21
2 $\bar{4}$ 2 24	0.914	1.252c	0.805	19.584k	0.259	5.112kc	1	162
3 $\bar{6}$ 3 36	0.609	1.733c	0.942	0.853k	0.096	0.134kc	0.026	
4 $\bar{8}$ 4 48	0.457	1.942c	0.976	0.630k	0.112	0.134kc	0.026	
$\bar{1}$ 0 1 11	2.151	0.443c	0.055	196.169k	0.731	3.473kc	1	14
$\bar{2}$ 0 2 22	1.076	1.055c	0.698	3.361k	0.172	0.426kc	0.123	110
$\bar{3}$ 0 3 33	0.719	1.546c	0.887	0.599k	0.146	0.120kc	0.035	
$\bar{4}$ 0 4 44	0.514	1.880c	0.961	0.836k	0.068	0.103kc	0.030	
$\bar{5}$ 0 5 55	0.430	1.956c	0.981	0.367k	0.096	0.068kc	0.020	
2 $\bar{2}$ 0 22	1.082	1.046c	0.698	3.417k	0.172	0.429kc	1	111
4 $\bar{4}$ 0 44	0.541	1.841c	0.960	0.974k	0.070	0.120kc	0.280	830

$N'_{abs}(\lambda)$: Normalized value for $N_{abs}(\lambda)$.

Table 1.4b Estimation of photon count absorbed by the film during a (0001) sapphire white beam synchrotron X-ray back reflection topography exposure.

Index of reflection	X-Ray wavelength (Å)	$N_0(\lambda)$	$f_1(\lambda)$	$f_2(\lambda)$	$f_3(\lambda)$	$N_{abs}(\lambda)$	$N'_{abs}(\lambda)$	t_p (µm)
1 0 $\bar{1}$ 7	3.035	0.287c	0.0004	121.550k	0.951	0.014kc	0.001	
2 0 $\bar{2}$ 14	1.517	0.728c	0.371	138.810k	0.384	14.090kc	1	34
3 0 $\bar{3}$ 21	1.012	1.165c	0.744	15.390k	0.147	1.960kc	0.139	115
4 0 $\bar{4}$ 28	0.759	1.522c	0.875	7.020k	0.166	1.550kc	0.110	270
5 0 $\bar{5}$ 35	0.607	1.765c	0.927	0.811k	0.095	0.125kc	0.009	
6 0 $\bar{6}$ 42	0.506	1.910c	0.950	0.521k	0.059	0.055kc	0.004	
7 0 $\bar{7}$ 49	0.433	1.974c	0.961	0.620k	0.098	0.115kc	0.008	
1 $\bar{1}$ 0 8	2.782	0.319c	0.002	628.990k	0.911	0.438kc	0.052	6
2 $\bar{2}$ 0 16	1.391	0.814c	0.466	69.870k	0.317	8.415kc	1	47
3 $\bar{3}$ 0 24	0.928	1.272c	0.793	2.190k	0.117	0.259kc	0.031	
4 $\bar{4}$ 0 32	0.696	1.624c	0.899	3.400k	0.134	0.666kc	0.079	369
5 $\bar{5}$ 0 40	0.557	1.845c	0.939	1.290k	0.076	0.169kc	0.020	
6 $\bar{6}$ 0 48	0.464	1.948c	0.957	1.350k	0.116	0.292kc	0.035	
1 0 $\bar{1}$ 10	2.353	0.408c	0.025	741.700k	0.790	6.076kc	1	11
2 0 $\bar{2}$ 20	1.176	0.990c	0.630	34.547k	0.214	4.601kc	0.757	84
3 0 $\bar{3}$ 30	0.784	1.479c	0.865	12.920k	0.180	2.974kc	0.489	279
4 0 $\bar{4}$ 40	0.588	1.800c	0.932	1.181k	0.087	0.173kc	0.028	
3 0 $\bar{3}$ 18	1.099	1.068c	0.685	41.800k	0.181	5.523kc	1	79
6 0 $\bar{6}$ 36	0.550	1.855c	0.941	0.662k	0.073	0.084kc	0.015	
0 3 $\bar{3}$ 18	1.099	1.068c	0.685	41.800k	0.181	5.523kc	1	79
0 6 $\bar{6}$ 36	0.550	1.855c	0.941	0.662k	0.073	0.084kc	0.015	

$N'_{abs}(\lambda)$: Normalized value for $N_{abs}(\lambda)$.
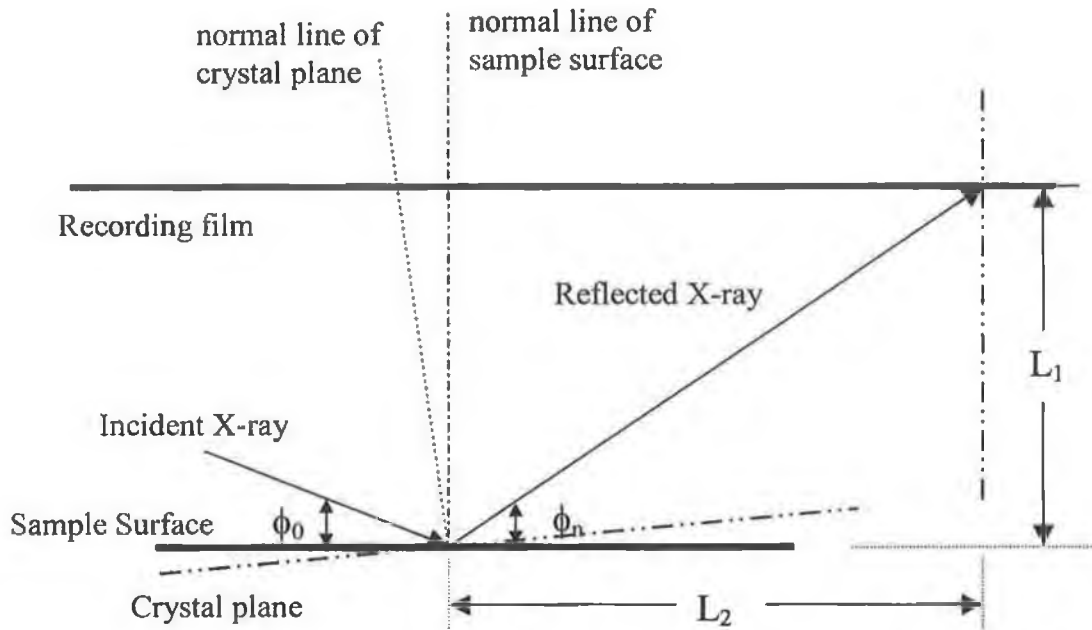
Figure 1.18: Schematics for the geometry of reflection in back reflection topography.

$$t_p = [\mu(\tfrac{1}{\sin 90} + \tfrac{1}{\sin \phi_n})]^{-1} = [\mu(1 + \tfrac{1}{\sin \phi_n})]^{-1} \qquad (1.29)$$

The exit angle ϕ_n can be measured easily with the following expressing:

$$\phi_n = \tan^{-1}(\tfrac{L_1}{L_2}) \qquad (1.30)$$

where L_1 is the distance from sample to film and L_2 is the distance from the reflection spot to the film centre, where the incoming X-ray passes through a hole in the film for the back reflection experimental set-sup.

The calculated penetration depths for some sapphire reflections are listed in Tables 1.4a and 1.4b.

References

1. M. Sauvage-Simkin, X-Ray topography and related techniques using synchrotron radition, pp:179-204.

2. T. Tuomi, K. Naukkarinen, P. Rabe, Physica Status Solidi A. **25,** 93 (1974).

3. W.M. Chen, P.J. McNally, Yu.V. Shvyd'ko, T. Tuomi, A.N. Danilewsky, M. Lerche, J. Cryst. Growth, **252**, 113 (2003).

4. W.M. Chen, P.J. McNally, Yu.V. Shvyd'ko, T. Tuomi, M. Lerche, A.N. Danilewsky, J. Kanatharana, D. Lowney, M. O'Hare, L. Knuuttila, J. Riikonen, R. Rantamäki, Phys. Status Solidi A, **186,** 365 (2001).

5. W.M. Chen, P.J. McNally, K. Jacobs, T. Tuomi, A.N. Danilewsky, D. Lowney, J. Kanatharana, L. Knuuttila, J. Riikonen, Mat. Res. Soc. Symp. Proc., **693**, 141 (2002).

6. http://img.cryst.bbk.ac.uk/www/kelly/historyoftopography.htm

7. M. Sauvage, J. F. Petroff, H. Winick and S. Doniach, Synchrotron Radiation Rresearch, Plenum, New York, NY, USA. pp. 607-38, 1980

8. W.M. Chen, P.J. McNally, K. Jacobs, T. Tuomi, A.N. Danilewsky, Z.R. Zytkiewicz, D. Lowney, J. Kanatharana, L. Knuuttila, J. Riikonen, J. Cryst. Growth, **243**, 94 (2002).

9. http://www-hasylab.desy.de/

10. H. Marchand, X.H. Wu, J.P. Ibbetson, P.T. Fini, P. Kozodoy, S. Keller, J.S. Speck, S.P. DenBaars, U.K. Mishra, Appl. Phys. Lett. 73 (1998) 747

11. A. Sakai, H. Sunakawa, A. Usui, Appl. Phys. Lett. 71 (1997) 2259

12. S. Nakamura, M. Senoh, S. Nagahama, N. Iwasa, T. Matushita, T. Mukai, MRS Internet J. Nitride Semicond. Res. 4S1, G1.1 (1999); http://nsr.mij.mrs.org/4s1/g1.1/

13. http://www.spring8.or.jp/ENGLISH/general_info/overview/

14. A. Authier, Dynamical Theory of X-Ray Diffraction, Oxford University press, 2001, and reference therein.

15. J. Schwinger, Phys. Rev., **75**, (1949), 1912.

16. D. K. Bowen, B. K. Tanner, High Resolution X-ray Diffractometry and Topography, Taylor and Francis, 1998.

17. P.J. McNally, J.W. Curley, M. Bolt, A. Reader, T. Tuomi, R, Rantamäki, A.N. Danilewsky, I. DeWolf, J. Mater. Sci.:Materials in Electronics, **10** (1999) 351

18. P.J. McNally, R. Rantamaki, T. Tuomi, A.N. Danilewsky, D. Lowney, J. W. Curley, P.A.F. Herbert. IEEE Trans. Comp. Packag. Technol., **24**, (2001) 76.

19. http://www.ccp14.ac.uk/ccp/web-mirrors/lmgp-laugier-bochu/

20. R. Rantamäki, T. Tuomi, P.J. McNally, P.J. Curley, A.N. Danilewsky, J. X-ray Sci. Technol. **8** (1998) 159.

21. http://www-cxro.lbl.gov/optical_constants/

22. H. Dosch, Phys. Rev., B**35** (1987) 2137.

23. K. Stoev, K. Sakurai, Rigaku Journal **14**, (1997) 22.

24. M. Hart, J. Appl. Cryst. **8** (1975) 436.

25. C. L. Kuo, J. C. Bilello, J. Appl. Phys. **62**, (1987) 137.

26. H. Winick, in: Synchrotron Radiation Research, H. Winick and S. Doniach, eds, Plenum Press, New York, 1980, P.16.

27. http://jcrystal.com/steffenweber/dos/xrdiff.html

28. B.D. Cullity, Elements of X-ray diffraction, 2nd edition. Addison-Wesley. 1978, London, UK.

29. J. B. Bilde-Sorensen, B. F. Lawlor, T. Geipel, P. Pirouz, A. H. Heuer and K. P. D. Lagerlof, Acta Mater. **44**, (1996) 2145.

30. P. Pirouz, B. F. Lawlor, T. Geipel, J. B. Bilde-Sorensen, A. H. Heuer and K. P. D. Lagerlof, Acta Mater. **44**, (1996) 2153.

31. T. Geipel, J. B. Bilde-Sorensen, B. F. Lawlor, P. Pirouz, K. P. D. Largerlof and A. H. Heuer, Acta Mater. **44**, (1996) 2165.

32. International tables for crystallography. Vol.A. Space-group symmetry. Second, revised edition. Reidel. 1987, Dordrecht, Netherlands.

33. http://www.esrf.fr/exp_facilities/ID19/homepage/DiffTopo/X-raytopography.htm#1.introduction.

2 Basic theory of dislocations and practice for semiconductors

2.1 Introduction

A dislocation is one kind of line defect in a crystal. They can have complex effects on the performance and reliability of the devices produced thereon, and their origin is complicated, especially in the heteroepitaxial films. In general, dislocations tend to have adverse effects on electronic devices, though occasionally they can have positive effects. Dislocations appear in most crystalline materials, such as semiconductors. The impact of dislocations has interested many scientists from different fields and has been extensively studied in the past two generations. In this chapter, some concepts related to dislocations are introduced, and the origins and effects of dislocations on semiconductor materials and devices are briefly reviewed. Some preventive methods and characterization techniques for dislocations are also presented.

2.2 Concepts and properties of dislocations

2.2.1 Type and properties of dislocations

There are two main kinds of pure dislocation, i.e. the edge dislocation and the screw dislocation. An edge dislocation can be formed when stress is applied to a crystal so that the lower part moves with respect to the upper part. In this dislocation, an extra plane of atoms is inserted into the upper plane. Another kind of dislocation is the screw dislocation; in this case the slip direction is parallel to the dislocation line. The schematics for edge and screw dislocations are shown in Fig. 2.1. The dislocation line [1] is defined as the boundary between the slipped and unslipped parts of a crystal. An important concept related to the dislocation is the Burgers vector, which is a unit slip distance for the dislocation and is always parallel to the direction of slip. The Burgers vector can be determined by carrying out a circuit
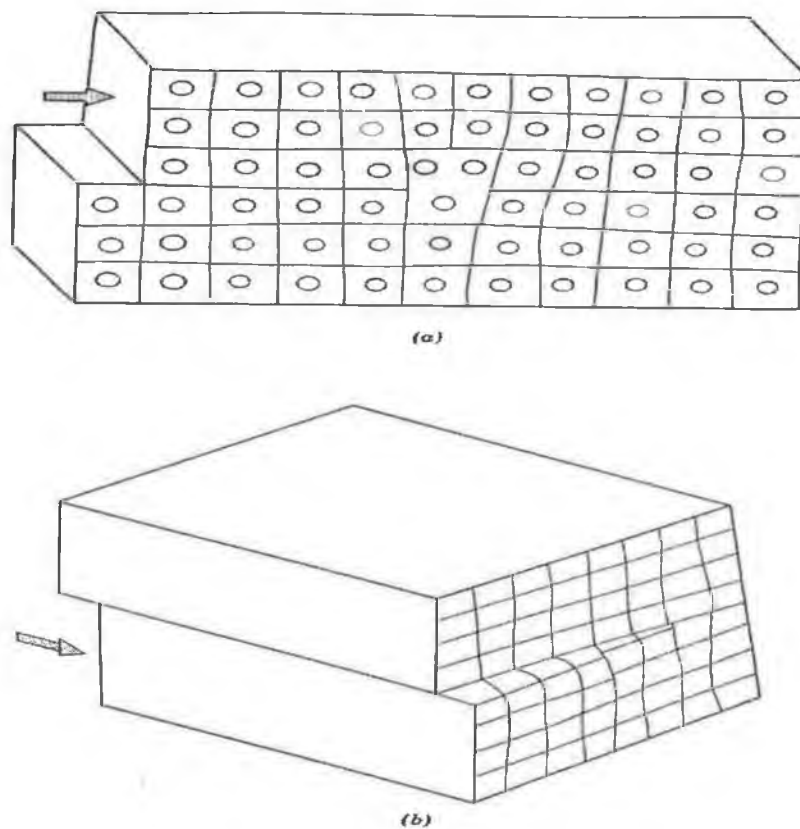
Fig. 2.1 Schematics for (a) Pure edge and (b) Pure screw dislocations occurring during plastic deformation [1].

count of atoms on lattice positions around the dislocation [1]. The dislocation line in the pure edge dislocation is perpendicular to the Burgers vector, while in the pure screw dislocation, it is parallel to the Burgers vector. When a screw dislocation and edge dislocation are combined, a mixed dislocation is then formed. Fig. 2.2 shows the schematics for pure screw (left), pure edge (right) and mixed dislocations (middle). Some of the important properties of dislocations are listed as follows [2]:

1. For a given dislocation, there is only one Burgers vector b regardless of the shape of the dislocation line.

2. A dislocation must end on itself, thus forming a loop, or on other dislocations, thus forming a network, or on surfaces such as an external surface or a grain boundary.

3. In general, dislocations in real crystals form three-dimensional networks.
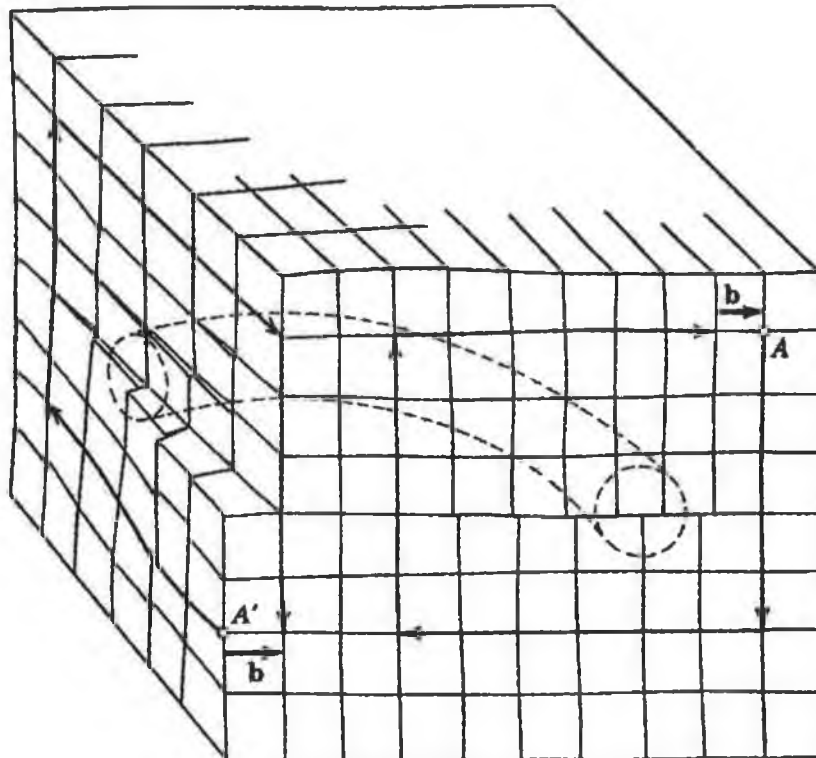
Fig. 2.2 Combination of edge and screw dislocations. Burgers vector b shown for pure screw and for pure edge. The dotted dislocation line connecting these is shown also [1].

The sum of the Burgers vectors at the node or point of junction of the dislocations is zero.

4. The slip (or glide) plane of a dislocation contains the dislocation line and its Burgers vector.

The existence of crystal dislocations was first postulated independently by several scientists in 1934 to explain plastic deformation. But it was not directly observed in real crystals until 1953 [1]. Dislocations disturb the regular atomic arrangement in crystals, and an elastic strain field is created after the dislocation forms. For example, atoms around the upper part of a positive edge dislocation experience a tensile stress, and the lower atoms bear a compressive stress. An approximate relationship for the strain energy per unit length of a dislocation (edge, screw or mixed dislocation) can be written as [1]:

$$E = \alpha G b^2 \hspace{5cm} (2.1)$$

where $\alpha \approx 0.5\text{-}1.0$, is a constant, G is the shear modulus of elasticity, and b is the magnitude of the Burgers vector. As can be seen from equation (2.1), dislocations with the smallest Burgers vector have the lowest strain energy and consequently are the most likely to form.

2.2.2 Origin of dislocations in (semiconductor) crystals

Depending on the required application, both bulk and thin film materials are used in semiconductor technology. Dislocations in bulk and thin films have different origins. Dislocations in bulk crystals have three main sources [3]: (1) dislocations present in a seed crystal could propagate into a growing crystal; (2) point defects could cluster to form dislocation loops during the cool down, and they may undergo multiplication, resulting in highly dislocated crystals; (3) under the influence of thermal-gradient-induced stresses, dislocations present in the peripheral regions of a growing crystal could propagate into the interior of the crystal. The thermal-gradient-induced stresses are a major source of dislocations in III-V crystal semiconductors.

Thin films can be produced in many ways, consisting of physical, chemical or mixed methods, such as vapour phase epitaxy (VPE), metalorganic chemical vapour deposition (MOCVD), plasma-induced molecular beam epitaxy (PIMBE) [4], etc. Sometimes multilayer epitaxial structures are required for many devices [5].

If the film is deposited over the same type of material, the process is called homoepitaxy, such as Si thin film deposited over a Si substrate. Usually the thin film material is different from that of the substrate, such as a GaAlAs film upon a GaAs substrate, $Si_{1-x}Ge_x$ epilayer on a Si substrate, etc. and this process is called heteroepitaxy.

The concept of misfit is important in the heteroepitaxy technique, which is defined as:

$$\varepsilon\% = \left| \frac{a_s - a_f}{a_s} \times 100 \right| \tag{2.2}$$

where a_s is the lattice parameter for the substrate, and a_f is the lattice parameter for the thin film.

By growing a semiconductor overlayer on top of a thick substrate, a large strain can be built into the overlayer [5-6], while still maintaining crystallinity and long-range order. The following rules are useful in the heteroepitaxy process [2].

1. If ε is less than ε_{c1} (~10%), the first monolayer has no dislocations. If ε lies between ε_{c1} and ε_{c2} (~14%), the lowest energy state of a monolayer has dislocations running along the monolayer, although the dislocations may not be generated in a metastable state. If $\varepsilon > \varepsilon_{c2}$, dislocations will be always generated in the very first monolayer and the thick overlayer may continue growth in a different orientation than the substrate.

2. For $\varepsilon < \varepsilon_{c1}$, it is possible to divide the overlayer thickness d into two regions: $d < d_c$ (the critical thickness), where the overlayer grows in coherence with the substrate (i.e. no dislocations are produced, and the thin film is pseudomorphic); $d > d_c$, where dislocations are produced at the interface and overlayer grows with its own bulk lattice constant.

The critical thickness is an important concept in thin film growth and will be introduced in section 2.2.3.

The strain in the overlayer will relax after dislocations are produced [5], but pseudomorphic films below critical thickness are thermodynamically stable, i.e. the relaxed state with dislocations has a higher free energy.

As stated above in the film-substrate system, the most favorable site for dislocation formation is the film-substrate interface [3, 7-9].

For epilayers there are two main categories of defects, i.e. growth-process-independent and growth-process-dependent defects. Dislocations are usually growth-process-independent defects. In homoepitaxial and lattice-matched heteroepitaxial layers, threading dislocations in the substrate are the major source of dislocations [3, 10]. For lattice-unmatched heteroepitaxial layers, the linear density ρ of misfit dislocations, i.e. the number per unit length, is given by [10]

$$\rho = \frac{a_f - a_s}{a_f * a_s} \tag{2.3}$$

where a_s and a_f are the unstrained lattice parameters of the substrate and the epilayer respectively.

2.2.3 Critical thickness

The critical thickness (d_c) is the thickness of the deposited epilayer above which dislocation generation is favored and the strain relaxes. A rough theoretical estimate is given by [2] equation (2.4),

$$d_c \sim \frac{a}{2\varepsilon} \tag{2.4}$$

where a is the lattice constant and ε is the misfit. Another simple empirical expression for the critical thickness is given by Blaqnc [2], which is:

$$d_c \sim \frac{b}{2\varepsilon} \tag{2.5}$$

where b is the magnitude of the Burgers vector of the dislocation.

However the onset of the critical thickness is often not abrupt and depends upon the growth conditions, since growth is carried out away from equilibrium conditions. It depends on the structure and elastic properties of the materials, and the type of dislocation [8] as well. As a result, the reported critical thicknesses for similar mismatched epitaxial systems often differ from each other.

2.2.4 Movement of dislocations in semiconductors

There are several mechanisms for the movement of dislocations in a crystal, such as climb and slip. Dislocation climb is the movement of dislocations out of their slip planes, which is defined by the position of the dislocation line and the Burgers vector of the dislocation [45]. It requires a diffusional jump of an atom above the

dislocation line into the dislocation. This is equivalent to the motion of the dislocation into the adjacent plane. Slip means the movement of a dislocation along its slip planes.

In general dislocation mobility in semiconductor materials is very low compared to that in metals. As a result, if material is deposited rapidly and at a relatively low temperature, films with low dislocation densities can be grown to thicknesses well beyond the critical thickness. Such films are very resistant to dislocation formation if they are cooled to low temperature as they are in a metastable state, thus making it nearly impossible for the formation of new dislocations from the point view of dynamics.

Dislocations tend to have different mobilities along different crystalline directions [11-12]. For example, dislocations lying along the two <110> directions in a (001) plane of GaAs have different activation energies [11].
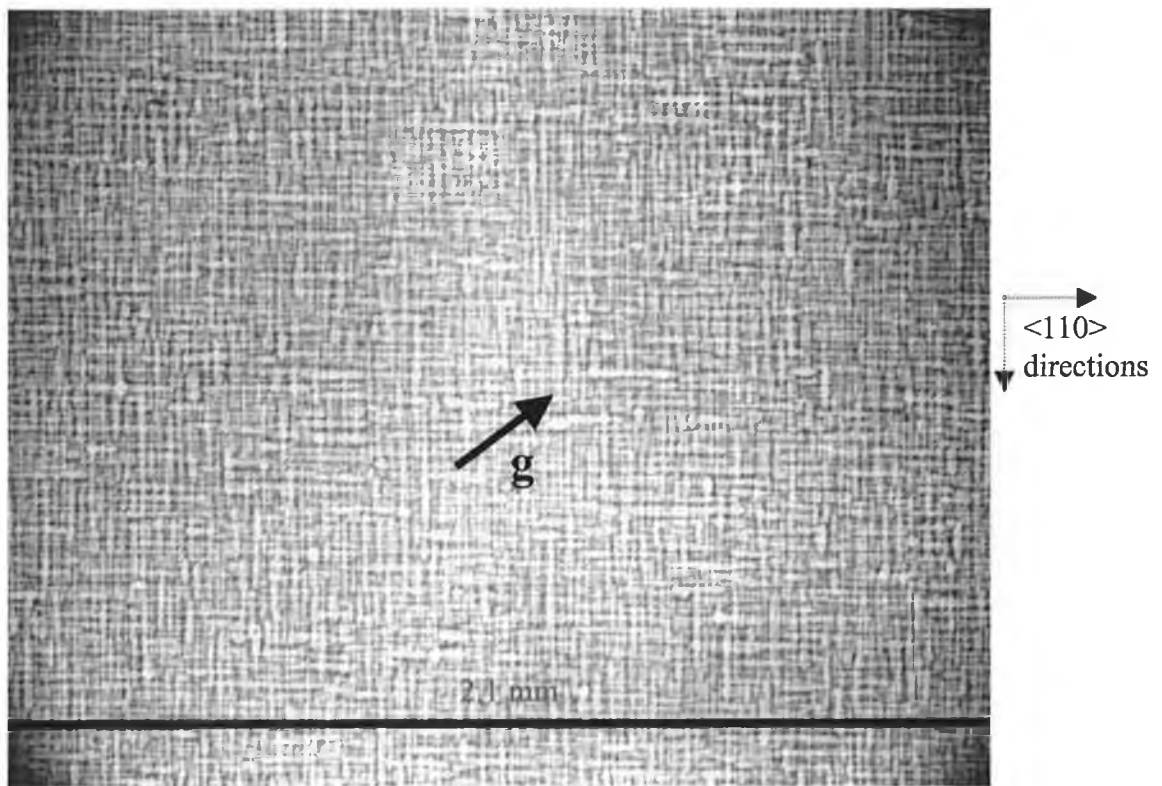
Figure 2.4 Crosshatch of misfit dislocations observed in the $Si_{1-x}Ge_x$ virtual substrates with the large area back reflection topography, (013) reflection.

During the growth of relaxed SiGe buffers, the inhomogeneous misfit dislocation densities in the graded buffer form regions of more severe crosshatch on the surface that will impede the dislocation flow [13]. A crosshatch is the two groups of misfit dislocations formed along the two perpendicular <110> directions when, for example, growing $Si_{1-x}Ge_x$ virtual substrates over Si substrates. Such an example is shown in Fig. 2.4, which is a large area back reflection topograph of the sample measured with micro-Raman spectroscopy in this study (see chapter 5). Fig. 2.4 clearly shows two perpendicular dislocation groups along the two <110> directions. By using chemomechanical planarization (CMP), deleterious pile-up formation can be avoided, and previously formed pile-ups can be destroyed by regrowth of a graded layer [13].

2.3 Effects of dislocations on the performance of semiconductor devices

Dislocations in semiconductor materials usually have prominent effects on the performance of devices. As they provide easy diffusion paths for dopants, which can lead to short circuits across film layers, they cause band bending [3], which can result in a resistivity increase in the semiconductor. Dislocations can act as acceptors or donors in a semiconductor and thus also change the electrical performance. For example, in n-type materials, dangling bonds related to the dislocations can accept electrons from energy states in the conduction band to form pairs, thus behaving as acceptors. On the other hand, dislocations in p-type materials can act as donors. The strain induced by dislocations in the semiconductor also affect its performance; sometimes dislocations provide recombination centers which reduce the charge carrier density, and they interfere with subsequent deposition by providing sites for defect nucleation, growth and multiplication [9].

Defects in crystals often cause device degradation (including rapid degradation, gradual degradation and catastrophic degradation) and are a major hindrance to device reliability [8].

In general, dislocations have dramatic effects on minority carrier devices [3, 10], such as solar cells, light emitters, bipolar transistors, photodetectors, etc. The performance, yield, reliability and degradation behavior of minority carrier devices are adversely affected by the presence of defects [3]. One study showed that when a compressive load was applied to diffused GaAs electroluminescent diodes, their degradation rate increases by an order of magnitude and the degradation was accompanied by the multiplication of dislocations [14]. Other studies showed [15] that the breakdown voltage for an n-type InP based diode reduces substantially when the dislocation density increases from 2.2×10^7 to 1.5×10^8 cm^{-2}, and in reverse bias the leakage current dramatically increased. In contrast, the impact of dislocations on majority carrier devices (for example, MOSFETs) is not so dramatic [3].

Luminescent properties are important for the operation of light emitting devices. Dislocations may have a great influence on the luminescent properties. However the effects of dislocations on the performance of semiconductor devices vary with type and orientation. For example [16], the yellow luminescence of GaN was related to the presence of screw dislocations with $\vec{b} = [0001]$, but it is not

significantly influenced by edge-type dislocations. It may be that edge-dislocations induce only shallow levels in the bandgap, while screw dislocations may form deep levels. The yellow luminescence acts as the lifetime killer and suppresses the desired UV luminescence. Electron microscopy and cathodoluminescence [4] results suggest that the yellow luminescence relates to dislocations at low-angle grain boundaries or point defects nucleated at the dislocations, and the band-to-band UV luminescence originates from the bulk of the crystal.

Evidence also shows that recombination-enhanced dislocation climb and glide are responsible for the rapid degradation of optical devices [8], such as GaAlAs/GaAs double-heterostructure light-emitting diodes or InGaAsP/InGaP double-heterostructure lasers.

A recent experimental result indicated [17] that dislocations reduced the sapphire crystal reflectivity when it is used in X-ray optics. Defects in sapphire crystal will also affect its transparency [44] when it is used as a transparent window material. In all of these cases it is clear that dislocations should be suppressed during growth of bulk or epitaxial crystal materials to improve the performance and reliability of the devices, etc. A dislocation analysis in crystals, such as, sapphire, is an essential prerequisite for improvement of the crystal quality, and can provide useful information for the manufacturers about the defects inside the crystal material.

In most situations, dislocations have adverse effects on electronic devices. However if the dislocations generated are all confined to the substrate-overlayer interface, their effects are not felt in the active region of the overlayer where the devices are to be fabricated. Furthermore, dislocations in this interface region may absorb defects and hazardous dopants in the active layer, leading to improvements in the performance and reliability of the devices [2]. Dislocations are sometimes used as electronic elements on a semiconductor chip to make the smallest transistor [18]. Sometimes scientists take advantage of the presence of dislocations to develop new products and improve the device performances [5, 9, 19]. For example, lattice-mismatched semiconductor systems have been extensively investigated for the realization of strained-layer devices [5, 19]. On the other hand, if the dislocations thread through the growing overlayer, they will propagate in the overlayer and cause deterioration of active devices fabricated in the overlayer.

2.4 Preventive methods for dislocations in semiconductors

Depending on which semiconductor process is used, the preventive methods for dislocations are quite different. For bulk semiconductor, usually all dislocations present in the seed will be incorporated into the as-grown crystals. Using small-diameter seeds [20-21] could reduce the magnitude of the thermal stresses, thus lowering the dislocation density in the bulk crystal. The procedure of forming a neck by an initial rapid pull of the growing bulk crystal could also prevent the propagation of dislocations from the seed into the crystal [22].

One approach to growing crystals of compound semiconductors with lower dislocation densities is to reduce the magnitudes of the thermoelastic stresses to low levels so that the slips are not activated [23-25]. However it is not easy to operate in practice, as the yield stresses of compound semiconductors at high temperature are very low [23-25]. Some intentionally introduced impurities can reduce the dislocation density as they can strengthen the matrix, thus improving the yield stress [26-28].

For thin epitaxial films, several schemes have been proposed [3] to lower the density of threading dislocations in lattice mismatched layers: (i) graded buffer layers [5, 19]; (ii) growth on compliant substrates; (iii) epitaxial lateral overgrowth [6, 29-30].

By selecting materials and dimensions carefully, it is theoretically possible to force dislocations to form and to propagate them into the substrate rather than into the film [9], thus leaving the film surface unaffected. Some preliminary experimental results have proved this possibility. In Christiansen's experiment [16], he and his colleagues found that dislocations reacted with each other or bent back to the interface, so that a reduced density of surviving dislocations was observed at a height larger than 400 nm above the interface.

In order to produce strained-layer devices, misfit dislocations must be eliminated. This can be achieved by preventing the nucleation of misfit dislocation, by minimizing dislocation multiplication, and limiting the glide of existing misfit dislocations [11].

By limiting the lateral dimension of the sample before film growth, the interface dislocation density may be reduced, as too few threading dislocations would be present to nucleate a large number of misfit dislocations. This method is

believed [11] to be useful for any nucleation sources that depend on area. If non-area-dependent nucleation sources become active, the reduction of dislocation density with growth area will still be observed, but the lowest achievable dislocation density will be higher than if these sources were not active. The results for quality improvement of the Epitaxial Lateral Overgrowth (ELO) epilayers compared with non-ELO samples can be found in many studies [29, 31-37].

In addition, chemomechanical planarization (CMP) and regrowth of graded layers are also effective methods in reducing the threading dislocation density [13].

2.5 Characterization methods for dislocations in semiconductors

2.5.1 Etch method

The strain energy of a dislocation leads to a faster rate of chemical etching at the point of emergence of a dislocation at a free surface, resulting in the formation of etch pits at such points. Similarly, because of the strain energy, dislocations act as catalytic sites for precipitation from solid solution. So it is possible to decorate the dislocations which intersect the free surfaces with Cu, etc. By using this method, dislocations may be revealed by various optical techniques. It is the earliest characterization method for dislocations, but it cannot reveal those dislocations located inside the sample [38].

2.5.2 Transmission electron microscopy (TEM)

Because of the contrast difference between the perfect and dislocated area, TEM is able to detect dislocations in semiconductor materials. The high resolution capability of TEM makes it a powerful and exact tool for the characterization of dislocations. However the TEM method is a destructive method, and the cost and time needed for preparing the sample limits its widespread application [31, 34, 39].

2.5.3 High resolution x-ray diffractometry and topography

Threading dislocation densities may be determined with x-ray diffraction methods by using the linewidth of x-ray rocking curves combined with computational simulation [41].

The topography method for dislocation characterisation has been introduced in Chapter 1. With the help of synchrotron radiation sources, synchrotron x-ray topography techniques (SXRT) have become powerful and versatile characterisation tools for dislocation analysis.

In comparison with other characterization techniques, such as transmission electron microscopy (TEM), X-ray topography enables large area measurements, for example, 5 mm x 5 mm, and this is very useful in obtaining wafer quality assessment and dislocation density calculations [11, 17, 42]. Consequently, the SXRT technique was employed to characterize dislocations in a number of crystal materials in this study.

Many other techniques have also been developed to characterize dislocations in semiconductors, some of which include cathodoluminescence [7, 40], photoluminescence (PL) [43], etc.

2.6 Summary

Dislocations have been studied for almost 70 years, and still their impact on semiconductors and devices are not understood completely. It is not easy to produce perfect semiconductors, especially compound semiconductors, though much progress has been achieved in recent decades. Many questions still need to be answered by materials scientists and process technologists. These include an understanding of how do dislocation interactions influence the process during elastic strain relaxation in epitaxial heterostructures with mismatch beyond critical thickness? Researchers would also like to know if there is a more direct means of controlling threading dislocation density in epitaxial films.

References

1. W. D. Kingery, H. K. Bowen, D. R. Uhlmann, Introduction to ceramics (John Willey & Sons, 1976).

2. J. Singh, Physics of semiconductors and their heterostructures (McGraw-Hill, 1993).

3. S. Mahajan, Acta Mater., **48**, 137 (2000).

4. O. Ambacher, J. Phys. D: Appl. Phys., **31**, 2653 (1998).

5. W.M. Chen, G.D.M. Dilliway, P.J. McNally, T. Tuomi, A.F.W. Willoughby, J. Bonar, J. Mater. Sci. - Mater. Electron, **14**, 455 (2003).

6. W.M. Chen, P.J. McNally, K. Jacobs, T. Tuomi, J. Kanatharana, D. Lowney, L. Knuuttila, J. Riikonen, J. Toivonen, J. Mater. Sci. - Mater. Electron, **14**, 283 (2003).

7. C. Zanotti Fregonara, G. Salviati, M. Borgarino, L. Lazzarini, F. Fantini, Micron, **31** (2000) 269.

8. Osamu Ueda, Microelectron Reliab, **39**, 1839 (1999).

9. L.B. Freund, International Journal of Solids and Structures, **37**, 185 (2000).

10. Mahajan, S., Prog. Mater. Sci., **33**, 1(1989).

11. E.A. Fitzgerald, P.D. Kirchner, R. Proano, G.D. Pettit, J.M. Woodall, D.G. Ast, Appl. Phys. Lett., **52**, 1496 (1988).

12. H. Steinhardt, P. Haasen, Phys. Status Solidi A, **49**, 93 (1978).

13. E.A. Fitzgerald, M.T. Currie, S.B. Samavedam, T.A. Langdo, G. Taraschi, V. Yang, C.W. Leitz, M.T. Bulsara, Phys. Status Solidi A., **171**, 227 (1999).

14. Brantley, W. A. and Harrison, D. A., in Proc. IEEE Reliability Physics, Symposium, 1973, p. 267.

15. Beam III, E. A., Temkin, H. and Mahajan, S., Semicond. Sci. Technol., **7**, A229 (1992).

16. S. Christiansen, M. Albrecht, W. Dorsch, H.P. Strunk, C. Zanotti-Fregonara, G. Salviati, A. Pelzmann, M. Mayer, M. Kamp, K.J. Ebeling, MRS Internet J. Nitride Semicond. Res., **1**(article 19) (1996).

17. W.M. Chen, P.J. McNally, Yu.V. Shvyd'ko, T. Tuomi, M. Lerche, A.N. Danilewsky, J. Kanatharana, D. Lowney, M. O'Hare, L. Knuuttila, J. Riikonen, R. Rantamäki, Phys. Status Solidi A, **186,** 365 (2001).

18. S. Mil'shtein, Phys. Status Solidi A, **171**, 371 (1999).

19. G. Dilliway, PhD Thesis, University of Southampton, 2002.

20. W.C. Dash, J. Appl. Phys., **29**, 705 (1958).

21. W.C. Dash, J. Appl. Phys., **30**, 459 (1959).

22. S. Mahajan, K.S. Sree Harsha, Principles of Growth and Processing of Semiconductors, McGraw-Hill, New York, 1999.

23. D. Brasen, W. A. Bonner, Mater. Sci. Engng, **61**, 167 (1983).

24. B. Cockayne, G.T. Brown, W.R. MacEwan, J. Cryst. Growth, **64**, 48 (1983).

25. R.S. Rai, S. Mahajan, D.J. Michel, H.H. Smith, S. McDevitt, C.J. Johnson, Mater. Sci. Engng, **B10**, 219 (1991).

26. Y. Seki, J. Matsui, H. Watanabe, J. Appl. Phys., **47**, 3374 (1976).

27. Y. Seki, H. Watanabe, J. Matsui, J. Appl. Phys., **49**, 822 (1978).

28. R.S. Rai, S. Guruswamy, K.T. Faber, J.P. Hirth, Phil. Mag. A, **60**, 1339 (1989).

29. W.M. Chen, P.J. McNally, K. Jacobs, T. Tuomi, A.N. Danilewsky, Z.R. Zytkiewicz, D. Lowney, J. Kanatharana, L. Knuuttila, J. Riikonen, J. Cryst. Growth, **243**, 94 (2002).

30. W.M. Chen, P.J. McNally, K. Jacobs, T. Tuomi, A.N. Danilewsky, D. Lowney, J. Kanatharana, L. Knuuttila, J. Riikonen, Mat. Res. Soc. Symp. Proc., **693**, 141 (2002).

31. H. Marchand, X.H. Wu, J.P. Ibbetson, P.T. Fini, P. Kozodoy, S. Keller, J.S. Speck, S.P. DenBaars, U.K. Mishra, Appl. Phys. Lett. **73**, 747 (1998).

32. S. Nakamura, M. Senoh, S. Nagahama, N. Iwasa, T. Matushita, T. Mukai, MRS Internet J. Nitride Semicond. Res. 4S1, G1.1 (1999); http://nsr.mij.mrs.org/4s1/g1.1/.

33. T.S. Zheleva, W.M. Ashmawi, O.-H. Nam, R.F. Davis, Appl. Phys. Lett. **74**, 2492 (1999).

34. T.S. Zheleva, O.-H. Nam, W.M. Ashmawi, D. J. Griffin, R. F. Davis, J. Cryst. Growth, **222**, 706 (2001).

35. F. Gerhard, Science, **278**, 1902 (1997).

36. S. Nakamura, M. Senoh, S.-I. Nagahama, N. Iwasa, T. Yamada, T. Matsushita, H. Kiyoku, Y. Sugimoto, T. Kozaki, H. Umemoto, M. Sano, K. Chocho, Jpn. J. Appl. Phys. **36**, L1568 (1997).

37. M. Razeghi, P. Sandvik, P. Kung, D. Walker, K. Mi, X. Zhang, V. Kumar, J. Diaz, F. Shahedipour, Mater. Sci. & Eng. B, **74**, 107 (2000).

38. S.S. Xu, D. Feng, X-ray Diffraction Topography, Academy Press, Beijing, 1987.

39. H. Raidt, R. Kohler, F. Banhart, B. Jenichen, A. Gutjahr, M. Konuma, I. Silier, E. Bauser, J. Appl. Phys. 80 (1996) 4101.

40. F. A. Ponce, D. P. Bour, W. Götz, P.J. Wright, Appl. Phys. Lett., **68**, 57 (1996).

41. A. Pelzmann, M. Mayer, C. Kirchner, D. Sowada, T. Rotter, M. Kamp, K.J. Ebeling, S. Christiansen, M. Albrecht, H.P. Strunk, B. Hollander, S. Mantl, MRS Internet J. Nitride Semicond. Res., **1**(article 40), (1996).

42. P.J. McNally, T. Tuomi, D. Lowney, K. Jacobs, A.N. Danilewsky, R. Rantamäki, M. O'Hare, L. Considine, Phys. Status Solidi A, **185**, 373 (2001).

43. K.W. Mah, E. McGlynn, J. Castro, J.G. Lunney, J-P. Mosnier, D. O'Mahony, M.O. Henry, J. Cryst. Growth, **222**, 497 (2001).

44. C.P. Khattak, F. Schmid, J. Cryst. Growth, **225**, 572 (2001).

45. D. Hull, Introduction to dislocations (Pergamon press, 1965).

3 White beam synchrotron X-Ray topography experimental results

3.1 Sapphire crystal measurement results

3.1.1 Why are sapphire wafers studied in this research?

Sapphire is a strong, tough, hard, highly chemically stable, low-scatter material, combining multispectral range transparency, high thermal conductivity and high temperature capability. Sapphire also has good insulating and dielectric properties, and is resistant to solarization. It has become an important optical materials for scientific, industrial and military applications [1-4], such as high power laser windows, hypersonic missile domes, etc.

As an optical window material, sapphire is transparent in the range from 142 nm to longer than 5 μm; it is also transparent from 50 μm through to microwave wavelengths.

Since the pioneering work of Maruskas and Tietjen in 1969 [5], sapphire remains the most commonly used substrate material for the heteroepitaxial growth of Group III-nitrides which are extensively exploited as the wide bandgap materials for blue laser and light emitting diode technologies [6], etc. Due to its relatively high thermal and chemical stability at high growth temperatures, excellent structural and surface morphology, its availability in large quantities and size, and its relative low cost, sapphire will continue to be an important substrate material for many kinds of epitaxial application.

In the past few years, non-cubic crystals, such as Al_2O_3 and 6H-SiC, especially the former, have been studied as backscattering mirrors for X-ray and Mössbauer radiation instead of traditional silicon crystals [7-9]. Exact back reflection in silicon suffers from extremely low – tending to zero – reflectivity [8, 10]. This occurs in cubic crystals because the condition for exact Bragg backscattering is fulfilled simultaneously with the condition for multiple beam Bragg diffraction. Furthermore, silicon single crystals allow backscattering only in limited regions of the X-ray spectrum. Non-cubic crystals, such as Al_2O_3 are free from these drawbacks. They can provide a higher density of backscattering reflections with high reflectivity. In fact

sapphire allows backscattering for x-rays with practically any energy above 10 KeV [8]. However for this to be realized, thick and perfect sapphire crystals have to be used. The crystal quality affects greatly the mirror performance [7-9].

As a result of its rhombohedral structure, sapphire has anisotropic properties, such as birefringence. However in the (0001) orientation, the anisotropic properties are minimized as a consequence of the radial crystal symmetry along the c-axis [1, 11-13]. Therefore (0001) sapphire is important for lenses and optics shaped to maintain optical and mechanical symmetry. For the manufacture of high temperature semiconductor devices, (0001) sapphire is also the most commonly used substrate [6, 14-19]. When it is used as a substrate for the fabrication of light-emitting diodes, sapphire has the advantage of being transparent up to 8.8 eV [6]. As described earlier, its quality has important effects on the fabricated devices, because dislocations in the epilayer may originate from the substrate, which in turn will deteriorate the device performance and reliability [20-21].

Single crystal sapphire can be manufactured by several methods, for example, the Verneuili technique (flame fusion rowth), edge-defined film fed growth (EFG), the Czochralski method, the heat exchanger method (HEM), and the gradient solidification method (GSM) [22], which is also referred to as the temperature gradient technique (TGT). Because of the poor sapphire quality produced with the Verneuili technique as a result of fast growth rates, sapphire produced with this technique is not used for GaN epitaxy [22].

The Czochralski method is a process in which sapphire crystal is pulled from a Al_2O_3 melt. The seed crystal is contacted with the melt surface and withdrawn slowly. The crystallization occurs on the seed with its same crystal orientation [23].

With the exception of HEM, other methods cannot produce large boules as the high temperature gradient in the boules during the cooling down stage will cause cracks [4, 24]. At present 34 cm diameter, 65 kg boules are grown on a production basis with the HEM technique. The production of high quality 500 mm diameter sapphire boules using this method has been attempted; the next step will be the production of 750 mm diameter sapphire boules with this technique [2-4, 25].

The HEM method was first called Schmid-Viechnicki or Gradident Furnace technique [4, 26]. It was developed at the Army Materials and Mechanics Research Centre in 1969 [25]. In this method, high purity Al_2O_3 material is put in the melt, a controllable, helium-cooled heat exchanger was used to extract heat during the

crystal growth [27]. The crystallization is initiated at the bottom centre of the crucible because of the cooling caused with the flow of helium. The sapphire crystal growth is conducted under vacuum to keep the high purity of the crystal, as higher vapour pressure impurities will volatilize under vacuum condition. Besides, most impurities have a low segregation coefficient in sapphire, and thus these impurities are rejected to the last material to solidify, which is near the outside surface of the boule; they are thus easily removed. In the final sapphire crystal product, most impurities are below the detectibility level («1 ppm w/w%) [1]. The name HEM has been in use since 1972 [28].

Despite the progress in sapphire growing techniques, it is still difficult to produce (0001) sapphire boules [1]. (0001) sapphire is actually produced by cutting perpendicular to the growth axis of $(1\bar{1}20)$ or $(10\bar{1}0)$ oriented crystals [1, 4].

In the past few years, advances in fabrication technology for sapphire components makes it possible to make large planar and spherical sapphire optics economically, with a combination of supersmooth surfaces and tight optical control. Thus sapphire will become a more widely used material in high technology applications.

In fact, sapphire has been extensively studied in theory and experiments in the past few decades [11-13, 29-32]. Among them there are a few papers related to dislocation studies using the X-ray transmission topography technique [29-32] and a laboratory X-ray source was typically used in these studies [29-32]. These included studies of Czochralski-grown sapphire [33], TGT sapphire [31], early stage HEM produced sapphire [29-30], etc.

In this study defects in sapphire wafers produced with the modified Czochralski method and the more recent HEM method [9, 34] were analysed with the synchrotron X-ray topography technique. The HEM sapphire samples were produced at Crystal System Inc.(CSI) [1-4, 25]. A premium grade "HEMEX" sapphire selected by optical methods was used, and several regions on each individual wafer were examined in order to study the dislocation distribution. Wafers cut from different boules were tested. The dislocation densities in a selection of wafers were calculated, the effects of the dislocation density on the X-ray reflectivity were studied, and the Burgers vectors for dislocations in the HEM sapphire were also carefully studied.

3.1.2 Quality assessment of sapphire wafers for X-Ray crystal optics

3.1.2.1 Dislocation distribution and density
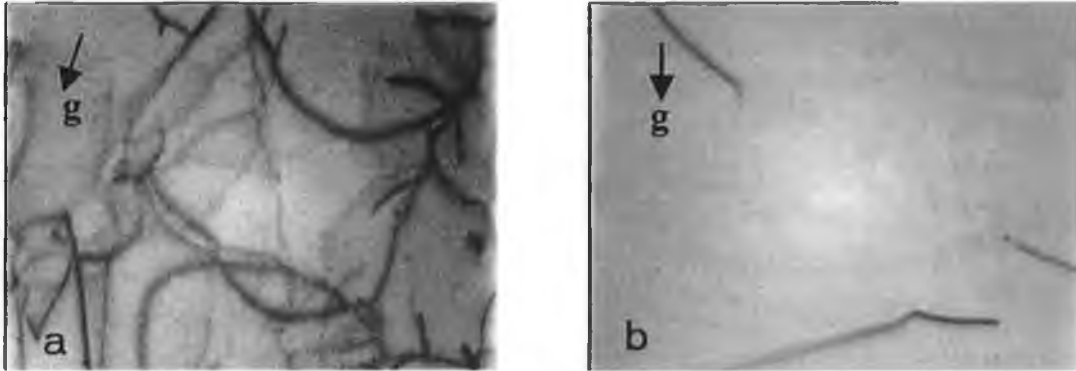
Figure 3.1 Large area back reflection topographs of HEMEX sapphire wafers cut from different boules show different dislocation densities: (a) ~10^3 cm^{-2}; 1 1 $\bar{2}$ 12 reflection, the thickness of the sample is about 1mm; (b) much lower dislocation density; 3 0 $\bar{3}$ 18 reflection, the thickness of the sample is about 2.5 mm. Sample area illuminated by X-rays is 2.1 mm x 1.7 mm.

LA-BRT topographs show that dislocations exist in most of the sapphire wafers. However in all samples discrete dislocation lines can be discerned, which indicates a relatively low dislocation density and high overall sapphire quality. The dislocation density in the studied sapphire can vary significantly from sample to sample, especially between samples produced with the different methods.

The nominally highest quality HEMEX sapphire typically shows a dislocation density in the range of ~10^3 cm^{-2} – see Fig. 3.1(a). In samples cut from a different boule a much lower dislocation density was detected – see Fig. 3.1(b). In some

Figure 3.2 0 $\bar{1}$ 1 1 transmission section topograph at a region in HEMEX sapphire with no dislocations (Note: the black spots in the image are due to defects in the film)
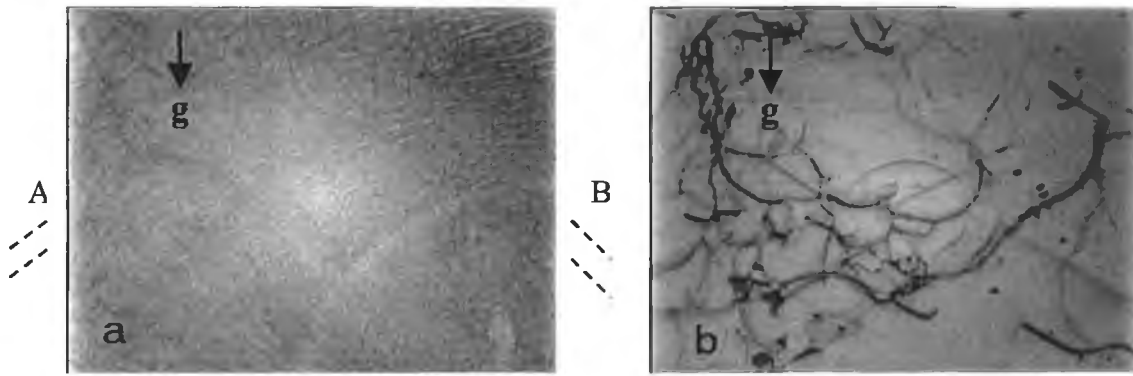
Figure 3.3 Large area back reflection topographs of a MCM sapphire wafer at regions with different dislocation densities: (a) Centre part of the wafer, 1 0 $\bar{1}$ 7 reflection; (b) Edge part of the wafer, 3 0 $\bar{3}$ 18 reflection . Sample area illuminated by X-rays is 2.1 mm x 1.7 mm; the thickness of the sample is about 0.3 mm.

regions of these samples no dislocations were detected at all. Pendellösung fringes were observed in the corresponding transmission Section Topographs (ST) (Fig. 3.2), which confirms the very high quality of the sapphire wafer [35]. The topograph of Fig. 3.3(a) was taken from the centre part of a MCM wafer. The dislocation density is high: $9.0 \times 10^4 \mathrm{cm}^{-2}$. It can be observed from Fig. 3.3(a) that two sets of dislocations exist in this wafer, which run roughly in the direction of [0 1 $\bar{1}$ 0] and [1 $\bar{1}$ 0 0] respectively, as indicated by directions A and B in the figure. An examination of the edge region of the same wafer indicates a higher crystal quality, as fewer dislocations $(4 \times 10^3 \mathrm{cm}^{-2})$ were detected in its corresponding topographs – see Fig. 3.3(b).

Dislocation densities were calculated using the equation [36]:

$$\rho = L/V \qquad\qquad (3.1)$$

where V is the volume of the sapphire wafer exposed to the x-rays during the experiment and L is the total dislocation line length in that volume and ρ is the density. V is calculated using the x-ray penetration depth t_p [37] and the beam size.

3.1.2.2 Correlation of Bragg reflectivity and dislocation density

Figure 3.4 shows the energy dependence of the reflectivity of the sapphire crystals for X-rays at normal incidence to the (0 0 0 30) atomic planes. The X-rays were monochromatized to an energy band of 7 meV width and scanned around E_0
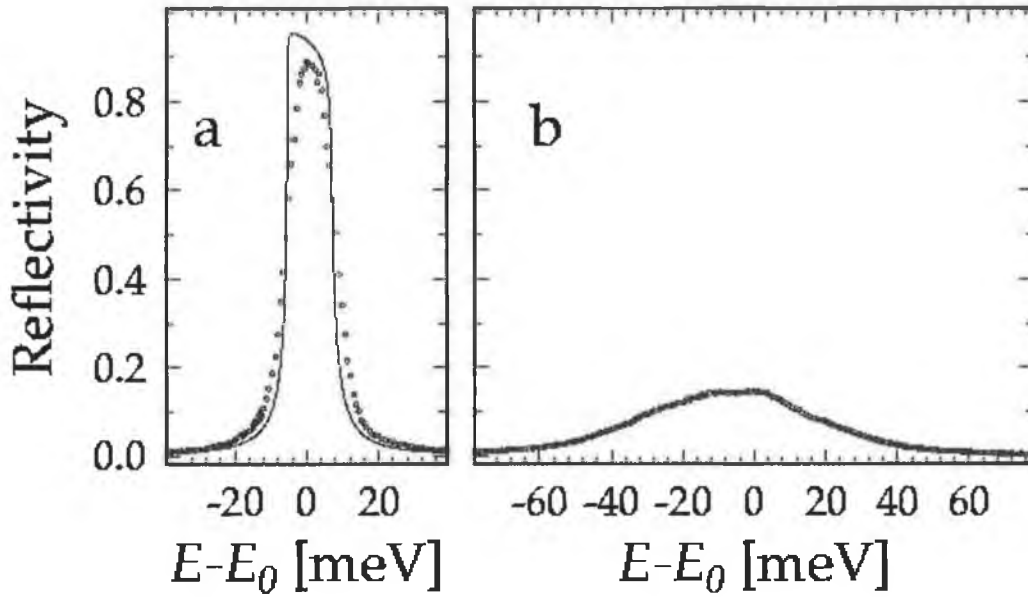
Figure 3.4 Energy dependence of the reflectivity of the sapphire crystals for X-rays at normal incidence to the (0 0 0 30) atomic planes. X-rays were scanned around $E_0 \approx$ 14.314 keV. (a) HEMEX low dislocation density sapphire; its corresponding topograph is shown in Fig. 1b. Circle curve is the measured result, and solid line is the calculated value with the dynamical theory of X-ray diffraction in perfect crystals. (b) MCM sapphire with high dislocation density; its corresponding topograph is shown in Fig. 3.3a.

$\approx$14.314 keV by using a high-energy resolution monochromator as described in detail in Ref [8]. The reflectivity curve shown in Fig. 3.4(a) was measured for the same region of the HEMEX Al_2O_3 crystal where few dislocations were detected – as seen in Fig. 3.1(b). The reflectivity curve shown in Fig. 3.4(b) was measured for the same region of the MCM Al_2O_3 crystal where the high dislocation density was detected – see Fig. 3.3(a). The HEMEX sapphire shows a high peak reflectivity of $\approx$ 86% and a narrow reflection curve – circles in Fig. 3.4(a) – with a full width at half maximum (FWHM) of 13 meV which fits well to the curve (solid line) calculated with the dynamical theory of X-ray diffraction in perfect crystals [8]. The MCM sapphire shows a much lower peak reflectivity of $\approx$ 14% and a broad reflection curve with a peak FWHM of $\approx$ 50 meV.

A comparison of the reflectivity and topography results shows that the white beam X-ray topography technique provides information on defect and dislocation distributions that correlates well with the reflectivity measurements.

3.1.2.3 Stacking fault observation

(a): 3 3 $\bar{6}$ 30 Reflection
Note: Scratches in the image are due to defects in the film

(b): 1 1 $\bar{2}$ 12 Reflection
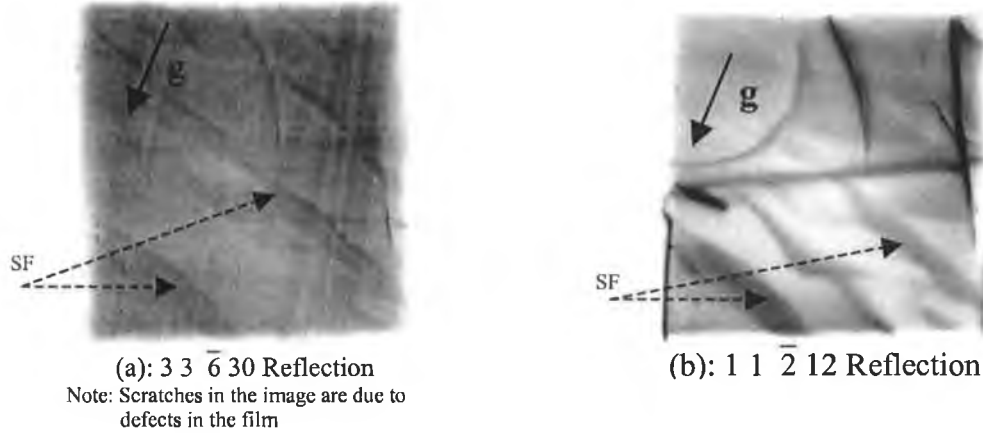
Figure 3.5 Stacking fault features for different reflections in the sapphire wafer; the thickness of the sample is about 50 μm.

One prominent feature observed in the sapphire samples is the occurrence of numerous stacking faults (SF). Stacking faults are found in most topographs and in all wafers inspected in this study. Some topographs of the SFs are shown in Fig.3.5(a)-(b), which comprise of two reflections from the same experimental spot. If the phase shift α ($\alpha = 2\pi\, g \bullet r$, where r refers to the fault vectors) between the normal crystal and the stacking faulted region is not an integer times 2π [35], the fault contrast in the topographs can be easily observed as shown in Fig. 3.5. In some samples, no dislocations were detected, but many stacking faults were still observed.

3.1.3 Dislocation analysis for Heat-Exchanger Method grown sapphire

3.1.3.1 Burgers vector analysis for dislocations in the HEM sapphire

As indicated in Section 3.1.2.1, topography measurement results show that dislocations exist in most of the HEM sapphire wafers. However the dislocation density in the studied sapphire can vary significantly from sample to sample [9].

The X-ray topographs indicate that the length for most dislocation lines is of the order of one millimetre. Considering the thickness of the sample and the experimental set-up for transmission topography [17], it is reasonable to conclude that most of the dislocations observed in this study are parallel or nearly parallel to the (0001) plane.

When examining dislocations in different reflections from the same region, one may notice that their contrast changes with each reflection. Occasionally the dislocation contrast disappears in certain reflections. By applying the criterion $g \bullet b$ =0, where g is the diffraction vector of the x-ray and b is the Burgers vector of the dislocation, one can in principle determine the Burgers vector of individual dislocations [29-31, 35].

More than 100 topographs were obtained from 10 HEM sapphire crystals in this study. Fig. 3.6 shows a selection of X-ray topographs for a typical individual HEM sapphire sample for different reflections. A schematic diagram indicating certain directions within this sapphire sample is included in Fig. 3.6(b). It can be seen that most straight dislocation lines intersect with each other at angles of 30°, 60°, 90° or 120°; a few dislocations are parallel to each other. Dislocations indicated as a, β and c show strong contrast in the $2\ \bar{1}\ \bar{1}\ 0$ reflection (Fig. 3.6(a)) and disappear or show weak contrast in the $3\ 0\ \bar{3}\ 0$ reflection (Fig. 3.6(e)). They also disappear or show weak contrast in the $2\ 0\ \bar{2}\ \bar{1}$ and $\bar{1}\ 0\ 1\ 2$ reflections. Thus the Burgers vector for dislocations of type a, β and c is parallel to the $[\ \bar{1}\ 2\ \bar{1}\ 0]$ direction. As the dislocation line of a is parallel to its Burgers vector, this dislocation is a pure screw dislocation. The dislocation line of β is parallel to $[1\ 0\ \bar{1}\ 0]$ and perpendicular to its Burgers vector, so dislocation β is a pure edge dislocation. But for dislocation c, the situation is quite different. The Burgers vector and dislocation line have a 60° angle with respect to each other. It is therefore most likely a 60° mixed dislocation. This is confirmed by the fact that dislocation c does not disappear completely but shows low contrast in the $2\ 0\ \bar{2}\ \bar{1}$ and $\bar{1}\ 0\ 1\ 2$ reflections (Fig. 3.6(h)) and (Fig. 3.6(i)).

Dislocations d~g disappear or show low contrast in the $3\ \bar{3}\ 0\ 0$ and $4\ \bar{4}\ 0\ 2$ reflections, and their Burgers vector is calculated to be parallel to the $[\ \bar{1}\ \bar{1}\ 2\ 0]$ direction. They are all mixed dislocations.

Similarly dislocation h disappears in the $1\ 1\ \bar{2}\ 0$ and $1\ 2\ \bar{3}\ \bar{1}$ reflections, and its Burgers vector is along $[1\ \bar{1}\ 0\ \bar{1}]$, and it is also a mixed dislocation.

(a) 2 $\bar{1}$ $\bar{1}$ 0 topograph
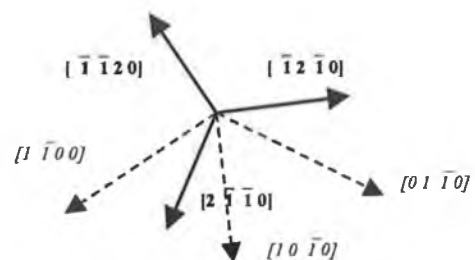
(b) Orientation of dislocations in the sapphire crystal

(c) 1 1 $\bar{2}$ 0 topograph

(d) 0 3 $\bar{3}$ 0 topograph

Note: scale bar for topographs 3.6(c)~3.6(j)
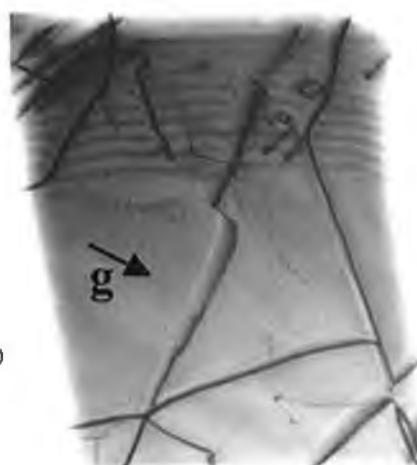
(e) 3 0 $\bar{3}$ 0 topograph

(f) 3 $\bar{3}$ 0 0 topograph
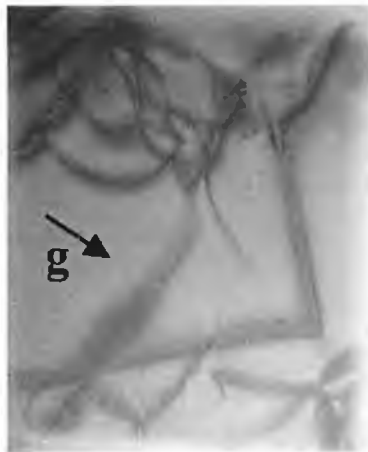
(g) 1 2 $\bar{3}$ $\bar{1}$ topograph

(h) 2 0 $\bar{2}$ $\bar{1}$ topograph

(i) $\bar{1}$ 0 1 2 topograph

(j) 4 $\bar{4}$ 0 2 topograph

Figure 3.6 Topographs of the same sapphire crystal with different reflections

Dislocation *i* disappears in the $2\,\bar{1}\,\bar{1}\,0$ reflection (see Fig. 3.6(c)), which indicates that the Burgers vector is parallel to $[0\,1\,\bar{1}\,L]$, where L is a constant, and it is a pure edge type dislocation.

Dislocations No. *1~7* show strong contrast in the $2\,\bar{1}\,\bar{1}\,0$ reflection, but disappear or almost disappear in the $0\,3\,\bar{3}\,0$ reflection. Thus the Burgers vector of these dislocations should be parallel to the $[2\,\bar{1}\,\bar{1}\,L]$ direction. The most common value for L is 0, which is confirmed by the following arguments. Dislocations *6(b₆=[2 $\bar{1}$ $\bar{1}$ L]), d(b_d=[$\bar{1}$ $\bar{1}$ 2 0]) and c(b_c=[$\bar{1}$ 2 $\bar{1}$ 0])* intersect at node *M*(see Fig.3.6(a)). Since $b_c+b_d+b_6=0$ [29], it then can be concluded that the Burgers vector for dislocation *6* is parallel to the direction of *[2 $\bar{1}$ $\bar{1}$ 0]*, i.e. L equal to zero. Dislocation *1* is a screw type dislocation. Dislocations *2~4* are mixed dislocations. Dislocations *5* and *6* are of a curved shape; they change from mixed type dislocations on the left part (Fig. 3.6(a)) to pure screw type dislocations on the right part of the dislocation line; near the middle, they are edge type dislocations. Dislocation *7* is also curved; it changes from a mixed dislocation in its upper part to a possible pure edge type dislocation in the lower part (Fig. 3.6(a)). Usually, curved dislocations in these crystals are caused by a fast growth rate, as the fast growth rate leads to an instability of the interface between the growing crystal and the melt [38]. The supersaturation of vacancy related dislocation climb motion during crystal growth [38] or a dislocation climb and reaction mechanism [30] also tends to cause the formation of curved dislocations.

The straight dislocations are usually formed in crystals with a slow growth rate [38]. Since the HEM sapphire crystals are grown for long periods, typically 25 days for the total cycle [3], many dislocations detected in the HEM sapphire tend to be straight lines. The curved dislocations detected in the HEM sapphire could be caused by mechanisms other than a fast growth rate. In fact, the curved dislocation lines in the topographs are usually connected with a dislocation reaction node, such as *M*. Each reaction represents a self-pinning point, thus the dislocations involved cannot glide easily [39], and dislocation climb will result in a curved dislocation line. But such a climb mechanism requires a transfer of materials and a high activation energy [39]. This can only be activated at high temperature, so the curved dislocations in the observed topographs are most probably formed during the cooling stage in the HEM

Table 3.1 List of reflections in which dislocations show strong contrast or disappear

Dislocation Symbol	1~7	a,β,c	d~g	h	i
Diffraction vector shows strong dislocation contrast (g)	2 $\bar{1}$ $\bar{1}$ 0	2 $\bar{1}$ $\bar{1}$ 0	2 $\bar{1}$ $\bar{1}$ 0	2 $\bar{1}$ $\bar{1}$ 0	0 3 $\bar{3}$ 0
Diffraction vector show no or almost no contrast (g)	0 $\bar{3}$ 3 0	3 0 $\bar{3}$ 0 2 0 $\bar{2}$ $\bar{1}$ $\bar{1}$ 0 1 2	3 $\bar{3}$ 0 0 4 $\bar{4}$ 0 2	1 1 $\bar{2}$ 0 1 2 $\bar{3}$ $\bar{1}$	2 $\bar{1}$ $\bar{1}$ 0
Direction of the Burgers vector for dislocations (b)	6:[2 $\bar{1}$ $\bar{1}$ 0] 1~5,7: [2 $\bar{1}$ $\bar{1}$ L]	[$\bar{1}$ 2 $\bar{1}$ 0]	[$\bar{1}$ $\bar{1}$ 2 0]	[1 $\bar{1}$ 0 $\bar{1}$]	[0 1 $\bar{1}$ L]
Dislocation type	1: screw 2~4:mixed	a: screw β: edge c: mixed	mixed	mixed	Edge

sapphire manufacturing process. To produce higher quality, dislocation free sapphire crystal, the cooling process should be controlled tightly during manufacturing.

A summary of the dislocation types is listed in Table 3.1, which indicates the reflections from which the dislocations exhibit strong, low or null contrast as well as other properties. At first glance dislocations *e, j* and *k* seem to be connected together, and should have the same Burgers vector and a similar contrast appearance. In fact, they are different dislocation lines, which are not easily detectable in most of the reflections, especially for dislocations *j* and *k*. But a careful inspection of the 1 1 $\bar{2}$ 0 and 1 2 $\bar{3}$ $\bar{1}$ reflections will enable the reader to arrive at this conclusion. A similar phenomenon was reported in [29].

3.1.3.2 Comments on the Burgers vector calculation using $g \bullet b = 0$

Traditionally four indices, i.e. *hkil*, are used to indicate the lattice planes of Trigonal Structural sapphire crystal [11, 40], but only three indices *h, k* and *l* are independent, the fourth index *i* is dependent on *h* and *k* through the following relation: $i=-(h+k)$ [40]. For the calculation of Burgers vectors with the condition $g \bullet b$

=0, either the three or four index system can be adopted. i.e. $h.U+k.V+i.T+l.W=0$ for the four index system or $h'.U'+k'.V'+l'.W'=0$ for the three index system, where $hkil$ and $h'k'l'$ are indices of reflection for the crystal planes, i.e. diffraction vector (g) indices, in the four and three index systems respectively. $[UVTW]$ and $[U'V'W']$ are the direction indices of the Burgers vector for dislocations in the four and three index systems, respectively. Similarly $T=-(U+V)$ [40]. Though $h=h'$; $k=k'$ and $l=l'$ in the above notation, the conversion of the Burgers vector indices between the three and four index system is not so simple. The relation between $[UVTW]$ and $[U'V'W']$ is listed as follows [40]:

$$U=(2U'-V')/3 \qquad\qquad (3.2)$$

$$V=(2V'-U')/3 \qquad\qquad (3.3)$$

$$T=-(U+V) \qquad\qquad (3.4)$$

$$W=W' \qquad\qquad (3.5)$$

$$U'=U-T \qquad\qquad (3.6)$$

$$V'=V-T \qquad\qquad (3.7)$$

$$W'=W \qquad\qquad (3.8)$$

So care should be taken in the calculation of Burgers vector for dislocations in sapphire and other trigonal or hexagonal crystals.

3.2 Epitaxial Lateral Overgrown GaN measurement results

3.2.1 Application of GaN based semiconductor devices

GaN is a wide-bandgap semiconductor, and α-GaN has a direct bandgap of 3.4 eV [6]. The physical properties of GaN make it an attractive semiconductor for many electronic and optoelectronic devices [22, 41-42]. Its wide and direct bandgap make it suitable for short wavelength emitters, LEDs (light-emitting diodes) and diode lasers, and detectors[43]. GaN based semiconductors [44] are extremely important for next generation opto-electronics by filling the voids in the opto-electronic spectrum from green to the ultra-violet. They have created new markets in green LED traffic signals, full colour outdoor displays, and promised the next great advance in white solid-state lighting. Their possible electronic applications are in the area of sources and amplifiers for communications and low loss switches in power conditioning. GaN based semiconductors are also promising as the light source for high-density optical storage systems. In 1999, a capacity of 22 GB was achieved using a GaN-based blue laser diode [42, 45]. The strong chemical bonds, wide bandgap and good thermal stability of GaN make it suitable for high temperature, high power electronics [22, 45] and high radiation exposure operation conditions [44]. The wide bandgap, high breakdown field (3×10^6 V cm^{-1}), high peak (3×10^7 cm s^{-1}) and saturation velocity (1.5×10^7 cm s^{-1}) of GaN enable the excellent microwave power performance of GaN based heterojunction field effect transistors [44, 46].

3.2.2 Structure of GaN

The thermodynamically stable structure of GaN is the hexagonal wurtzite structure (α-phase). In addition it has a metastable zincblende structure (β-phase). The α-phase and β-phase only differ in the stacking sequence of nitrogen and gallium, and it is possible that both phases can co-exist in the same epilayer [47]. For the α-phase GaN, its lattice constants are: a_0=3.189 Å, c_0=5.185 Å [48].

3.2.3 Typical GaN crystal material growth

Growing bulk GaN crystal requires extreme high N_2 pressure and high temperature to promote crystallization from solutions of atomic N in liquid Ga. GaN crystal grown with this method shows strong growth anisotropy, thus platelet shape crystals will be obtained [49]. It is not easy to enhance the growth along the (0001) direction. Though progress has been made in bulk crystal growth [49], it is still difficult to grow large (>1 cm), high quality GaN crystals suitable for substrates [6], and consequently most of the GaN-based applications are exploited with heteroepitaxial thin films over foreign substrates.

The six most commonly employed substrates are sapphire, 6H-SiC, Si, GaAs, $LiGaO_2$ and AlN [22]. Among them, as indicated earlier, sapphire is the most commonly used substrate. GaN epilayers grown on a sapphire substrate are usually of higher quality than those grown on other substrates [22]. In order to grow GaN epilayers, the sapphire substrate surface should be treated to remove contaminants and remnant polishing damage and to produce a step and terrace surface structure. Then the substrate surface is nitridated to alter the wetting characteristics of the deposited layers. Thirdly, a thin buffer layer of either GaN or AlN, which is usually about 10-100 nm thick, is deposited and annealed to produce a surface ready for the final epitaxial growth.

By far, (0001) sapphire is the most commonly used substrate for the GaN epitaxial growth (referring to page 58). GaN epitaxy on (0001) sapphire results in (0001) plane orientated epitaxial film, but with a $30°$ rotation of the in-plane GaN crystal directions with respect to the same directions in the sapphire. This $30°$ misorientation between the (0001) nitride plane and the (0001) sapphire plane occurs to reduce the lattice constants mismatch to 13.9 % [6]. Otherwise the lattice constants mismatch between the (0001) planes of sapphire and GaN is more than 30%. As a result of the high lattice mismatch, standard epitaxial deposition of GaN on Al_2O_3 leads to very high threading dislocation densities in the GaN epilayer, usually in the range of $10^{10} cm^{-2}$ [6, 14, 50-54]. However candela class high brightness GaN based light emitting diodes are realized [42, 55] on this kind of epilayer.

Although III-N based quantum structures containing InGaN are more tolerant of crystal lattice defects than the structures based on GaAs compounds, for high performance devices, it is still preferable to reduce defects in the epilayers [42, 45,

49]. There are a few methods to achieve high quality GaN based materials, such as growing large high quality bulk GaN crystal or using a low temperature buffer [56] as mentioned previously [49, 57], or using the epitaxial lateral overgrowth technique [17-18, 58-61].

As pointed out previously, it is difficult to grow large, high quality GaN single crystals. Epilayers grown only on lower temperature buffers (standard method) still possess high threading dislocation densities (10^{10}cm^{-2}). Besides, the surface of the GaN epilayer grown with the standard method is also rough (its roughness is more than 10 nm), which would cause mirror losses of at least 2-3% for laser diodes [42].

3.2.4 Epitaxial Lateral Overgrowth of GaN epilayer

Epitaxial lateral overgrowth (ELO) was first developed by Nishinaga *et al.* in 1988 [62] to improve GaAs epilayer quality, and was introduced to GaN-based semiconductors in 1997 [63-64].

In the ELO GaN process, a mask film is first deposited over the GaN seed layer, then parallel windows are opened along a specific direction in the mask. GaN starts to grow vertically at the window position in the later process, after which the GaN grows laterally along the mask surface (wing region). The adjacent GaN wings will coalesce to form a continuous film if enough growth time is given. As the crystal growth direction changes in the wing regions using the ELO technique, most of the dislocations threading from the underlying GaN seed to the window regions will not cross the upper surface of the wing areas [60-61, 65-68]. Thus GaN epilayer quality over the wing regions improves remarkably. Some reports show that even defect free wing regions can be obtained occasionally [60, 69-71] in the ELO epilayer. Overall the ELO technique can result in dislocation densities three or four orders of magnitude lower than in the planar GaN heterostructures [50, 52, 60, 68], and the roughness for the surface of the wing region is less than 1 nm also [42]. GaN-based devices have benefited from this reduced dislocation density [43, 52, 72-75]. The lifetime of laser diodes made on ELO GaN are more than 1000 hours at 30 mW continuous wavelength operation at 60°C and more than 10,000 hours at an output power of 2 mW [42, 76]. However ELO GaN is far from perfect at present, e.g. an unwanted $\approx 10^{6}$-10^{7}cm^{-2} dislocation density still exists in the epilayer [42, 50-52]. Moreover, interaction of the wings with the mask underneath is commonly observed
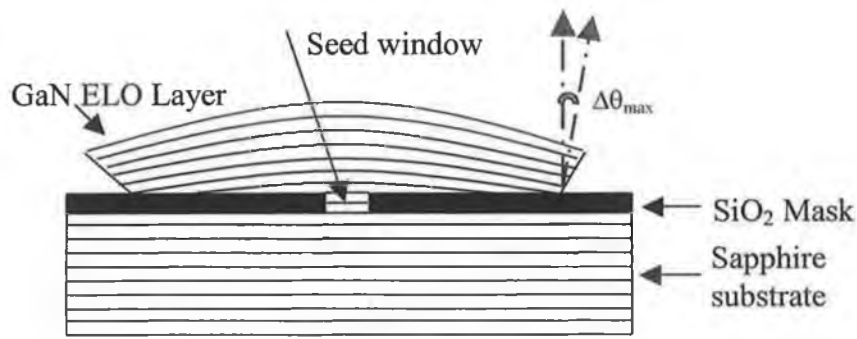
Figure 3.7 Schematic cross section of the GaN ELO sample. At the edge of the ELO GaN (i.e. the coalescence region between the neighbouring ELO GaN wings), the wing tilt reaches the largest value $\Delta\theta_{max}$. – not drawn to scale

in ELO structures. This phenomenon leads to a downward tilt of the ELO wings and to the creation of low angle boundaries over the mask edges as well as causing problems for defect-free coalescence of tilted wings grown from adjacent seeds [77]. A schematic for the ELO GaN technique and the tilted GaN wing is shown in Fig. 3.7; for clarity, only one window in the mask is shown in this schematic, but actually a lot of parallel windows are opened in the sample for the GaN epilayer lateral growth and the neighbouring wings coalesce to form a continuous ELO GaN epilayer for the samples measured in this study.

Therefore, many researchers are trying to optimize the ELO process by changing the process parameters [15, 78-80] and by studying other mask materials instead of the commonly used dielectrics [65, 81-82]. An understanding of the processes active during the ELO procedure, and their impact on defect generation, will help promote ELO GaN quality improvements. This will require a better understanding of MOVPE ELO growth mechanisms and advanced diagnostic tools to study the properties of the structures produced.

In this work white beam SXRT [9, 17-18, 34, 83] has been applied to measure the crystal misorientation in GaN on sapphire ELO structures. The data obtained is then compared with that from standard X-ray diffraction (XRD) studies of the same sample. X-ray diffraction measurements were performed using a Bede Model 150 double crystal diffractometer, by measuring the rocking curve about the GaN (0004) peak. Furthermore the stress distribution of the ELO GaN epilayer was studied with micro-Raman spectroscopy, which will be presented in chapter 5.

3.2.5 ELO GaN sample preparation

Table 3.2 Fill Factor at Different Regions on the Sample

Region	a	b	c	d
SiO$_2$ stripe width: S (µm)	/	3	3	3
Window size: W (µm)	/	3	4	5
Fill Factor	non-ELO	0.5	0.571	0.625

The growth of the GaN films was carried out in a vertical rotating disk MOVPE reactor manufactured by Thomas Swan & Co. operated at a pressure of 100 Torr. Initially, a low temperature thin (50 nm) GaN buffer layer was grown on the 430 µm thick (0 0 0 1) sapphire substrate at 550 °C [84]. On top of this, a 1.1 µm thick GaN buffer was deposited at 1050 °C. In both cases, trimethylgallium (TMG) and ammonia (NH$_3$) were used as the Ga and N precursors. Subsequently, a 150 nm thick SiO$_2$ mask was deposited using plasma enhanced chemical vapour deposition followed by conventional photolithography and dry etching. The width of the SiO$_2$ stripes in the sample was 3 µm, but the window sizes varied between 3 and 5 µm for different regions of the sample. As shown in Table 3.2, the wafer was divided into four regions according to their respective fill factors, i.e. ratio of stripe opening width to stripe period. In order to achieve large lateral growth rates the SiO$_2$ stripes were oriented in the <1 $\bar{1}$ 0 0> direction relative to the GaN epilayer.
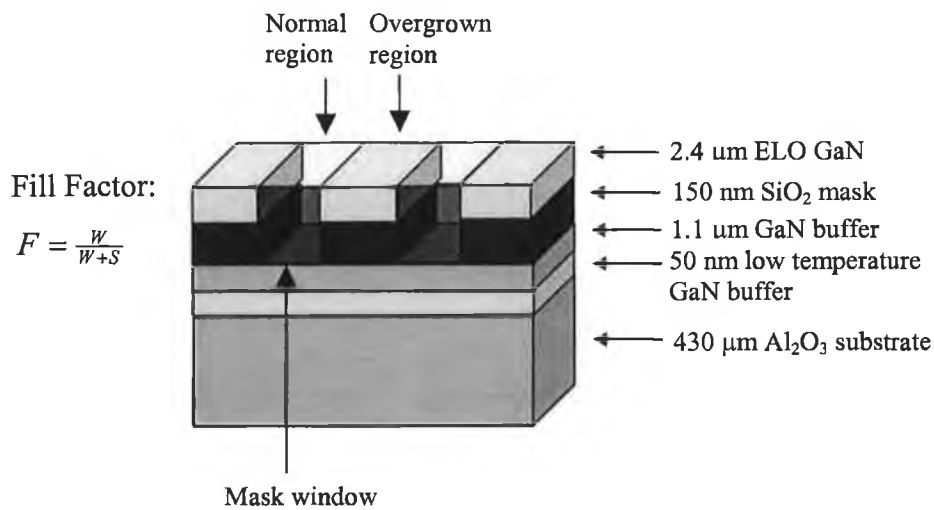
Figure 3.8 Schematic of ELO GaN over sapphire substrate– not drawn to scale

74

Prior to the actual ELO growth the sample was dipped for 5 s in a 1:4 solution of HF:H$_2$O to remove the surface oxide. Then, the ELO growth took place at a temperature of 1060 °C using H$_2$ as the carrier gas. Typical flow rates for the TMG and NH$_3$ were 23.7 μmol/min and 5 l/min respectively. The thickness of the resulting ELO layer as well as that of the reference planar layer of GaN (region a) was 2.4 μm, which was enough to get complete coalescence of neighbouring ELO stripes. The structure of the ELO GaN over sapphire substrate is shown in Fig.3.8.

3.2.6 Determination of crystal misorientation in Epitaxial Lateral Overgrowth of GaN

In this study White Beam Synchrotron X-ray Topography (WBSXT) is applied to the evaluation of regions *a - c* of the aforementioned ELO GaN and the sapphire substrate itself. The sample was tilted at an angle of 18° with respect to the perpendicular direction during transmission topography experiments. The GaN epilayer was on the film side as shown in Fig. 3.9. For the back reflection topography, the GaN epilayer was also on the film side. Two Laue patterns of topographs, i.e. one from the sapphire substrate and another from the GaN epilayer, appear on every recording film. Fig. 3.10 shows typical large area transmission topographs of the GaN on sapphire ELO structure; a few of these reflection indices
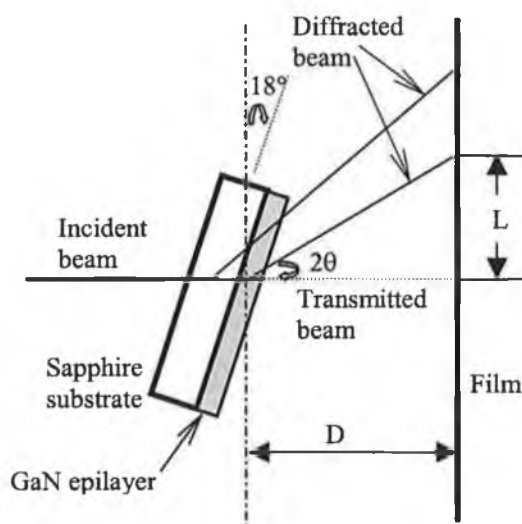
Figure 3.9 Schematic diagram of transmission X-ray topography– not drawn to scale
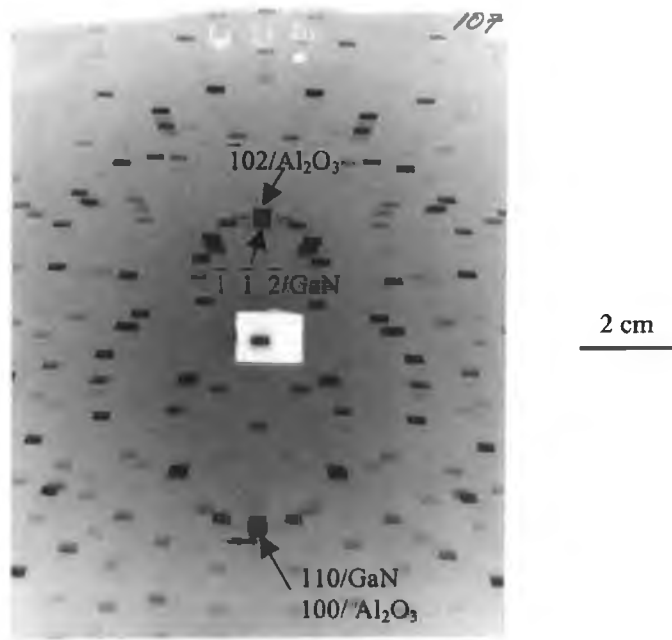
Figure 3.10 Laue patterns of large area transmission topographs of the GaN epilayer and of the sapphire (Al_2O_3) substrate

are indicated in Fig. 3.10.

All regions *a - d* of the sample were measured with the high resolution X-ray rocking curve for the GaN (0004) peak. The high resolution X-ray rocking curve method is a commonly used technique for measuring the crystal misorientation in ELO GaN epilayers [15].

Fig. 3.11 shows a series of $\bar{1}\ 0\ 1\ 2$ sapphire and $\bar{1}\ \bar{1}\ 2\ \bar{2}$ GaN transmission section topographs taken from different regions of the sample. Individual dislocations are not visible in the GaN topographic image, as their density is too high. This is also confirmed by large area transmission topographs (shown in Fig. 1.4) of the sample.

For the topographs shown in Fig. 3.11, the most interesting feature is the "fuzzy" feature that appears in the epitaxial GaN topographs [Figs. 3.11(b)-3.11(e)]. It is also found in the large area transmission topographs (Fig. 3.12) and topographs taken with the back reflection method (in both large area and section modes). Fig. 3.13 shows the $\bar{1}\ 1\ 0\ 5$ back reflection section topograph taken from region *b*, and the "fuzzy" feature is clearly seen in Fig. 3.13. This feature appears only in the
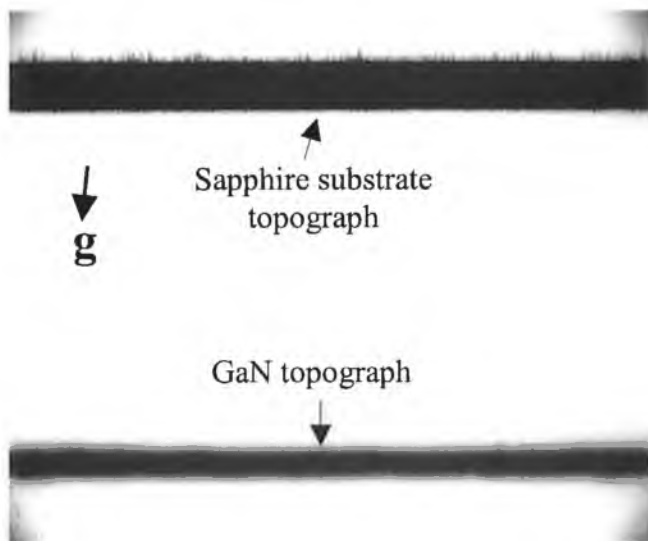
Sapphire substrate topograph

g

0.5mm

GaN topograph

(a) Section topograph taken from region *a* on non-ELO structure.

g
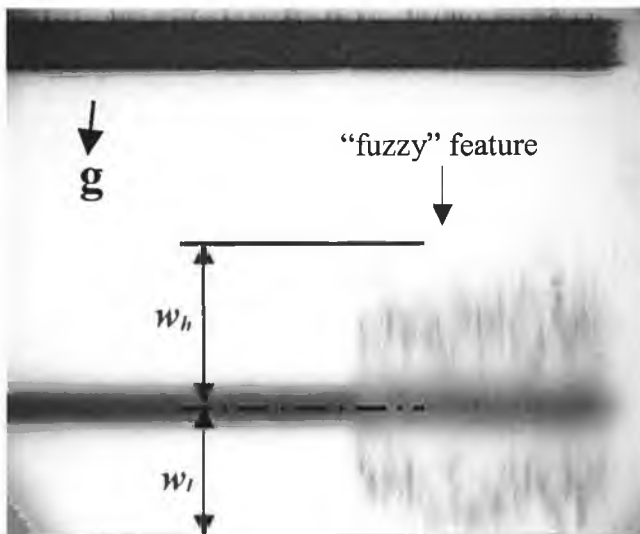
"fuzzy" feature

w_h

w_l

0.5mm

(b) Section topograph taken from boundary of regions *a* (non-ELO) and *b* (ELO region). Left: non-ELO; Right: ELO.

g

0.5mm

w_{epi}
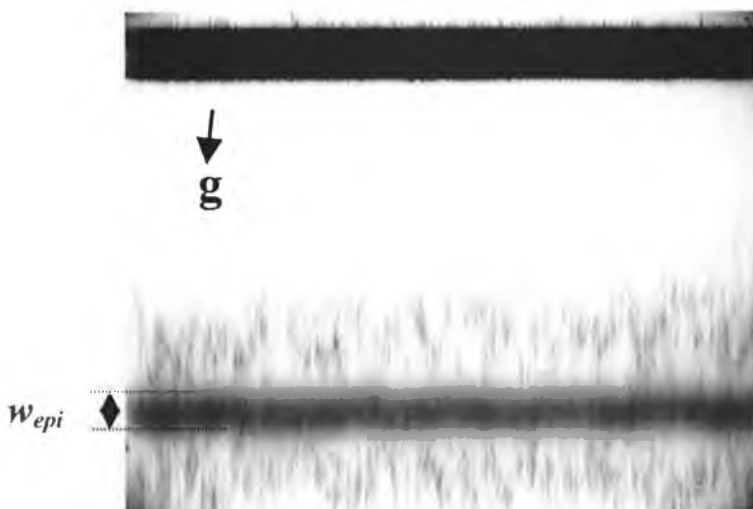
(c) Section topograph taken from ELO region *b*: 3 μm stripe/3 μm window.
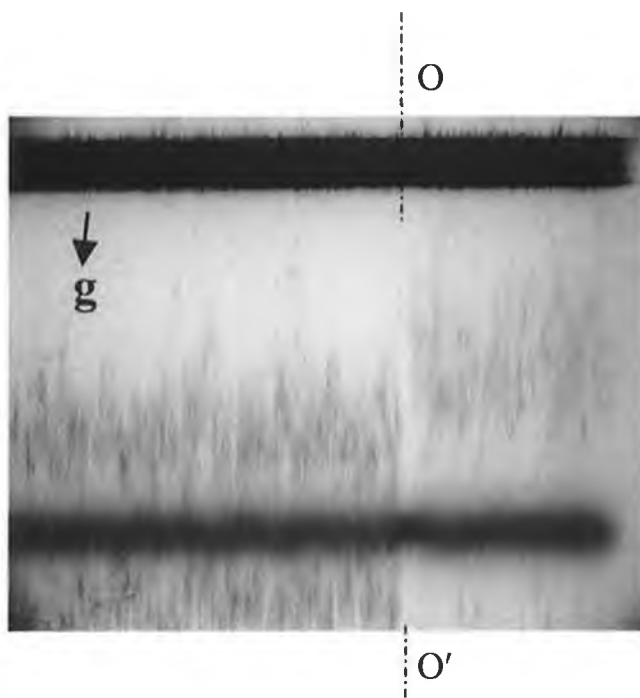
(d) Section topograph taken from the boundary of region *b* (ELO region) and *c* (ELO region). Left: 3 μm stripe/3 μm window; Right: 3 μm stripe/4 μm window. The OO′ dotted line represents the interface between the two different window sizes.
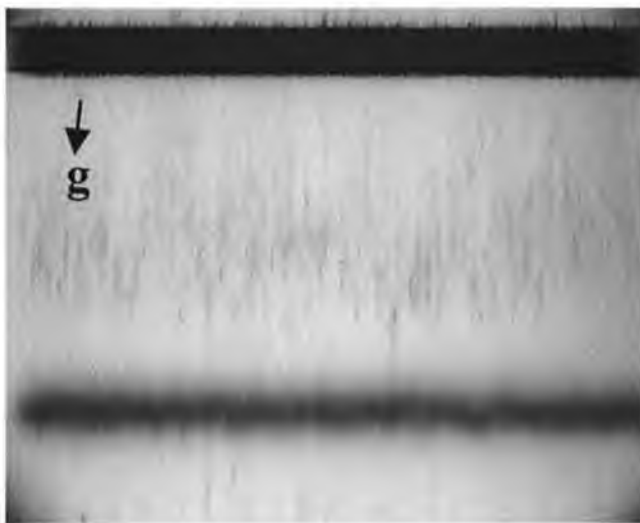
(e) Section topograph taken from ELO region *c*: 3 μm stripe/4 μm window.

Figure 3.11 Transmission section topographs ($\bar{1}$ 0 1 2 sapphire and $\bar{1}$ $\bar{1}$ 2 $\bar{2}$ GaN reflections) taken from different regions of the sample. The sapphire (Al_2O_3) topograph is located in the upper part and the GaN topograph is located in the lower part of all pictures.
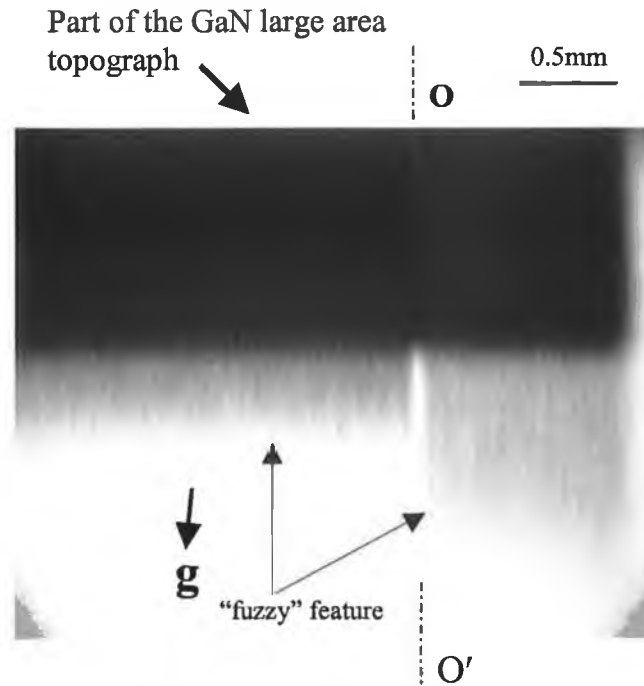
Figure 3.12 Part of the $\bar{1}\ \bar{1}\ 2\ \bar{2}$ GaN large area transmission topograph taken from the boundary of region *b* and *c* of the ELO sample. Left: region *b* (3 μm stripe and 3 μm window); Right: region *c* (3 μm stripe and 4 μm window). The OO′ dotted line represents the boundary between the two different window sizes. This large area topograph corresponds to the section topograph listed in Fig.3.11(d), but the sapphire ˙ substrate topograph is not included here.
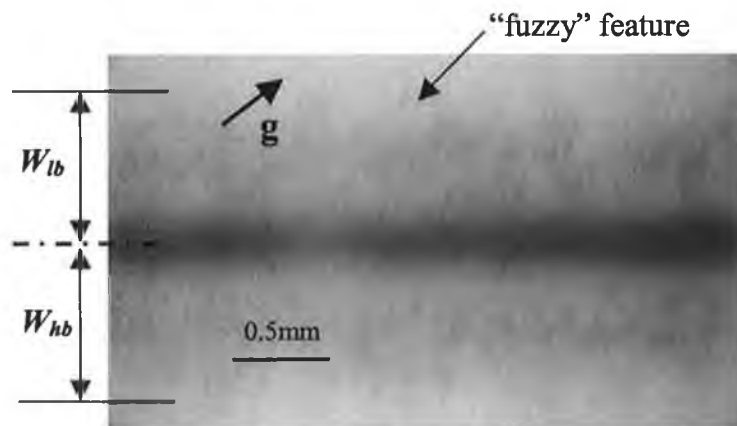
Figure 3.13 $\bar{1}\ 1\ 0\ 5$ back reflection section topograph taken from region *b*

topographs taken from the ELO regions, so it is absent in the topograph of region *a* of the sample (Fig. 3.11(a)). It is worth noting that the size of the "fuzzy" features increases when the ELO fill factor increases (see Fig. 3.11d and Fig. 3.12). The meaning of that is explained below.

Previous research has shown that the crystallographic orientation of the ELO epilayer tilts in the wing region relative to the window region [71, 82]. The nature of this tilting has not been fully explained yet, but the adhesion between the ELO stripe and the underlying mask caused by the surface energy and the van der Waals force [70, 85], capillary forces which are driven by an overall energy minimization in the stripe [15] or thinning/densification of the SiO_2 mask [50], are regarded as possible causes of the observed wing tilt. The way in which tilting of the ELO wings results in the appearance of the "fuzzy" features visible in the topographs can be explained as follows. When the crystal is immersed in a beam of X-rays, it diffracts the X-rays according to Bragg's Law:

$$2d_{hkl}\sin\theta=\lambda \tag{3.9}$$

where d_{hkl} is the interplanar spacing of the lattice planes, θ is the Bragg angle and λ is the wavelength of the diffracted beam. As shown in Fig. 3.9, in the transmission topography experiment, the distance (L) from the nominal centre of the transmitted beam to one Laue spot is calculated according to the following formula:

$$L=\text{Dtan}(2\theta) \tag{3.10}$$

where D is the distance from the film to the sample, its value having been confirmed using the X-ray diffraction simulator OrientExpress [86].

As the crystallographic orientation tilts in the laterally overgrown parts of ELO GaN, the corresponding lattice planes of the wings and the normal region (i.e. vertically grown part of ELO and the underlying GaN buffer) have different Bragg angles with respect to the incident beam. If θ is the Bragg angle of the window region, the Bragg angle in the wing region may be $\theta-\Delta\theta$ or $\theta+\Delta\theta$ according to which way the wing tilts. However Bragg's Law is still satisfied in the wing region as a white beam is used in this study. But the wavelength of the diffracted beam in this region is different from that in the window region as indicated in equation (3.11).

$$2d\sin(\theta\pm\Delta\theta)=\lambda' \tag{3.11}$$

As we have shown already, $\Delta\theta$ varies with the distance from the ELO stripe centre [87]. The topograph of the tilted wing will appear at the upper (for $\theta+\Delta\theta$ or

lower (for θ-$\Delta\theta$) position on the recording film with respect to the topographic image of the normal region. Therefore, the ELO GaN topograph will produce separate images of the normal region and of the wings, as observed in Figs. 3.11(b) – 3.11(e). The "fuzzy" streaks above and below the normal topograph are the images of the left and right wings, respectively. As the topograph in the ELO regions $b - d$ of the sample separates into different parts, the intensity corresponding to the normal GaN decreases compared to that of the planar GaN epilayer (see Fig. 3.11b).

The width of the "fuzzy" or misorientational features provides quantitative information about the wing tilt in the ELO grown GaN. Table 3.3 lists the measured largest widths of the topographic images of the wing regions of ELO GaN, w_h and w_l, in the $\bar{1}\ \bar{1}\ 0\ \bar{2}$ transmission section topographs and W_{hb} and W_{lb} in the $\bar{1}\ 1\ 0\ 5$ back

Table 3.3 Wing tilt measurement results

Region		b	c	d
Fill factor		0.5	0.571	0.625
Measured "fuzzy" width from $\bar{1}\ \bar{1}\ 2\ \bar{2}$ TS topograph (mm)	W_l	0.75	1.32	/
	W_h	0.80	1.42	/
Calculated wing tilt from $\bar{1}\ \bar{1}\ 2\ \bar{2}$ TS topograph (arcsec)	$\Delta\theta_l$	-1275	-2253	/
	$\Delta\theta_h$	+1343	+2371	/
Measured "fuzzy" misorientationed width from $\bar{1}105$ BRS topograph (mm)	W_{lb}	0.80	1.65	/
	W_{hb}	0.80	1.65	/
Calculated wing tilt from $\bar{1}105$ BRS topograph (arcsec)	$\Delta\theta_{lb}$	-1040	-2124	/
	$\Delta\theta_{hb}$	+1059	+2205	/
(0004) X-ray Rocking curve measured wing tilt (arcsec)	$\Delta\omega_l$	-731	-1174	1448
	$\Delta\omega_h$	+743	+1330	1602

TS=Transmission Section

BRS=Back Reflection Section

reflection section topograph (as defined schematically in Fig.3.11b and Fig.3.13), and the calculated wing tilts. $\Delta\theta_h$, $\Delta\theta_l$ are the wing tilt values calculated from the $\bar{1}\,\bar{1}\,0\,\bar{2}$ transmission section topograph measurements of the widths of W_h and W_l; $\Delta\theta_{hb}$, $\Delta\theta_{lb}$ are the wing tilt values calculated from the $\bar{1}\,1\,0\,5$ back reflection section topographic image widths of the tilted GaN wing regions W_{hb} and W_{lb}. $\Delta\theta_h$ or $\Delta\theta_{hb}$ is the increment of the Bragg angle in the left wing region relative to the window region caused by the wing tilt; $\Delta\theta_l$ or $\Delta\theta_{lb}$ is the decrement of the Bragg angle in the right wing region relative to the window region caused by the wing tilt.

The Bragg angle increment $\Delta\theta_h$ from the transmission section topograph or $\Delta\theta_{hb}$ from the back reflection section topograph is calculated by the following formulae:

$$D\tan 2(\theta + \Delta\theta_h) - D\tan(2\theta) = W_h \qquad (3.12)$$

$$D\tan(180 - 2\theta) - D\tan[180 - 2(\theta + \Delta\theta_{hb})] = W_{hb} \qquad (3.13)$$

The Bragg angle decrement is calculated with a similar method.

As can be seen from Table 3.3, the wing tilts increase with an increase of the fill factor. To explain this finding we recall the report by Marchand *et al.* [88], who showed that the GaN ELO stripes become wider and thinner when the fill factor increases. As tilting of the ELO wings is caused by their interaction with the underlying mask, the tilt angle increases with wing width and decreases with its thickness [15, 89]. Thus, a large fill factor enhances lateral overgrowth at the expense of vertical growth, which results in a large tilt of the wings, in agreement with the available literature and data [15]. The data in Table 3.3 also shows that the wings tilt asymmetrically. This may in part be due to difficulties in precisely controlling the off-orientation of the substrate with respect to the ELO stripe growth; this asymmetry could also possibly be related to the fact that during growth the stripes were orientated perpendicular to the rotation direction (i.e. radially in the reactor), which could lead to a difference in the supply of species and the extent of lateral overgrowth between both sides of the stripes. This in turn should result in a tilt asymmetry as the tilt angle is sensitive to wing dimensions. Similar behaviour has been reported by Fini *et al.* for samples grown by MOVPE [15].

The wing tilt tendency with the increase of the fill factor and the tilt asymmetry around the window are further confirmed with the X-ray diffraction measurements for the GaN (0 0 0 4) peak. The X-ray rocking curves measured with the scattering plane (defined by incident and reflected wave vectors) set perpendicular to the seeding lines are shown in Fig. 3.14. It can be seen from Fig. 3.14 that the ELO GaN (0 0 0 4) reflection splits into three peaks: the central one is due to reflection from the window region and the underlying seed GaN and the two side peaks are caused by reflections from the tilted wings. These X-ray diffraction curves show the same tilt asymmetry and wing tilt angle dependence on the fill factor. However, as shown in Table 3.3, they give smaller values of tilt angle compared to the X-ray topography method. In the SXRT technique the maximum widths, w_l, w_{lb} or w_h, w_{hb}, used in the wing tilt measurement (see equations (3.12), (3.13)), give the maximum wing tilt information. On the contrary, the two side peaks of the X-ray diffraction curve are diffuse, which is related to the fact that the wing tilts are distributed over a certain range. Thus, the X-ray beam, the size of which is usually much larger than the window spacing, samples many ELO stripes. Actually, this tilt distribution can be studied by X-ray topography as images of individual tilted wings can be resolved in the topographs (see Fig. 3.11(c)), while the X-ray diffraction technique gives the tilt information integrated over all stripes illuminated by the beam. The centre positions in the peaks of the diffraction curve are regarded as the nominal wing tilt values, so they give information on the average wing tilt only. Consequently, the X-ray
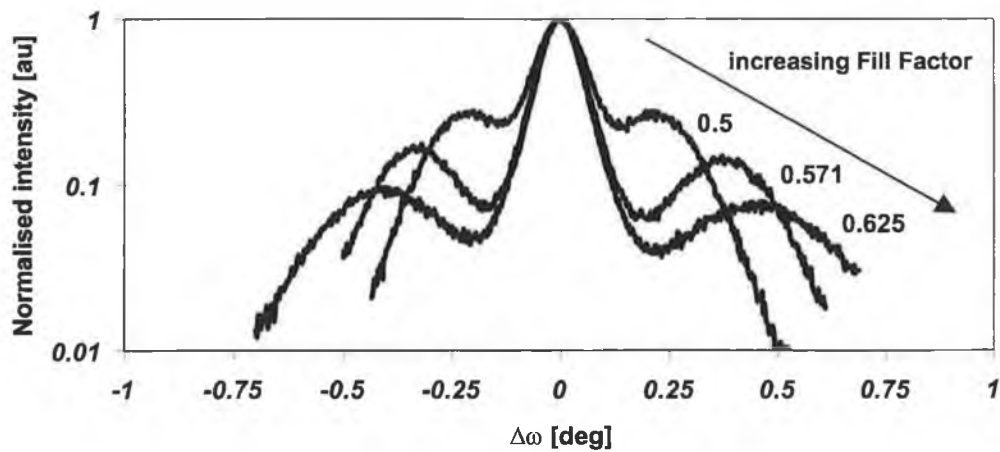
Figure 3.14 X-ray rocking curves mesured from different regions of the sample

diffraction method always yields smaller wing tilt values than those obtained by X-ray topography.

Table 3.3 also shows that the $\bar{1}\ \bar{1}\ 2\ \bar{2}$ transmission section topograph and the $\bar{1}\ 1\ 0\ 5$ back reflection section topographs exhibit different wing tilts. This is reasonable as each set of diffracting planes will exhibit a different level of distortion due to the anisotropic property of the GaN crystal and the non-uniform stress distribution in the GaN epilayer. Thus different wing tilt results are obtained by using different reflections. Because of the experimental set-up limitations, it is difficult to measure and compare the wing tilt values from the same reflection in the back reflection and transmission topography. However the wing tilt tendency measured from the back reflection and transmission topography is the same as the fill factor changes.

Furthermore, let us point out that the section topograph image of the vertically grown GaN and of the underlying buffer appears to be almost as thick as that of the sapphire substrate despite the fact that the GaN film is about 3.5 µm thick only, while the sapphire has a thickness of 430 µm. This effect is most likely due to the fact that the GaN buffer is far from perfect and this manifests itself via local deviations from lattice coherence. Various regions in the buffer, each slightly misoriented with respect to its neighbour, though macroscopically aligned, will each contribute to a topographic image in a manner similar to a mosaic structure with a high dislocation density. Each of these regions will produce images at slightly different locations on the film, which in turn will result in broadening of the whole GaN buffer image. The measured width of the $\bar{1}\ \bar{1}\ 2\ \bar{2}$ GaN transmission section topographs, w_{epi} (as defined in Fig. 3.11(c)), of region b is 0.2 mm, which gives the maximum GaN crystal lattice misorientation of ±170 arcsec if calculated with the same method as that for the wing tilt. This value is an order of magnitude less than that measured in the wing region, which shows that lattice misorientation caused by tilting of the ELO wings is of prime importance in GaN ELO structures.

3.2.7 Quality of the sapphire substrate used for the ELO GaN

Figure 3.15 is the $5\ \bar{4}\ \bar{1}\ 0$ large area transmission topograph of the sapphire substrate. It shows that the dislocations form networks in the sapphire substrate. It is
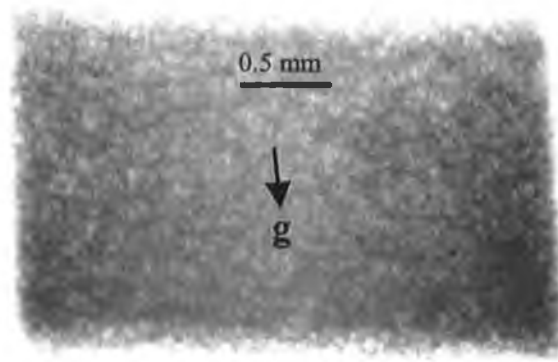
Figure 3.15 5 $\bar{4}$ $\bar{1}$ 0 transmission large area topography of sapphire substrate

not easy to discern individual dislocations in this topograph. The transmission section topograph of the sapphire substrate also shows a high dislocation density and the dislocations are distributed through the whole thickness of the substrate. After comparing Fig. 3.15 with the topograph in Fig. 3.3a [9], which is taken from a modified Czochralski produced sapphire wafer with a dislocation density of 9 x 10^4cm^{-2}, as well as considering the sapphire substrate thickness used for this ELO GaN and the X-ray penetration depth for topograph in Fig. 3.3a, the dislocation density in the substrates examined in this study is roughly estimated to be approximately ~10^6cm^{-2}. This implies a relatively low quality sapphire substrate.

References

1. F.K. Schmid, C.P. Khattak, D.M. Felt, Laser Focus World, **23**, 167 (1996).

2. F. Schmid, H.H. Rogers, C.P. Khattak, D.M. Felt, Proceedings of the SPIE - The International Society for Optical Engineering. **3424**, 37 (1998).

3. F. Schmid, C.P. Khattak, H.H. Rogers, D.M. Felt, J. Askinazi, R.V. Wientzen, Proceedings of the SPIE - The International Society for Optical Engineering. **3705**, 70 (1999).

4. C. P. Khattak, F. Schmid, J. Cryst. Growth, **225**, 572 (2001).

5. H.P. Maruskas, J.J. Tietjen, Appl. Phys. Lett. **15**, 327 (1969).

6. O. Ambacher, J. Physics D: Appl. Phys. **31**, 2653 (1998).

7. Yű. V. Shvyd'ko, E. Gerdaǔ, J. Jäschke, O. Leűpold, M. Lűcht and H. D. Rűter, Phys. Rev. B **57**, 4968 (1998).

8. Yu.V. Shvyd'ko and E. Gerdau, Hyperfine Interactions **123/124**, 741(1999).

9. W.M. Chen, P.J. McNally, Yu.V. Shvyd'ko, T. Tuomi, M. Lerche, A.N. Danilewsky, J. Kanatharana, D. Lowney, M. O'Hare, L. Knuuttila, J. Riikonen, R. Rantamäki, Phys. Status Solidi A, **186,** 365 (2001).

10. J.P. Sutter, PhD Thesis, Purdue University, 2000.

11. J. B. Bilde-Sorensen, B. F. Lawlor, T. Geipel, P. Pirouz, A. H. Heuer and K. P. D. Lagerlof, Acta Mater. **44**, 2145 (1996).

12. P. Pirouz, B. F. Lawlor, T. Geipel, J. B. Bilde-Sorensen, A. H. Heuer and K. P. D. Lagerlof, Acta Mater. **44**, 2153 (1996).

13. T. Geipel, J. B. Bilde-Sorensen, B. F. Lawlor, P. Pirouz, K. P. D. Largerlof and A. H. Heuer, Acta Mater. **44**, 2165 (1996).

14. J. Chaudhuri, M. H. Ng, D. D. Koleske, A. E. Wickenden and R. L. Henry, Mater. Sci. Eng. B, **64**, 99 (1999).

15. P. Fini, H. Marchand, J. P. Ibbetson, S. P. DenBaars, U. K. Mishra and J. S. Speck, J. Crystal Growth, **209**, 581 (2000).

16. X. J. Ning, F. R. Chien, P. Pirouz, J. W. Yang and M. Asif Khan, J. Mater. Res. **11**, 580 (1996).

17. W.M. Chen, P.J. McNally, K. Jacobs, T. Tuomi, A.N. Danilewsky, Z.R. Zytkiewicz, D. Lowney, J. Kanatharana, L. Knuuttila, J. Riikonen, J. Cryst. Growth, **243**, 94 (2002).

18. W.M. Chen, P.J. McNally, K. Jacobs, T. Tuomi, A.N. Danilewsky, D. Lowney, J. Kanatharana, L. Knuuttila, J. Riikonen, Mat. Res. Soc. Symp. Proc., **693**, 141 (2002).

19. W.M. Chen, G.D.M. Dilliway, P.J. McNally, T. Tuomi, A.F.W. Willoughby, J. Bonar, J. Mater. Sci. - Mater. Electron, **14**, 455 (2003).

20. O. Ueda, Microelectronics Reliability, **39**, 1839 (1999).

21. S. Mahajan, Acta Mater. **48**, 137 (2000).

22. L. Liu, J.H. Edgar, Mater. Sci. Eng. Rep. **R37**, 61 (2002).

23. M. Maruyama, Jpn. J. Appl. Phys., **5**, 1026 (1966).

24. M.R. Kokta, Growth of crystals for solid state lasers, in: P. Hammerling, A.B. Budgor, A. Pinto (Eds.), Tunable Solid State Lasers, Springer Series in Optical sciences No. 47, Springer, New York, 1985.

25. F. Schmid, C.P. Khattak and D.M. Felt, Am. Ceram. Soc. Bull. **73**, 39 (1994).

26. F. Schmid, D. Viechnicki, J. Am. Ceram. Soc. **53**, 528 (1970).

27. F. Schmid, D. Viechnicki, U.S. Patent No. 3,653,432, April 4, 1972.

28. F. Schmid, Solid State Technol., **16**, 45 (1972).

29. J. L. Caslavsky, C. P. Gazzara and R.M. Middleton, Phil. Mag. **25**, 35 (1972).

30. J. L. Caslavsky and C. P. Gazzara, Phil. Mag. **26**, 961 (1972).

31. Zhang Qiang, Deng Peizhen and Gan Fuxi, J. Appl. Phys. **67**, 6159 (1990).

32. Zhang Qiang, Deng Peizhen and Gan Fuxi, J. Crystal Growth, **108**, 377 (1991).

33. C.A. May, J.S. Shah, J. Materials Sci., **4**, 179 (1969).

34. W.M. Chen, P.J. McNally, Yu.V. Shvyd'ko, T. Tuomi, A.N. Danilewsky, M. Lerche, J. Cryst. Growth, **252**, 113 (2003).

35. D. K. Bowen, B. K. Tanner, High Resolution X-ray Diffractometry and Topography, Taylor and Francis, 1998.

36. Xu Shunshen and Feng Duan, X-ray Diffraction Topography, Science Press, Beijing, 1987.

37. R. Rantamäki, T. Tuomi, P. J. McNally, J. Curley and A. Danilewsky, J. X-Ray Sci. Technol. **8**, 159 (1998).

38. M. Tachibana, Qi Tang; N. Ide, K. Kojima, Jpn. J. Appl. Phys. Part 1. **33**, 1995 (1994).

39. J.L. Caslavsky, G.P. Gazzara, J. Mater. Sci. **6**, 1139 (1971).

40. C. Hammond, The Basics of Crystallography and Diffraction, Oxford University Press, 1997.

41. S.J. Pearton, F. Ren, A.P. Zhang, K.P. Lee, Mater. Sci. Eng. Rep. **R30**, 55 (2000).

42. T. Miyajima, T. Tojyo, T. Asano, K. Yanashima, S. Kijima, T. Hino, M. Takeya, S. Uchida, S. Somiya, K. Funato, T. Asatsuma, T. Kobayashi, M. Ikeda, J. Phys.: Condens. Matter., **13**, 7099 (2001), and reference therein.

43. E. Muñoz, E. Monroy, J.L. Pau, F. Calle, F. Omnes, P. Gibart, J. Phys.: Condens. Matter., **13**, 7115 (2001).

44. H. Xing, S. Keller, Y.-F. Wu, L. McCarthy, I.P. Smorchkova, D. Buttari, R. Coffie, D.S. Green, G. Parish, S. Heikman, L. Shen, N. Zhang, J.J. Xu, B.P. Keller, S.P. DenBaars, U.K. Mishra, J. Phys.: Condens. Matter. **13**, 7139 (2001).

45. T. Mukai, S. Nagahama, N. Iwasa, M. Senoh, T. Yamada, J. Phys.: Condens. Matter., **13**, 7089 (2001).

46. S.C. Binari, W. Kruppa, H.B. Dietrich, G. Kelner, A.E. Wickenden, J.A.J. Freitas, Solid-State Electron., **41**, 1549 (1997).

47. A. Tabata, R. Enderlein, J.R. Leite, S.W. da Silva, J.C. Galzerani, D. Schikora, M. Kloidt, K. Lischka, J. Appl. Phys. **79**, 4137 (1996).

48. J.H. Edgar (Ed), Group III Nitrides, London: INSPEC, 1994.

49. I. Grzegory, J. Phys.: Condens. Matter., **13**, 6875 (2001).

50. H. Marchand, X.H. Wu, J.P. Ibbetson, P.T. Fini, P. Kozodoy, S. Keller, J.S. Speck, S.P. DenBaars, U.K. Mishra, Appl. Phys. Lett. **73**, 747 (1998).

51. A. Sakai, H. Sunakawa, A. Usui, Appl. Phys. Lett. **71**, 2259 (1997).

52. S. Nakamura, M. Senoh, S. Nagahama, N. Iwasa, T. Matushita, T. Mukai, MRS Internet J. Nitride Semicond. Res. **4S1**, G1.1 (1999); http://nsr.mij.mrs.org/4s1/g1.1/.

53. S.D. Lester, F.A. Ponce, M.G. Craford, D.A. Steigerwald, Appl. Phys. Lett. **66**, 1249 (1995)

54. T.S. Zheleva, W.M. Ashmawi, K.A. Jones, Phys. Stat. Sol. (a) **176**, 545 (1999).

55. S. Nakamura, T. Mukai, M. Senoh, Appl. Phys. Lett., **64**, 1687 (1994).

56. S. Nakamura, Jpn. J. Appl. Phys., **30**, 1705 (1991).

57. T. Inoue, Y. Seki, O. Oda, S. Kurai, Y. Yamada, T, Taguchi, Jpn, J. Appl. Phys., **39**, 2394 (2000).

58. W.M. Chen, P.J. McNally, K. Jacobs, T. Tuomi, J. Kanatharana, D. Lowney, L. Knuuttila, J. Riikonen, J. Toivonen, J. Mater. Sci. - Mater. Electron, **14**, 283 (2003).

59. Z.R. Zytkiewicz, Thin Solid Films, **412**, 64 (2002).

60. T. S. Zheleva, O.H. Nam, W. M. Ashmawi, J.D. Griffin, R.F. Davis, J. Cryst. Growth, **222**, 706 (2001).

61. K. Hiramatasu, J. Phys.: Condens. Matter., **13**, 6961 (2001).

62. T. Nishinaga, T. Nakano, S. Zhang, Jpn. J. Appl. Phys., **27**, L964 (1988).

63. A. Usui, H. Sunakawa, A. Sakai, A. Yamaguchi, Jpn. J. Appl. Phys., **36**, L899 (1997).

64. O.H. Nam, M.D. Bremser, T. Zheleva, R.F. Davis, Appl. Phys. Lett., **71**, 2638 (1997).

65. G. Li, S.J. Chua, S.J. Xu, W. Wang, P. Li, B. Beaumont, P. Gibart, Appl. Phys. Lett. **74**, 2821 (1999).

66. Z. Liliental-Weber, M. Benamara, W. Swider, J. Washburn, J. Park, P.A. Grudowski, C.J. Eiting, R.D. Dupuis, MRS Internet J. Nitride Semicond. Res. **4S1**, G4.6 (1999).

67. T.S. Zheleva, O.-H. Nam, M.D. Bremser, R.F. Davis, Appl. Phys. Lett. **71**, 2472 (1997).

68. T.S. Zheleva, W.M. Ashmawi, O.-H. Nam, R.F. Davis, Appl. Phys. Lett. **74**, 2492 (1999).

69. S. Nakamura, M. Senoh, S.-I. Nagahama, N. Iwasa, T. Yamada, T. Matsushita, H. Kiyoku, Y. Sugimoto, T. Kozaki, H. Umemoto, M. Sano, K. Chocho, Appl. Phys. Lett. **72**, 211 (1998).

70. H. Raidt, R. Kohler, F. Banhart, B. Jenichen, A. Gutjahr, M. Konuma, I. Silier, E. Bauser, J. Appl. Phys. **80**, 4101 (1996).

71. Rantamäki, T. Tuomi, Z.R. Zytkiewicz, D. Dobosz, P.J. McNally, J. Phys. D. **32**, A114 (1999).

72. R. Vetury, H. Marchand, G. Parish, P.T. Fini, J.P. Ibbetson, S. Keller, J.S. Speck, S.P. DenBaars, U.K. Mishra, H. Sakaki, J.-C. Woo, N. Yokoyama, Y. Hirayama, Proceedings of the Twenty-Fifth International Symposium on Compound Semicond., Nara, Japan, 1998, IOP Publishing, Bristol, UK. 1999, pp. 177.

73. F. Gerhard, Science, **278**, 1902 (1997).

74. S. Nakamura, M. Senoh, S.-I. Nagahama, N. Iwasa, T. Yamada, T. Matsushita, H. Kiyoku, Y. Sugimoto, T. Kozaki, H. Umemoto, M. Sano, K. Chocho, Jpn. J. Appl. Phys. **36**, L1568 (1997).

75. M. Razeghi, P. Sandvik, P. Kung, D. Walker, K. Mi, X. Zhang, V. Kumar, J. Diaz, F. Shahedipour, Mater. Sci. & Eng. B, **74**, 107 (2000).

76. S. Nakamura, 1997 Proc. 2nd Int. Conf. On Semiconductors, ICNS'97 (Tokushima, 1997), p444.

77. A. Sakai, H. Sunakawa, A. Usui, Appl. Phys. Lett. **73**, 481 (1998).

78. H. Marchand, J.P. Ibbetson, P.T. Fini, S. Chichibu, S.J. Rosner, S. Keller, S.P. DenBaars, J.S. Speck, U.K. Mishra, H. Sakaki, J.-C. Woo, N. Yokoyama, Y. Hirayama, Proceedings of the Twenty-Fifth International Symposium on Compound Semicond., Nara, Japan, 1998, IOP Publishing, Bristol, UK. 1999, pp. 681.

79. Y.H. Song, S.C. Choi, J.Y. Choi, J.W. Yang, G.M. Yang, Phys. Stat. Sol.(a) **180**, 247 (2000).

80. R. S. Qhalid Fareed, S. Tottori, T. Inaoka, K. Nishino, S. Sakai, J. Cryst. Growth, **207**, 174 (1999).

81. H. Sone, S. Nambu, Y. Kawaguchi, M. Yamaguchi, H. Miyake, K. Hiramatsu, Y. Iyechika, T. Maeda, N. Sawaki, Jpn. J. Appl. Phys. **38**, L356 (1999).

82. Z.R. Zytkiewicz, J. Domagala, D. Dobosz, J. Bak-Misiuk, J. Appl. Phys. **84**, 6937 (1998).

83. T. Tuomi, K. Naukkarinen, P. Rabe, phys. stat. sol. (a), **25**, 93 (1974).

84. L. Considine, E.J. Thrush, J.A. Crawley, K. Jacobs, W. Van der Stricht, I. Moerman, P. Demeester, G.H. Park, S.J. Hwang, J.J. Song, J. Cryst. Growth, **195**, 192 (1998).

85. R. Kohler, B. Jenichen, H. Raidt, E. Bauser, N. Nagel, J. Phys. D. **28**, A50 (1995).

86. http://www.ccp14.ac.uk/ccp/web-mirrors/lmgp-laugier-bochu/

87. R. Rantamäki, T. Tuomi, Z.R. Zytkiewicz, J. Domagala, P.J. McNally, A.N. Danilewsky, J. Appl. Phys. **86**, 4298 (1999).

88. H. Marchand, J.P. Ibbetson, P.T. Fini, S. Keller, S.P. DenBaars, J.S. Speck, U.K. Mishra, J. Cryst. Growth, **195**, 328 (1998).

89. Z.R. Zytkiewicz, J. Domagala, D. Dobosz, J. Appl. Phys. **90**, 6140 (2001).

4 Raman spectroscopy

4.1 Introduction

Electronic products have had a major impact on our way of life in the past decades; from computers to mobile phones, human beings are enjoying the greatest range of convenience, often courtesy of modern semiconductor techniques. Moore's law states that the amount of data storage in a microchip doubles every year or at least every 18 months, i.e. the number of bits per square centimeter doubles at least every 18 months [1]. This trend leads to an exponential rise in device speed, computational power, and smaller device structures. As the different thermal expansion coefficients of the various oxide, nitride and metal layers induce large mechanical stresses in the underlying silicon substrate, one result of the continuing reduction of feature size is the increase of mechanical stress in the device structures. Above a certain threshold, stress will trigger defects, cracking or formation of voids and will thus render the devices useless. Besides the detrimental influence on the fabrication process, mechanical stress also influences the electrical properties of the device even in the absence of any defects [2-3]. It is therefore necessary to measure mechanical stress during device processing so as to adjust the process parameters to avoid high stress, or occasionally to keep the high stress, for example for the making of stressed transistor channels [4-5]. In the latter case the carrier mobility can be increased and thus the devices speed are improved [6-7].

Furthermore, in the last few years [8-10] there has been a new interest in silicon (Si) technology, related to the development of Micro-Electro-Mechanical Systems (MEMS) in which sensor devices and micro-actuators are integrated together with the electronic circuits for signal processing and control. In such systems, the characterization of the electrical, optical, mechanical and thermal properties of the thin films and structures are also critical for the performance of the device. The study of both crystallographic and physical features of the structure is of high technological interest in order to improve the process steps in MEMS technologies.

In summary the rapid evolution in semiconductor technology, including device fabrication, thin-film deposition, interface preparation and microelectronic

processing, have increased the need for characterization techniques that can provide more precise information, especially on the structure of the materials. The quality of this information is one of the most critical factors in designing and manufacturing microelectronic devices since high performance integrated circuits and devices demand an excellent quality material, either in the form of bulk material, thin-film or device structures.

The increasing densification and miniaturisation of devices in microelectronics components demands analytical techniques with a very high spatial resolution, in general higher than the limit set by far field diffraction of visible light. This offers challenges for optical techniques, such as micro-Raman spectroscopy (μRS) [11]. In fact, several methods can deliver information on mechanical stress in semiconductor devices. The most important are X-ray diffraction, transmission electron microscopy (TEM), and micro-Raman spectroscopy. All of these methods have advantages and disadvantages. The criteria that decide the usefulness of a technique for stress measurements in silicon microelectronic technologies include spatial resolution, stress sensitivity, and measurement time. These criteria make micro-Raman spectroscopy one of the more suitable techniques for modern microelectronic device stress measurement.

X-ray diffraction [12-13] is very sensitive to small changes in the lattice constant, a_0, with a strain sensitivity of $\Delta a_0/a_0 \approx 10^{-7}$. The size of the probe spot for X-ray diffraction is usually in the range of 1 mm^2; the best spatial resolution of X-ray diffraction is around 30 μm, though this is inadequate to determine the stress distribution at a local area especially when the strain gradient is high [14], such as for modern devices. Since device dimensions are of the order of a micron (and submicron for recent advanced devices), the measurement of locally resolved stress on a device scale is impossible with X-ray diffraction technique.

The TEM methods [15-18], such as stress contrast in cross-sectional TEM (XTEM) and convergent beam electron diffraction (CBED), reach spatial resolutions of a few nanometres. The strain sensitivity of 10^{-4} is lower than that of X-ray diffraction, but is about the same as for micro-Raman spectroscopy. The main disadvantage of this technique is the destructive sample preparation and the extensive modelling required to extract the information on stress from the measurement [15-18]. The time using TEM to get the stress information is often in the range of weeks

or even months. This is impractical in an industry, where such information is often desired within hours or at the most within a few days.

Micro-Raman spectroscopy (μRS) reaches neither the stress sensitivity of X-ray diffraction nor the spatial resolution of TEM, but is yet very suitable method to deliver stress information on a microscopic scale. The strain sensitivity is the same as for TEM (10^{-4}) and the spatial resolution can reach around 0.6-1.0 μm [19-20]. The time it takes to gain information on mechanical stress in a device structure is often of the order of hours or minutes. These properties make μRS a useful method to monitor processing stress in microelectronic devices.

Micro-Raman scattering is an extremely powerful contactless tool which allows non-destructive and quantitative microanalysis of structural and electrical properties [5, 11, 21-27]. This technique is very useful since the micro-Raman signal is very sensitive to the microstructural state of the sample and other local environments, therefore giving information on the structure of the material. The Raman signal depends on the electron-phonon interaction, i.e. lattice vibrations. The greatest advantages of Raman spectroscopy are its ease of sample preparation, the short time required for obtaining data (data acquisition is automated and it takes a few seconds to acquire a spectrum at an individual location), and high spatial resolution for micro-Raman spectroscopy. This would be an obvious benefit to manufacturers wanting data quickly from the products in a non-destructive manner such that they can easily move on to the next stage in the process.

Raman spectroscopy has been well exploited in the field of semiconductor materials. It allows analyses of many kinds of materials with no sample preparation. Solids are easily studied by placing them on a standard glass microscope slide [11].

However for micro-Raman spectroscopy mechanical stress assessment, the information obtained is averaged over the probed sample volume, which is determined by the laser spot size and the penetration depth of the laser in the studied material. Another drawback of the micro-Raman spectroscopy technique is that this technique can not be used to measure the stress in pure metal [11, 22] due to the extremely short penetration of the electromagnetic radiation in the metal and the low Raman scattering efficiency of the metal.

4.2 Principles of Raman spectroscopy and micro-Raman stress measurement

The Raman effect was named after Prof. C.V. Raman, who published the observation of "a new type of secondary radiation" for the first time in 1928 [28].

When light encounters the surface of a material, most of the energy is reflected, transmitted, absorbed, or Rayleigh scattered, because of the first-order elastic interactions with phonons. There is no photon frequency change for this fraction of the light intensity. But a small fraction of the light, a few Raman-scattered photons, interacts inelastically with phonon modes, resulting in outgoing photons whose frequency is shifted with respect to the incoming values, i.e. their energies are changed as a consequence of their interaction with the phonons in the sample. These scattered photons gain energy by absorbing a phonon (anti-Stokes shifted), or lose energy by emitting a phonon (Stokes shifted), according to the energy and momentum conservation rules:

$$\hbar\omega_s = \hbar\omega_i \pm \hbar\omega_j \tag{4.1}$$

$$K_s = K_i \pm q_j \tag{4.2}$$

where $\hbar\omega_i$ is the incident photon energy, $\hbar\omega_s$ is the scattered photon energy and $\hbar\omega_j$ is the energy transferred for the elementary excitation; K_i is the incident photon wavevector, K_s is the scattered photon wavevector and q_j is the wavevector for the elementary excitation; the minus sign stands for the process in which an elementary excitation is generated (Stokes process), and the plus sign is for the process in which an elementary excitation is annihilated (anti-Stokes process) [21]. The schematics for the three basic processes, i.e. Rayleigh Scattering, Stokes Scattering and anti-Stokes Scattering, are shown in Figs. 4.1-4.3.

Usually the Raman spectra are plotted against emitted photon energy in units of wavenumber, which is the reciprocal of the wavelength in units of cm^{-1} [27].

From the point of view of solid state physics, the vibrations of crystal atoms are described as collective motion waves (i.e. lattice vibrations), each possible vibration j being characterized by a wavevector q_j and a frequency ω_j. The vibration amplitude at position r is expressed as:

$$Q_j = A_j \exp[\pm i(q_j \cdot r - \omega_j t)] \tag{4.3}$$

where Q_j is the normal coordinate of the vibration, A_j is a constant.
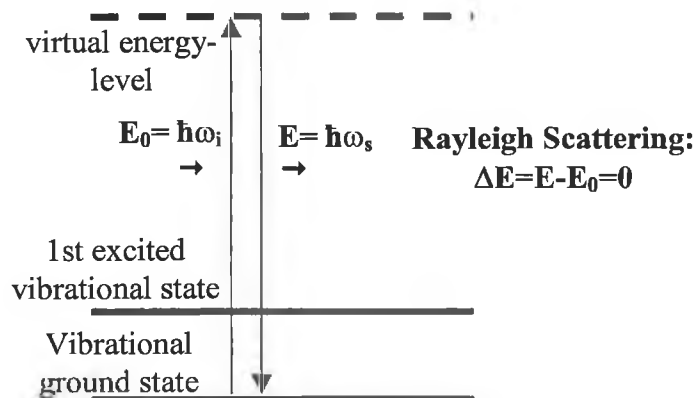
Figure 4.1 Schematic of Rayleigh Scattering. The atom is excited by a photon, $E_0 = \hbar\omega_i$, to a virtual energy-level, which is in fact a distortion of the electron distribution of a covalent bond. The atom returns to the vibrational ground state while emitting the same amount of energy, $E = \hbar\omega_s$.
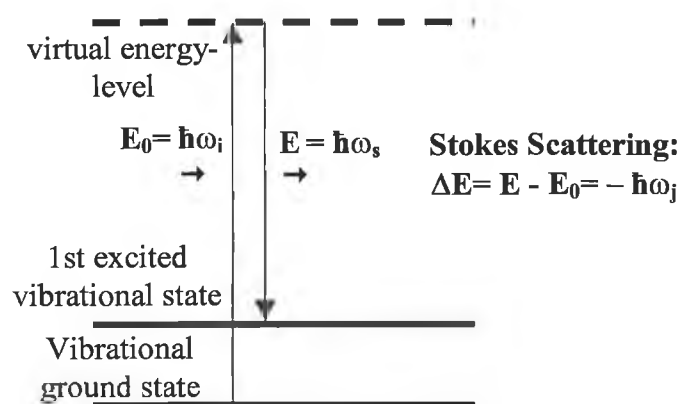
Figure 4.2 Schematic of Stokes Scattering. The atom is excited to a virtual energy-level, which is in fact a distortion of the electron-cloud, by absorption of a photon $E_0 = \hbar\omega_i$. The atom returns to the first excited vibrational state and emits the energy difference as a photon with lower energy, $\Delta E = E - E_0 = -\hbar\omega_j$. The radiation with lower energy (higher wavelength) is called Stokes Scattering.

virtual energy-level

$E_0 = \hbar\omega_i$ $E = \hbar\omega_s$ **anti-Stokes Scattering:**

$\Delta E = E - E_0 = \hbar\omega_j$

1st excited vibrational state

Vibrational ground state
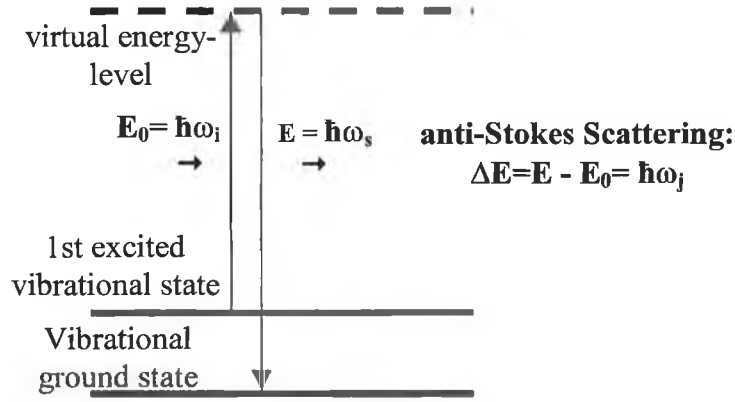
Figure 4.3: Schematic of anti-Stokes Scattering. The atom is situated on the first excited vibrational level, and absorbs a photon with energy $E_0 = \hbar\omega_i$. Again the atom is excited to a virtual energy level, which is higher in energy than is the case with Rayleigh and Stokes Scattering. The atom relaxes, and returns to the vibrational ground state, emitting the energy difference as a photon with energy $\Delta E = \hbar\omega_j$. This results in light with a shorter wavelength and is called anti-Stokes Scattering.

When monochromatic light of frequency ω_i is incident on a crystal in a direction k_i, at position r, the associated electric field E will induce an electric dipole moment P with the following relationship:

$$P = \varepsilon_0 \chi \cdot E = \varepsilon_0 \chi \cdot E_0 \exp[i(k_i \cdot r - \omega_i t)] \tag{4.4}$$

where χ is the susceptibility tensor. It describes the response of the crystal to the electric field. The susceptibility may change as a function of the atomic vibration, and it can be expanded into a Taylor series with respect to the normal coordinate of the vibration Q_j [11]:

$$\chi = \chi_0 + \left(\frac{\partial \chi}{\partial Q_j}\right)_0 Q_j + \left(\frac{\partial^2 \chi}{\partial Q_j \partial Q_k}\right)_0 Q_j Q_k + \cdots \tag{4.5}$$

The first term is related to the Rayleigh scattering, the second term is related to the first-order Raman scattering. The third term is related to second-order Raman scattering, where two phonons are involved. Higher order Raman scattering will not be discussed here. Combining equations (4.4) and (4.5), then the electric dipole moment can be expressed as:

$$P = \varepsilon_0 \chi_0 \cdot E_0 \exp[i(k_i \cdot r - \omega_i t)] + \varepsilon_0 A_j E_0 \left(\frac{\partial \chi}{\partial Q_j}\right)_0 \exp[i(k_i \pm q_j) \cdot r - i(\omega_i \pm \omega_j)t] \tag{4.6}$$

The first term give rise to Rayleigh Scattering. The second term describes the anti-Stokes (for plus) and Stokes scattering (for minus) with frequencies $\omega_i \pm \omega_j$. The second term (Raman scattering) will be observed only when:

$$\chi^{(1)} = \left(\frac{\partial \chi}{\partial Q_j}\right)_0 \neq 0 \qquad (4.7)$$

The elements of $\chi^{(1)}$ are referred as the Raman tensor components, and these carry the geometric information of the sample crystal. The exact form of the Raman tensor depends on crystal symmetry, and they have been derived by Loudon [29] for all crystal types. For silicon, in the orthonormal coordinate system $X=[100]$, $Y=[010]$, $Z=[001]$, the Raman tensors have the form:

$$R_x = \begin{pmatrix} 0 & 0 & 0 \\ 0 & 0 & d \\ 0 & d & 0 \end{pmatrix} \qquad (4.8a)$$

$$R_y = \begin{pmatrix} 0 & 0 & d \\ 0 & 0 & 0 \\ d & 0 & 0 \end{pmatrix} \qquad (4.8b)$$

$$R_z = \begin{pmatrix} 0 & d & 0 \\ d & 0 & 0 \\ 0 & 0 & 0 \end{pmatrix} \qquad (4.8c)$$

The full calculation of Raman intensity is difficult, but the qualitative intensity I for the observed Raman band is [27]:

$$I \propto \left| \hat{e}_i \cdot R_j \cdot \hat{e}_s \right|^2 \qquad (4.9)$$

where $\hat{e}_i$ and $\hat{e}_s$ are unit vectors giving the directions of the incident and scattered electric field respectively, and R_j is the Raman tensor. Equation (4.9) determines which phonon modes are allowed or forbidden for different sample orientations.

Usually the Stokes modes are stronger and dominate in measurement [27]. The mode strengths depend on the number of phonons available, which is a count of the distribution of normal mode harmonic oscillators in the lattice as a function of temperature. The relative strength of the anti-Stokes line to the Stokes line can be expressed as [27]:

$$\frac{I_{anti-Stokes}}{I_{Stokes}} = e^{-\frac{\hbar\omega_j}{k_BT}}$$

(4.10)

where k_B is the Boltzmann constant and T is the sample temperature in Kelvin. The anti-Stokes line intensity decreases to zero as T reaches 0 K. The intensity ratio between Stokes and anti-Stokes processes can sometimes be used to determine the sample temperature and local temperature distribution of the sample [30-31].

The Raman scattering has a frequency equal to one of the lattice vibrations, it is a second order inelastic scattering process and inherently a weak process, typically 1 in 10^7 photons being scattered by a Raman process [22]. As long as the lasers provide enough power, the Raman spectra can still be routinely measured.

Despite the Raman signal being usually very weak, its intensity increases dramatically if the energy of the incident laser matches a fundamental gap in the semiconductor band structure. It is therefore possible to study the band features of the studied semiconductor by this method [27].

Raman scattering is a very sensitive technique to probe local atomic environments. The properties of the vibrational modes are basically determined by the mass, bond type and symmetry of the constituting atoms in the elemental unit of a sample, which can be solid (primitive unit cell), liquid (molecule) or gas (molecule). Any physical factor affecting the short-range order of the sample, such as defects or impurities, has a direct impact on the atomic vibrational properties. These modifications of the vibrational characteristics are easily detected in the Raman spectrum features. Initially, Raman spectroscopy was used extensively to study the excitation and vibrational properties of molecules. In 1970, Anastassakis *et al.* started to study the effects of stress on the optical phonon modes, and since then this method was developed for stress characterization [5, 11, 21, 23-26, 32-33].

Micro-Raman spectroscopy can be used for the analysis of residual stresses, as mechanical stress will affect the frequencies of the Raman bands, and lift their degeneracy. For example, in crystal Si the triple degeneracy optical phonon with frequency ω_0 is lifted in the presence of a symmetric strain, which itself is caused by anistropic changes in the lattice constants [21]. The three optical modes in the presence of elastic strain can be obtained by solving the following secular equation [11]:

$$\begin{vmatrix} p\varepsilon_{11} + q(\varepsilon_{22} + \varepsilon_{33}) - \lambda & 2r\varepsilon_{12} & 2r\varepsilon_{13} \\ 2r\varepsilon_{12} & p\varepsilon_{22} + q(\varepsilon_{33} + \varepsilon_{11}) - \lambda & 2r\varepsilon_{23} \\ 2r\varepsilon_{13} & 2r\varepsilon_{23} & p\varepsilon_{33} + q(\varepsilon_{11} + \varepsilon_{22}) - \lambda \end{vmatrix} = 0 \quad (4.11)$$

where p, q, r are phonon deformation potentials, i.e. material constants; ε_{ij} are the strain tensor components. The above equation is given in the crystal coordinate system, though it is usually much easier to solve the secular equation in the sample coordinate system [25-26]. For that purpose the strain tensors, ε_{ij}, must be given in the sample axis system also. After calculating the eigenvalues λ_j (j=1, 2, 3) of the above secular equation, the Raman frequency shift of each mode in the presence of stress relative to the strain free degenerate frequency, ω_0, can be obtained with the following relationship [11]:

$$\lambda_j = \omega'_j{}^2 - \omega_0{}^2 \quad (4.12)$$

Since ω'_j is usually very close to ω_0,

$$\therefore \lambda_j = (\omega'_j + \omega_0) \cdot (\omega'_j - \omega_0) \approx 2\omega_0 \cdot (\omega'_j - \omega_0) \quad (4.13)$$

$$\Rightarrow \Delta\omega_j = \omega'_j - \omega_0 \approx \frac{\lambda_j}{2\omega_0} \quad (4.14)$$

It is not practical to give a general solution to (4.11), but is simple for the two most common cases: uniaxial stress and biaxial stress, which apply to many situations in microelectronic device structures. For example, the uniaxial stress is often a good approximation in the centre of overlayer lines or at least a certain distance away from the edges.

In the case of uniaxial stress in Si crystal, for backscattering from the z'=[001] direction, according to the Raman selection rule with $e_i=e_s=(100)$, only the third Raman mode can be observed. The relation between the measured Raman shift and the stress can be obtained from (4.11) and (4.14) to be [21]:

$$\Delta\omega_3 = \frac{1}{2\omega_0}[pS_{12} + q(S_{11} + S_{12})]\sigma_0 \quad (4.15)$$

where S_{ij} is the elastic compliance tensor element of silicon. The strain free degenerate frequency ω_0 of crystal silicon is about 520 cm^{-1}. The phonon deformation potentials (p, q and r) and the elastic compliance tensor element (S_{ij}) are material properties. Values of the theoretical and experimental phonon deformation potentials from different authors differ from each other [34-38], thus different literature sources produce different relations between the measured Raman shift and

the stress, and the stress determined from the Raman shift varies consequently. However for uniaxial stress, the relation between the measured Raman shift and the stress is often regarded as [11]:

$$\Delta\omega_3 = -2\times10^{-9}\sigma \qquad (4.16)$$

where $\Delta\omega_3$ is given in units of cm^{-1} and σ in Pascal (Pa). The parameters for the above relation are from reference [32], which are $p=-1.43\omega_0^2$, $q=-1.89\omega_0^2$, $S_{11}=7.68$ x 10^{-12} Pa^{-1} and $S_{12}=-2.14$ x 10^{-12} Pa^{-1}. Equation (4.16) shows that the Raman band is sensitive to the presence of stresses or strains in the scattering volume: a tensile stress will increase the lattice spacing and, hence, induce a decrease in the wavenumber of the vibrational mode. In the case of compressive strain, the decrease of the lattice parameter yields a corresponding increase of the vibrational frequency. In the elastic regime, these shifts depend in a linear way on the magnitude of the stress, and the position of the Raman band can be used to measure the stress.

In case of biaxial stress in the *X-Y* plane, with stress components σ_{xx} and σ_{yy}, the relation between the stress and the measured Raman shift is:

$$\Delta\omega_3 = -4\times10^{-9}\left(\frac{\sigma_{xx}+\sigma_{yy}}{2}\right) \qquad (4.17)$$

For GaN, experimental results indicate that the relation between in-plane biaxial stress $\dfrac{\sigma_{xx}+\sigma_{yy}}{2}$ in the epilayer and the measured Raman shift $\Delta\omega$ is [39]:

$$\Delta\omega = -4.2\times10^{-9}\left(\frac{\sigma_{xx}+\sigma_{yy}}{2}\right) \qquad (4.18)$$

Similarly, $\Delta\omega$ is given in units of cm^{-1} and σ in Pascal (Pa). $\Delta\omega$ is the GaN E_2 Raman peak shift under stress relative to the stress free wave number at 568 cm^{-1} [40-41].

Besides crystal materials, the micro-Raman technique is also a powerful tool in identifying stress and strain in polycrystalline silicon structures used for the fabrication of large polysilicon micromechanical structures [42-44]. These micromechanical systems based on surface-micromachining technologies can have serious stress effects that can cause mechanical device failure, curling or fracture.

Relations between the stress and the Raman peak shift under stress for other materials can be found in the literature [45].

As described above, the relation between the measured Raman shift and the stress has been well studied for many materials. Based on this knowledge, the author

measured stress distributions in a few selected semiconductor materials with the micro-Raman technique in this study. However the strong dependence of the Raman experimental frequency (bandwidth and intensity as well, which will be discussed later in this chapter) on the structural features in the scattering volume calls for extremely accurate measurement of the Raman line. So the experimental conditions should be as stable as possible.

Many factors can affect the Raman band frequency, and one such important factor is the temperature in the room where the spectrometer is installed. Variation in the laboratory temperature produces subtle mechanical changes in the diffraction gratings and optical parts. When high resolution measurements are required, the laboratory temperature stability should be better than $\pm 1^\circ C$. However some of these effects can be corrected (mainly for the frequency shift) by measuring reference samples with well known bands, such as a single crystal reference Si wafer (520 cm^{-1}). Another possibility is to use the plasma lines of the laser beam as internal calibration lines. In this study, a plasma line was used as the internal calibration and the equipment itself was calibrated with single crystal reference Si wafers from time to time. Fig. 4.4a shows a mapping of the GaN E_2 Raman peak position ($\approx$568 cm^{-1}) along an area of an ELO GaN epilayer on sapphire [46-48] as shown in Fig. 4.4b. Fig. 4.4a was obtained without internal plasma line calibration, while the environmental temperature of the spectrometer varied during the measurement, which took more than 10 hours and spanned from daytime to night. In the measurement, the sample was placed on a motorized X-Y stage with a minimum step size of 0.1 μm. So the laser scanned the sample along the X axis from left to right, and then from top to bottom along the Y axis. The measurement started in the afternoon when the room temperature is about 5°C higher than when the measurement finished in the early morning next day. It can be seen from Fig. 4.4a that the GaN E_2 Raman peak position appears higher when the ambient temperature is higher and decreases gradually as the ambient temperature drops. In this study, a plasma line around 561 cm^{-1} was used as an internal reference for the GaN E_2 Raman peak position correction. Even though the sample surface stress differs from point to point (thus the GaN E_2 Raman peak position changes also), the plasma line peak position should be at a fixed position if the equipment condition stays the same. The ambient temperature variation and equipment condition changes will cause both the
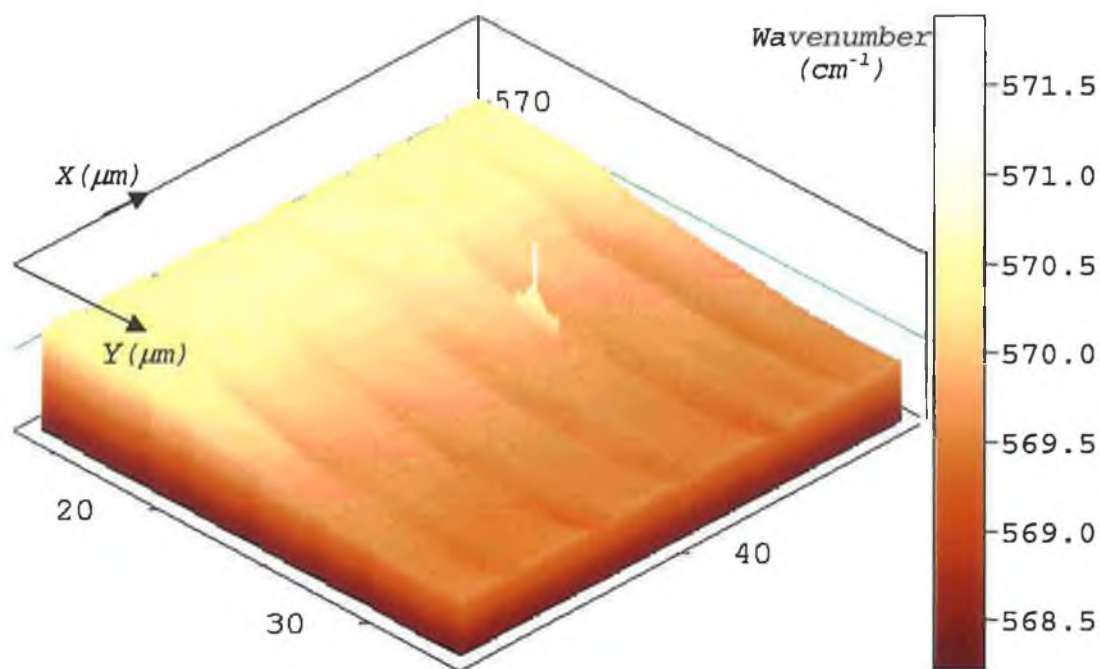
(a)
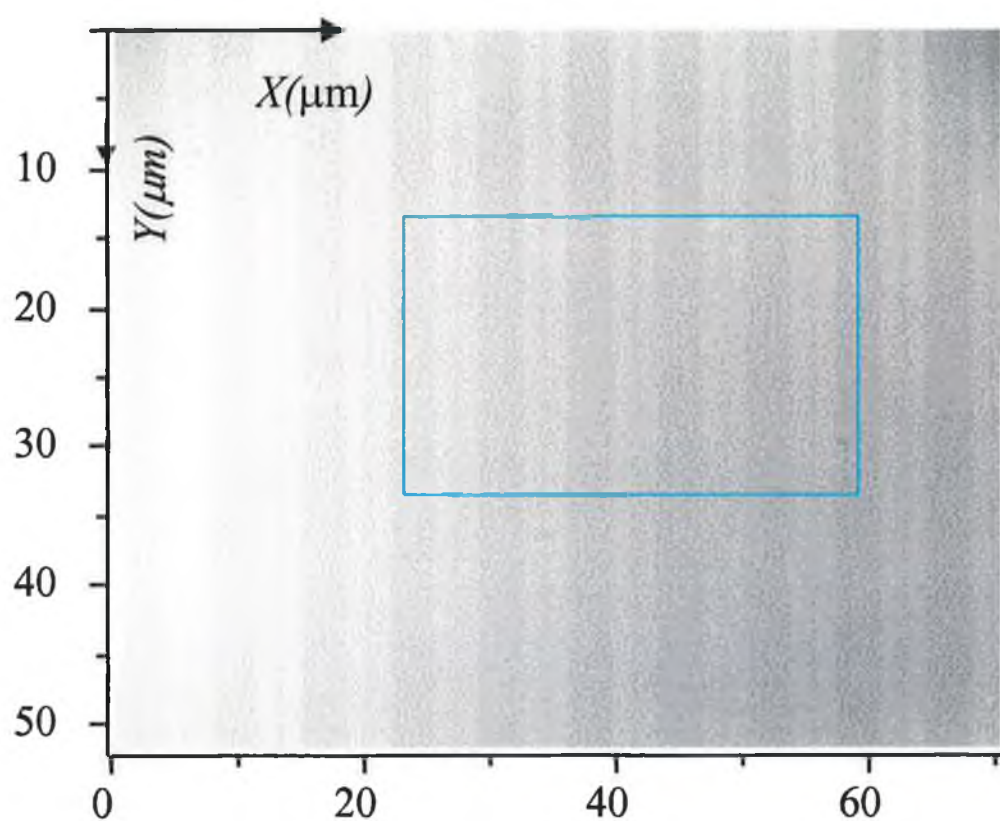
(b)

Figure 4.4: (a) Mapping of GaN E_2 Raman peak position ($\approx$568 cm^{-1}) in an area of 36.1 μm x 20 μm as indicated in the square area of (b) in the Epitaxial Lateral Overgrowth of a GaN sample on sapphire without the internal plasma line calibration for Raman peak position.
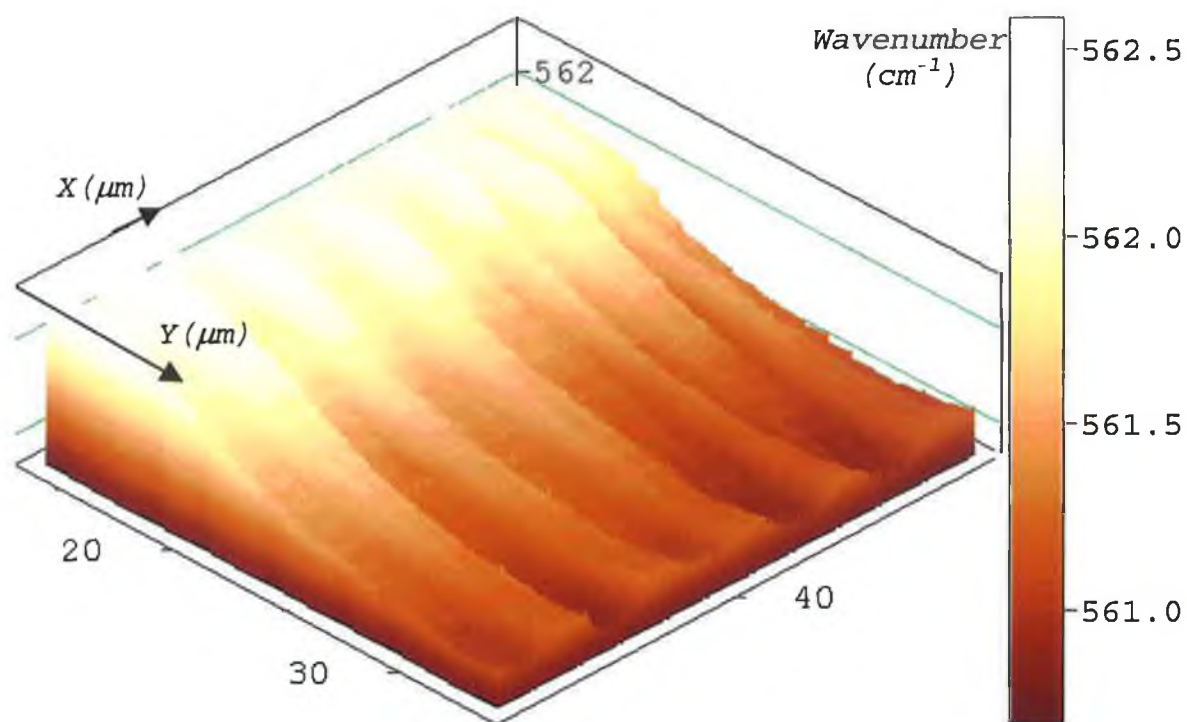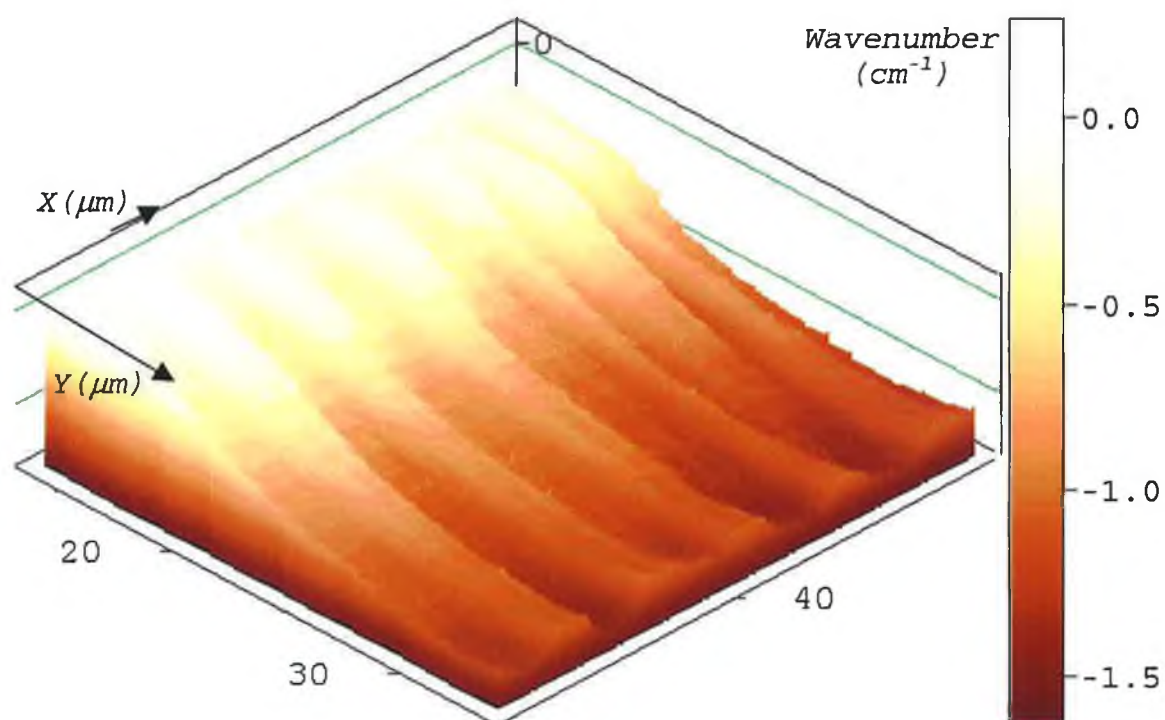
Figure 4.5 (a) Mapping of plasma line peak position during the ELO GaN stress measurement as indicated in Fig. 4.4; (b) Plasma line peak position variation during measurement.

plasma line and the GaN E_2 Raman peak position movement. After obtaining the plasma line peak position variation data during the measurement (Fig. 4.5b), the GaN E_2 Raman peak position variation caused only by the stress difference can be easily calculated by subtraction of the two mapping data. This kind of calculation can be performed conveniently with software provided by the equipment manufacturer. Thus stress information of the studied sample can be accurately obtained [46-49].

4.3 Experimental set-up for micro-Raman spectroscopy

In this study, a Jobin Yvon LabRam HR800 micro-Raman spectroscopy system was used for the stress measurement [5, 48]. In the micro-Raman technique, the incident monochromatic laser beam is reflected by a beam splitter and a flip mirror onto the microscope objective which focuses the laser on the specimen surface. The scattered light is recollected through the same microscope objective (back-scattering configuration), passes through the beam splitter and is focused onto the entrance slit of the spectrometer that disperses the Raman scattered light onto a CCD detector (which is cooled with liquid nitrogen in the LabRam HR800). Finally the spectrum is analysed. The flip mirror situated in the microscope also permits us to visualize the microscopic region under analysis with a TV camera. In the case of materials opaque to the laser, such as most semiconductors, the visualization of the sample in the camera must be achieved with a bright field reflection illumination system. A typical micro-Raman instrument is shown in Fig. 4.6 [11]. It is clear that this is a rather complex optical instrument. The advantage of using a back-scattering set-up is that the laser spot on the sample can be directly observed on the TV monitor which allows precise identification of the microscopic region of the sample analyzed.
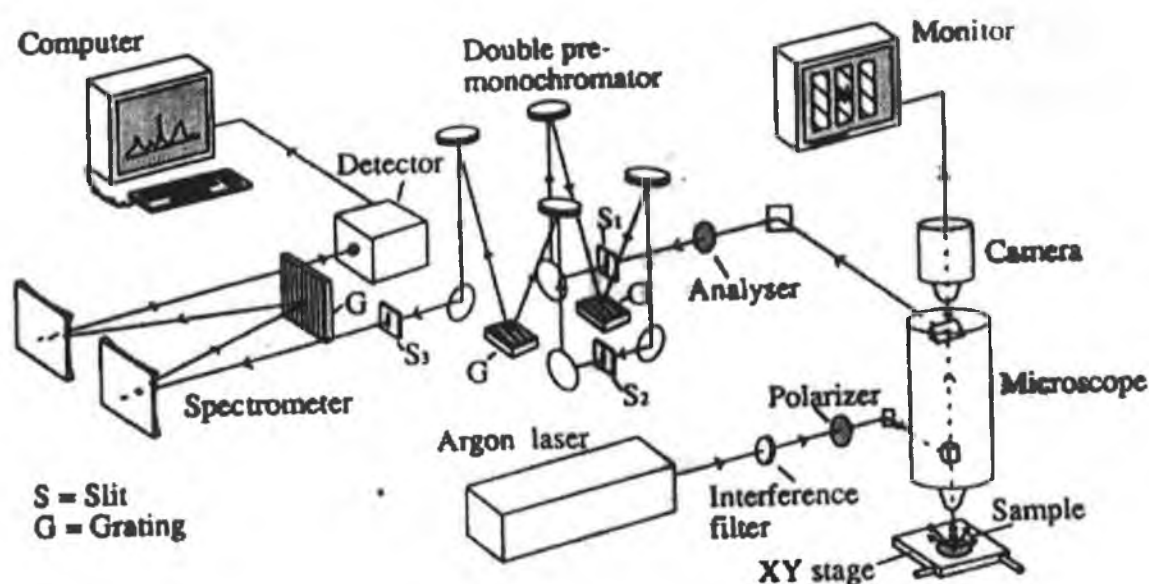
Figure 4.6 Experimental set-up of a typical micro-Raman spectrometer [11].
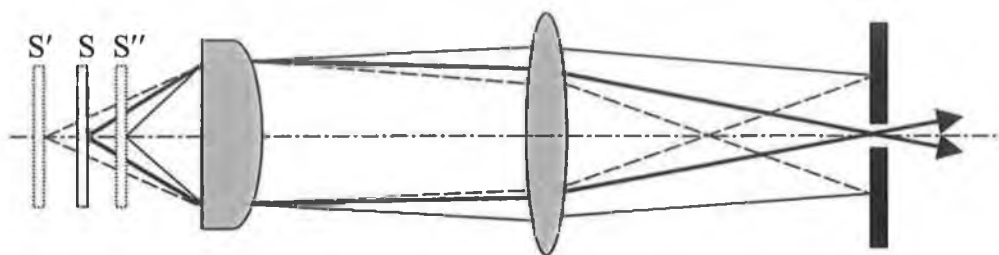
Figure 4.7 Schematic of confocal entrance optics for the LabRam HR800

For the LabRam HR800, the confocal technique is employed in the entrance optics. As shown in the schematic of Fig. 4.7, this confocal technique allows rejection of radiation originating away from the focal point conjugate to the confocal aperture. The radiation from the S′ and S″ planes does not pass through the aperture, because they are not focussed in the confocal plane. Thus, Raman radiation originating away from the sample depth of interest never reaches the entrance to the spectrograph, so that the acquired spectrum is specific to the depth of the sample in focus. The HR800 confocal entrance optics enables astigmatism correction and provides an adjustable confocal pinhole; pinholes with 50μm, 100 μm, 150μm and 200 μm diameters can be chosen conveniently via the control software of the LabRam HR800 system, thus different resolutions and signal intensities can be obtained for the experimental results. The confocal design requires very accurate optical alignment with a high degree of stability and reproducibility not previously obtainable with conventional laser spectrometers.

4.4 Spatial resolution and spot size

An important point that has to be considered in microanalysis with micro-Raman spectroscopy is the spatial resolution. The spatial resolution of the Raman instrument depends on the focused beam size on the sample and the wavelength. A useful definition of the spot size is given by defining the diameter of a diffraction limited spot to be the diameter at which the intensity of the spot has decreased to $\frac{1}{e^2}$ of its value in the middle of the spot, $I(0)$. This kind of spot is obtained by having a laser beam with a diameter much larger than the entrance aperture of the focusing lens (uniform illumination) and is the smallest spot we can ever obtain with ordinary optics. It has an intensity profile of the form:

$$I(r) = I(0) \left[\frac{2J_1(r)}{r} \right]^2 \tag{4.19}$$

with $J_1(r)$ a Bessel function of the first kind of order one, and r the distance to the middle of the spot [50].

The diffraction limited spot reaches its $1/e^2$ intensity value at a radius r with:

$$r = \frac{0.88\lambda}{2NA} \tag{4.20}$$

so its diameter is given by

$$\emptyset = \frac{0.88\lambda}{NA} \tag{4.21}$$

where λ is the wavelength of the light, and NA is the numerical aperture of the objective. NA = $n_i\sin\theta$, the angle θ is the angle the outer rays make with the optical axis, and n_i is the refractive index of the material surrounding the object. For a typical x100 microscope objective used in the experiment in this study, NA=0.95. This is the fundamental minimum spot size. Considering the Ar^+ blue laser wavelength (λ=488nm) for the LabRam HR800, equation (4.21) produces a theoretical spot diameter of 0.45 μm (NA≈0.95).

The Rayleigh criterion [20]

$$r = \frac{1.22\lambda}{2NA} \tag{4.22}$$

gives us the radius of the ring at which the first zero of the Bessel function occurs.

The actual laser beam spot size can be determined experimentally in the conditions of routine micro-Raman experiments by recording successive Raman spectra at different positions across a sharp metal (which is opaque to the laser light) edge over the Si substrate or similar samples [21] using a microscope XY translation stage controlled by a computer to probe the Raman signal across the interface. The intensity of the Raman band of Si at 520 cm^{-1} was measured for each spectrum recorded and plotted as a function of the analyzed position.

Eq. (4.21) or (4.22) means that by using lenses with higher NA, or applying a shorter wavelength UV laser, the micro-Raman spectroscopy resolution can be improved. Ordinary objectives (with a sample in air) are limited to $n_i = 1$ (refractive index of air) to a maximum NA ≈ 1 (sin $\theta \leq 1$ always). By using oil immersion lens (NA ≈ 1.4) [19] or solid immersion lens with the index of refraction greater than one, the spectroscopy resolution can be improved. A spatial resolution of about 0.5 μm was reported with the 457.9 nm laser after using the oil immersion lens [19].

As pointed out above, the UV-μRS approach is very promising, but in practice the UV-μRS spot size reduction is smaller due to the lack of good objectives with high numerical aperture in the UV region. The resolution of current UV-Raman instruments is about 1 μm [20]. When the UV laser is employed in the measurements, a special objective is needed. For the LabRam HR800, a special objective with a magnification of 40 is employed for the 325 nm UV laser source.

Due to the high power density of the laser on the sample surface caused by the focusing of the laser beam with the microprobe, typically between 10^4-10^5 W cm^{-2}, precautions should be taken to use as low a laser power as possible. Otherwise samples under measurement with high optical absorption in the spectral region close to the laser frequency will be locally overheated and damaged, and the Raman spectrum shape, intensity and wavenumbers of bands will also be affected since the local heating of the crystalline network causes anharmonic effects in the spectra. However, this effect is totally reversible and is determined by the temperature gradient in the scattering volume of the sample [51]. The laser energy absorption is higher for highly damaged or amorphous semiconductors, thus the local overheating effects are more serious for those materials. In this study, the output laser power from the equipment is limited to a safe value (≤ 18 mW) and the actual laser power on the sample surface is smaller.

4.5 Penetration depth of the laser beam in the sample

When the laser beam passes through the semiconductor, its intensity decreases as a result of absorption of the material. Upon passing through the semiconductor to a depth d, the light intensity I_d can be expressed as [27]:

$$I_d = I_o e^{-\alpha d} \qquad (4.23)$$

where I_o is the original light intensity at the sample surface, α is the absorption coefficient of the specific light wavelength in this material (its value can be obtained from reference [52] for some common materials).

One definition for the penetration depth d_p or skin depth is defined as the depth at which the laser intensity decreases to $1/e$ of its original intensity [52], i.e.

$$\frac{I_d}{I_o} = \frac{1}{e} \qquad (4.24)$$

Then $d_p = \frac{1}{\alpha}$. But in studies [11], the penetration depth is given by the depth that satisfies the following relationship:

$$\frac{I'_d}{I_s + I'_d} = 0.1 \qquad (4.25)$$

where I_s is the total scattered light intensity integrated from the surface to a depth d, which is given by [53]:

$$I_s = I_0 D \int_0^d e^{-2\alpha x} dx = \frac{I_0 D}{2\alpha} (1 - e^{-2\alpha d}) \qquad (4.26)$$

and I'_d is the total scattered light intensity integrated from the depth d to infinity, which is given by:

$$I'_d = I_0 D \int_d^\infty e^{-2\alpha x} dx = \frac{I_0 D}{2\alpha} e^{-2\alpha d} \qquad (4.27)$$

In equations (4.26) and (4.27), D is the Raman scattering cross section. I_0 and α have the same meaning as before. According to the definition of (4.25), the penetration is then given by:

$$d_p = \frac{-\ln 0.1}{2\alpha} = \frac{2.3}{2\alpha} \qquad (4.28)$$

Therefore there are small differences in the calculated penetration depth according to different definitions. In this study, the laser penetration depth is calculated according to equation (4.28).

Since there are different penetration depths for different wavelength laser beams, it is possible to probe to different depths, from a few nanometres to about 10 µm, within the sample. Higher penetration depths can be achieved by decreasing the excitation energy, because optical absorption decreases for energies in the visible-near infrared region. The LabRam HR800 is one of the most popular Raman microprobes now on the market. Two laser beams, a HeCd UV laser with a wavelength of 325 nm and a visible argon ion laser with a wavelength of 488 nm, were supplied with our apparatus. The two laser beams can be changed conveniently without moving the sample. As a result, stress information at different depths for the same location can be detected easily [5].

Actually the optics of the LabRam HR800 is designed for excitation from the UV to the near IR.

Since stress decreases quickly into the substrate and changes by orders of magnitude within a few nanometers away from the edge or surface where stress is created [21], an assessment of the true near-surface stress is desirable. The true near surface stress can be assessed very well using micro-Raman spectroscopy with the UV excitation in the LabRam HR800 [5].

4.6 Other applications of Raman spectroscopy

Different parameters and varied information can be obtained from the Raman spectrum of solid state materials. Besides the stress information of the studied sample as described previously, by analyzing the Raman spectrum, other information related to structure and physical properties of the studied samples can be obtained also:

4.6.1 Frequency

The frequency of the phonon Raman band depends on the interatomic forces (i.e. force constants of the bonds), the bond length, and the masses and positions of the atoms. Any factor affecting these features will produce a change in the frequency of the band.

Besides stress in the sample, the presence of crystalline disorder also gives rise to changes in the frequency of the band, usually towards lower wavenumbers. These are related to the breaking of translational symmetry in the crystal, which can be produced by structural defects such as dislocations or by grain boundaries in nanocrystalline materials.

Other factors affecting the frequency of the Raman band are the temperature which has been discussed already, and the presence of chemical impurities in the crystalline network which leads to changes in the mass of the atoms in the lattice sites. For example, the presence of Ge atoms at substitutional positions in the Si network produces a decrease in the frequency of the vibrational modes, due to a higher Ge mass. This is known as the chemical effect [51]. The presence of impurities at substitutional positions also affects the lattice spacing due to the different size of the impurity. Hence, a stress effect will also occur in addition to the chemical one [51]. As a result, Raman spectroscopy can be used also as an useful complementary method to X-ray diffraction for the characterization of heteroepitaxial layers. The Raman spectrum of $Si_{1-x}Ge_x$ alloys presents three main lines, related to Si-Si at about 500 cm^{-1}, Si-Ge around 400 cm^{-1} and Ge-Ge about 300 cm^{-1} vibrational modes. A typical $Si_{1-x}Ge_x$ spectrum is shown in Fig. 4.8. The line at around 220 cm^{-1} is the folded acoustical mode and is related to the layered sample structures [54] of the virtual substrate upon which this Raman spectrum was measured [5]. It was shown [55] that the wavenumber of these modes present a linear relation with respect to both chemical composition and strain. For example, the
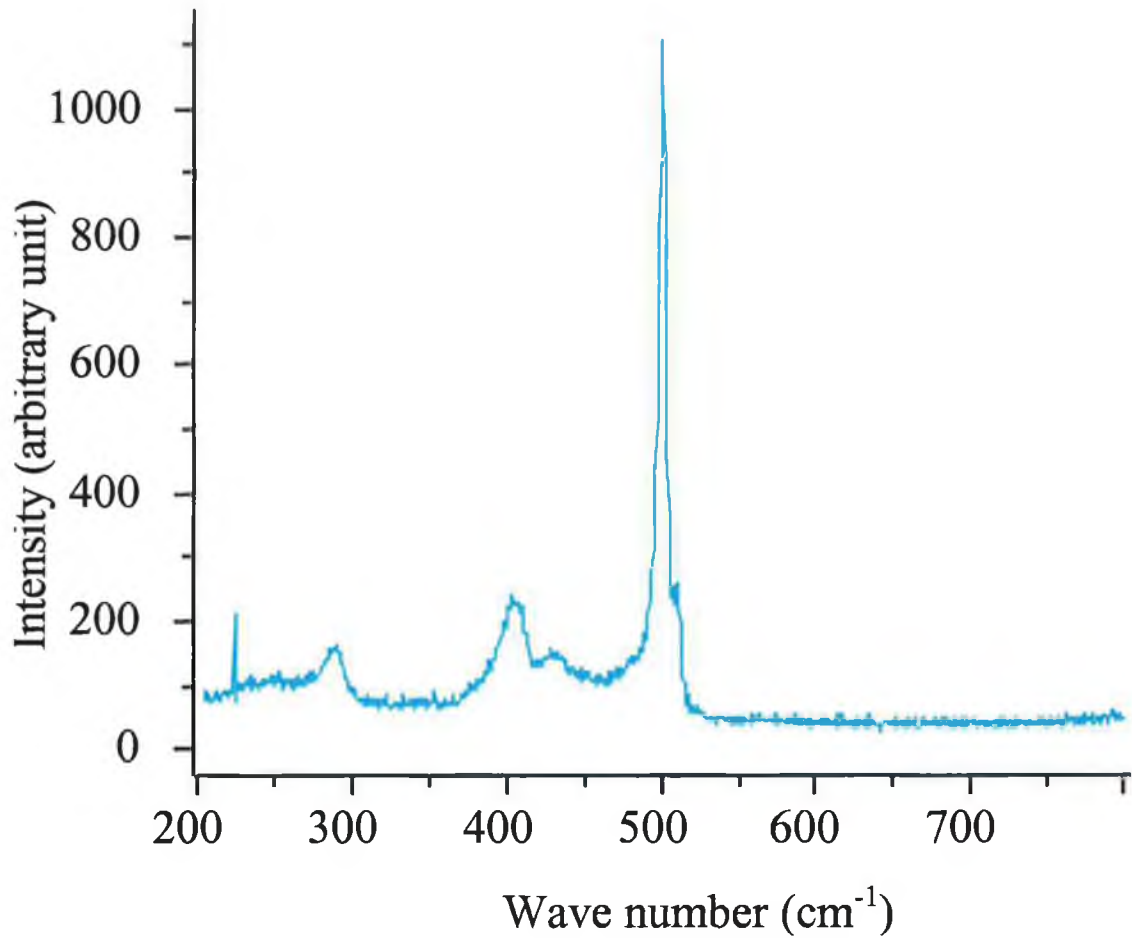
Figure 4.8 A typical $Si_{1-x}Ge_x$ Raman spectrum.

following relationships were reported:

$$\omega_{Si-Si} = 520 - 68x - 830\sigma \tag{4.29a}$$

$$\omega_{Si-Ge} = 500.5 + 14.2x - 575\sigma \tag{4.29b}$$

$$\omega_{Ge-Ge} = 282.5 + 16x - 384\sigma \tag{4.29c}$$

where ω is the wavenumber of the Raman mode, x the chemical composition and σ the strain parallel to the substrate. Similarly the above relationships may have some small variations in different studies [56-57]. So a single Raman spectrum of $Si_{1-x}Ge_x$ allows the determination of silicon and germanium contents as well as strain. In this study, the Raman band positions of a $Si_{1-x}Ge_x$ virtual substrate were measured and analysed for stress information with the LabRam HR800 [5].

4.6.2 Raman bandwidth and bandshape

Raman bandwidth and bandshape are closely related to the crystalline order. For crystalline Si, the Raman spectrum has a well defined single line at about 520 cm^{-1}. This line has a Lorentzian shape, with a full width at half maximum of approximately 3 cm^{-1}. In principle the bandwidth is related to the lifetime of the phonons. The presence of crystalline disorder decreases the phonon lifetime thus generating an increase of the bandwidth [51]. Therefore the density of defects can be evaluated from the bandwidth. The bandshape of the Raman line is also affected by confinement of phonons (for example in the case of polycrystalline structures where the phonons are confined in crystalline grains of average size L), these being defined by a correlation length model [58]. This correlation length is defined as the characteristic size of crystalline domains in the scattering volume where the translational symmetry of the crystal holds, and is related to the average distance between defects for damaged crystals or to the grain size for nanocrystalline materials. The position and shape of the Raman band can be simulated with a correlation length model [58] which allows one to estimate the value of the correlation length L, the average stress, as well as the density of defects in highly damaged Si films [59] in the scattering volume. This is useful for nanocrystalline materials where the average grain size is given by the correlation length. The main limit for this measurement is that phonon confinement only occurs for sizes in the nanometric range (L<20nm for Si).

In general the application of these models for grain size assessment has to take into account the fact that these are very simple models in which stress is assumed not to affect the shape of the Raman line and both stress and correlation lengths are assumed as uniform in the scattering volume.

For amorphous materials, the lack of long-range order yields a breakdown of the momentum conservation rule, and all the phonons become Raman active. For amorphous silicon, four broad bands centred at about 150 cm^{-1}, 310 cm^{-1}, 380 cm^{-1} and 480 cm^{-1} may appear in the spectrum, the broad peak at 480 cm^{-1} being the strongest [45]. It has been shown that the width of the TO mode is a good measure of local order which provides a tool for the structural assessment of the amorphous layers.

4.6.3 Raman intensity

The intensity of the Raman band is very sensitive to the structure of crystals and as a result significant information can be obtained from intensity measurements. Damage in the lattice leads to a decrease of the intensity of the first order modes, related to the breaking of bonds and changes in atomic force displacements, and, hence produces a decrease of the Raman polarizability tensors. For example, ion bombardment during doping processes will alter the original crystal with a consequent reduction of the Raman signal intensity. The measurement of the intensity of the Raman band can be applied to quantify the residual damage in processed wafers, such as ion implanted ones [60-61]. This can be performed by analysing the normalised intensity $I_n=(I_o-I)/I_o$, where I is the intensity of the Raman band measured in the implanted layer and I_o is the intensity of the Raman band measured in a virgin non-processed sample. For a low degree of damage, I is very similar to I_o and I_n is close to 0. As damage increases, I decreases and I_n tends to the maximum value of 1. This gives a 100% damage benchmark, which corresponds to the damage level for which full amorphization of the implanted layer occurs. In this case, all the crystalline modes vanish from the spectrum, and I becomes 0. This method allows the degradation of the crystalline structure to be followed. It can also be used to optimize the annealing process after ion implantation in order to eliminate the induced damage.

However, the intensity of the Raman line can be affected by possible dispersion of light by dust particles in the air, as well as on the measuring surface and mirrors. The environmental temperature will affect the Raman intensity also. Fig. 4.9 is the GaN E_2 Raman band intensity mapping in an area of 31 μm x 10.1 μm. As before the laser scanned the X axis from left to right, then scanned along the Y axis from top to bottom. Fig. 4.9 shows that the GaN E_2 Raman band intensity decreases gradually from top to bottom of the sample. This is caused by the ambient temperature change when the measurement is performed. It is difficult to establish a relationship between the sample structure and the Raman band intensity from the results of Fig. 4.9. It is not easy to calibrate the Raman band intensity vibration due to environmental temperature changes, so tight environmental temperature control is necessary if such information is wanted.

The quantitative analysis of the band intensities related to the crystalline and amorphous phases gives the crystalline fraction in partially amorphous systems [62].
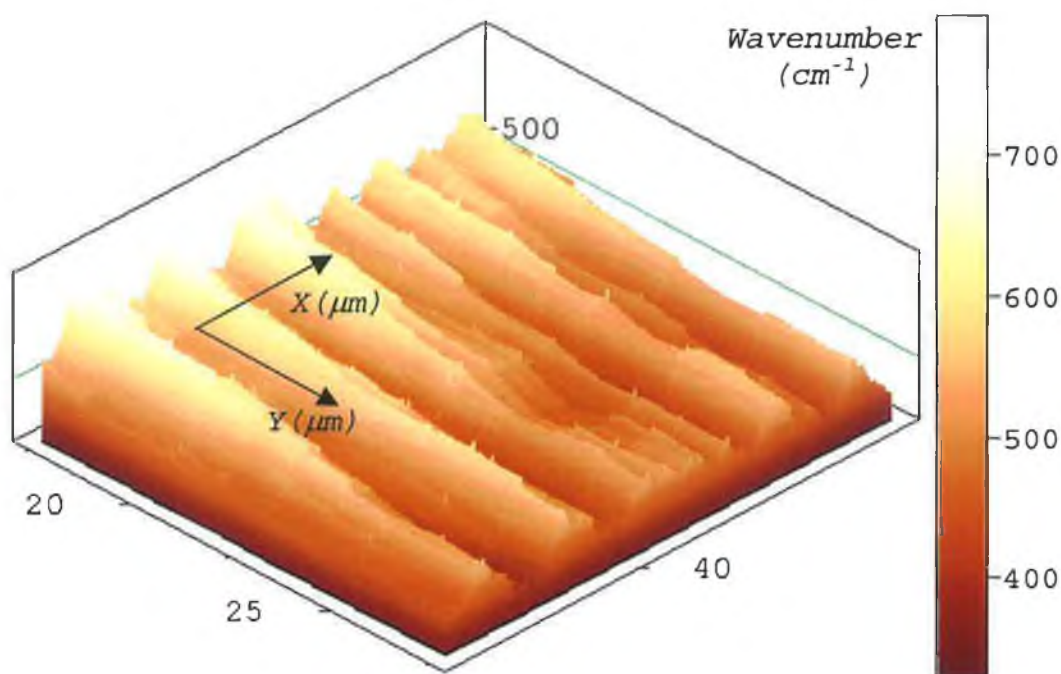
Figure 4.9 GaN E_2 Raman band ($\approx$568 cm^{-1}) intensity mapping in an area of 31μm x 10.1μm on the Epitaxial lateral Overgrown epilayer.

This technique is also useful to the research and manufacturing of glass-ceramic [63].

Besides the information listed above, local crystallographic orientation on semiconductor layers [64-67], free electrical charge carrier (electrons, holes) concentrations and the carrier mobility in semiconductors, etc. can also be measured [67-69] with the Raman technique.

Furthermore, Raman spectroscopy is also an efficient technique for other industries, for example, the pharmaceutical manufacturers [70]. Rapid, high throughput assessment of the composition, structure and uniformity of active ingredient distribution in drug tablet formulations is of great interest to the pharmaceutical industry. Understanding these parameters is critical to tablet quality monitoring and control. Typical analytical strategies for performing tablet assays often involve invasive sample preparation procedures, including tablet crushing, dissolution and chromatographic separation of active ingredients from excipients. Where tablet content uniformity must be measured, invasive sample staining procedures are often required to generate image contrast between active ingredients and excipients. Active ingredient distribution can then be visualized using optical

microscopy, for example. While traditional analytical strategies are effective, they are labour intensive due to the extensive sample preparation required and the techniques are applied to only a very limited number of tablets. Raman chemical imaging is an effective high throughput screening tool for the analysis of pharmaceutical tablet content uniformity. Analysis is performed without sample preparation, and characterization of tablets *in situ* is feasible, even in manufacturing environments as a quality monitoring tool. Similarly micro-Raman spectroscopy can be used to detect the contaminants in integrated circuits [71].

References

1. G.E. Moore, Proc. IEEE Int. Electropn Devices Meeting, p. 11 (1975).

2. T. Iida, T. Itoh, D. Noguchi, Y. Takanashi, Y. Takano, Y. Kanda, J. Appl. Phys. **89**, 2109 (2001).

3. P. Ramvall, Y. Aoyagi, A. Kuramata, P. Hacke, K. Horino, Appl. Phys. Lett. **74**, 3866 (1999).

4. G. Dilliway, PhD Thesis, University of Southampton, 2002

5. W.M. Chen, G.D.M. Dilliway, P.J. McNally, T. Tuomi, A.F.W. Willoughby, J. Bonar, J. Mater. Sci. - Mater. Electron, **14**, 455 (2003).

6. M.T. Currie, C.W. Leitz, T.A. Langdo, G. Taraschi, E.A. Fitzgerald, D.A. Antoniadis, J. Vac. Sci. Technol. B, **19**, 2268 (2001) and references therein.

7. S.B. Samavedam, W.J. Taylor, J.M. Grant, J.A. Smith, P.J. Tobin, A. Dip, A.M. Phillips, R. Liu, J. Vac. Sci. Technol. B, **17**, 1424 (1999).

8. S. Chen, T.V. Baughn, Z.J. Yao, C.L. Goldsmith, J. Microelectromech. Syst. **11**, 309 (2002).

9. L.Y. Lin, E.L. Goldstein, IEEE J. Select. Topics Quantum Electron. **8**, 163 (2002).

10. Nam-Trung Nguyen, Xiaoyang Huang, To Kok Chuan, J. Fluids Eng. - Transactions of the ASME, **124**, 384 (2002).

11. I. De Wolf, Semicond. Sci. Technol. **11**, 139 (1996), and reference therein.

12. J. Lu, D. Retraint. J. Strain Anal. Eng. Des. **33**, 127 (1998).

13. D. Buttard, D. Bellet, G. Dolino, J. Appl. Phys. **79**, 8060 (1996).

14. D. Mitchell, Y. Guo, V. Sarihan. IEEE Trans. Comp. Packag. Technol., **24**, 667 (2001).

15. A. Armigliato, R. Balboni, A. Benedetti, S. Frabboni, A. Tixier, J. Vanhellemont J. Phys. III, **7**, 2375 (1997).

16. J. Yuan, J.W. Corbett, S.N. Voronkov, I.V. Verner, Radiat Eff. Defects Solids, **125**, 275 (1993).

17. T. Okuyama, M. Nakayama, Y. Tomokiyo, O. Van der Biest, Microsc. Microanal. **8**, 11 (2002).

18. J. Demarest, R. Hull, K.T. Schonenberg, K.G.F. Janssens, Appl. Phys. Lett. **77**, 412 (2000).

19. I. De Wolf, G. Groeseneken, H.E. Maes, M. Bolt, K. Barla, A. Reader, P.J. McNally. ISTFA '98. Proceedings of the 24th International Symposium for Testing and Failure Analysis. ASM Int. 1998, pp.11-15. Materials Park, OH, USA.

20. http://stream.bo.cnr.it/pdocs/D06_IST10341-IM-RP001.doc, and reference therein.

21. Kai F. Dombrowski, PhD thesis, Brandenburgischen Technischen Universität Cottbus, 2000.

22. S. Jimenez-Sandoval, Microelectron. J. **31**, 419 (2000).

23. S. Narayanan, S.R. Kalidindi, L.S. Schadler, J. Appl. Phys. **82**, 2595 (1997).

24. K. Pinardia, S.C. Jain, M. Willander, A. Atkinson, H.E. Maes, R. Van Overstraeten, J. Appl. Phys. **84**, 2507 (1998).

25. I. De Wolf, H.E. Maes, S.K. Jones, J. Appl. Phys. **79**, 7148 (1996).

26. I. De Wolf, E. Anastassakis, Addendum: 'Stress measurements in silicon devices through Raman spectroscopy: Bridging the gap between theory and experiment' [J. Appl. Phys. **79**, 7148 (1996)]. J. Appl. Phys. **85**, 7484 (1999).

27. Sidney Perkowitz, Optical characterization of semiconductors : infrared, raman, and photoluminescence spectroscopy, Academic Press: London; San Diego, 1993.

28. C.V. Raman, Ind. J. Phys. **2**, 387 (1928).

29. R. Loudon, Adv. Phys. **13**, 423(1964); erratum ibid. **14**, 621 (1965).

30. G.D. Pazionis, H. Tang, I.P. Herman. IEEE J. Quantum Electron. **25**, 976 (1989).

31. H. Brugger, P.W. Epperlein, Appl. Phys. Lett., **56**, 1049 (1990).

32. E. Anastassakis, A. Pinczuk, E. Burstein, F.H. Pollak, M. Cardona, Solid State Commun. **8**, 133 (1970).

33. K. Brunner, G. Abstreiter, B.O. Kolbesen and H.W. Meul, Appl. Surf. Science **39**, 116 (1989).

34. M. Chandrasesekhar, J.B. Renucci, M. Cardona, Phys. Rev. **17**, 1623 (1978).

35. E. Anastassakis, A. Cantarero, M. Cardona, Phys. Rev. **41**, 7529 (1990).

36. O.H. Nielsen, R.M. Martin, Phys. Rev. Lett. **50**, 697 (1983).

37. O.H. Nielsen, R.M. Martin, Phys. Rev. B **32**, 3792 (1985).

38. M. Methfessel, C.O. Rodriguez, O.K. Andersen, Phys. Rev. B **40**, 2009 (1989).

39. C. Kisielowski, J. Kruger, S. Ruvimov, T. Suski, J.W. Ager III, E. Jones, Z. Liliental-Weber, M. Rubin, E.R. Weber, M.D. Bremser, R.F. Davis, Phys. Rev. B **54**, 17745 (1996).

40. P. Perlin, C. Jauberthie-Carillon, J.P. Itie, A. San Miguel, I. Grzegory, A. Polian, Phys. Rev. B **45**, 83 (1992).

41. V.Yu. Davydov, N.S. Averkiev, I.N. Goncharuk, D.K. Nelson, I.P. Nikitina, A.S. Polkovnikov, A.N. Smirnov, M.A. Jacobson, O.K. Semchinova, J. Appl. Phys. **82**, 5097 (1997).

42. M.A. Benitez, L. Fonseca, J. Esteve, M.S. Benrakkad, J.R. Morante, J. Samitier, J.A. Schweitz, Sens. Actuators, A**54**, 718 (1996)

43. J.R. Morante, J. Samitier, M.S. Benrakkad, Microelectron. J. **28**, 433 (1997).

44. M. Furtsch, M. Offenberg, A. Vila, A. Cornet, J.R.Morante, Thin Solid Films, **296**, 177 (1997)

45. European Commission, Directorate General Science, Research and Development, EUR 18595, "Raman and Luminescence Spectroscopy for Microelectronics".

46. W.M. Chen, P.J. McNally, K. Jacobs, T. Tuomi, A.N. Danilewsky, Z.R. Zytkiewicz, D. Lowney, J. Kanatharana, L. Knuuttila, J. Riikonen, J. Cryst. Growth, **243**, 94 (2002).

47. W.M. Chen, P.J. McNally, K. Jacobs, T. Tuomi, A.N. Danilewsky, D. Lowney, J. Kanatharana, L. Knuuttila, J. Riikonen, Mat. Res. Soc. Symp. Proc., **693**, 141 (2002).

48. W.M. Chen, P.J. McNally, K. Jacobs, T. Tuomi, J. Kanatharana, D. Lowney, L. Knuuttila, J. Riikonen, J. Toivonen, J. Mater. Sci. - Mater. Electron, **14**, 283 (2003).

49. J. Kanatharana, J. J. Pérez-Camacho, T. Buckley, P. J. McNally, T. Tuomi, J. Riikonen, A. N. Danilewsky, M. O'Hare, D. Lowney, W. Chen, R. Rantamäki, L. Knuuttila, Semicond. Sci. Technol. **17**, 1255 (2002).

50. E. Hecht, *Optics*, 2nd ed., Addison-Wesley Publishing Company, New York, 1987.

51. The internet journal of vibrational spectroscopy, 2(4). (http://www.ijvs.com/volume2/edition4/section1.htm)

52. D.E. Aspnes, A.A. Studna, Phys. Rev. B **27**, 985 (1983).

53. J-I. Takahashi, T. Makino, J. Appl. Phys. **63**, 87 (1988).

54. G. Abstreiter, K. Eberl, E. Friess, U. Menczigar, W. Wegscheider, R. Zachai, "Phonons and optical properties of Si/Ge Superlattices" in "Spectroscopy of Semiconductor Microstructures" (G. Fasol, A. Fasolino, P. Lugli), Plenum Press, New York, 1989, p. 165.

55. J.C. Tsang, P.M. Mooney, F. Dacol and J.O. Chu, J. Appl. Phys. **75**, 8098 (1994), and reference therein.

56. M.I. Alonso, K. Winer, Phys. Rev. B **39**, 10056 (1989).

57. C.H. Perry, L. Feng, F. Namavar, Solid State Commun. **88**, 613 (1993).

58. M. Kubo, M. Mannoh, T. Narusawa. J. Appl. Phys. **66**, 3767 (1989).

59. J. Macia, E. Martin, A. Perez-Rodriguez, J. Jimenez, J.R. Morante, B. Aspar, J. Margail. J. Appl. Phys. **82**, 3730 (1997).

60. R. Heliou, J.L. Berbner, S. Roorda. Semicond. Sci. Technol. **16**, 836 (2001).

61. A. Perez-Rodriguez, O. Gonzalez-Varona, L. Calvo-Barrio, J.R. Morante, H. Wirth, D. Panknin, W. Skorupa. Trans Tech Publications. Mater. Sci. Forum, **258-263**, 727 (1997).

62. A.T.Voutsas, M.K. Hatalis, J. Boyce, A.Chiang, J. Appl. Phys. **78**, 6999 (1995).

63. Measurement Techniques for Glass, Edited by Nanjin Glass-fibre Research Institute, Chinese Architecture Technology Press, 1987.

64. J. Sapriel, J. Chavignon, F. Alexandre, P. De Souza, and A.C. Papadopoulo, Inst. Phys. Conf. Ser., **91**, 371 (1988).

65. G. Kolb, T. Salbert, G. Abstreiter, J. Appl. Phys. **69**, 3387 (1991).

66. K. Mizoguchi, and S. Nakashima, J. Appl. Phys., **65**, 2583 (1991).

67. S. Nakashima, Raman microprobe study of semiconductors, Light Scattering in Semiconductor Structures and Superlattices (D.J. Lockwood, and J.F. Young, eds.), Plenum Press, New York, 1991, p. 291.

68. S. Nakashima, H. Yugami, A. Fujii, M. Hangyo and H. Yamanaka, J. Appl. Phys., **64**, 3067 (1988).

69. M. Herms, G. Irmer, J. Monecke, and O. Oettel, J. Appl. Phys., **71**, 432 (1992).

70. I. Nabiev, I. Chourpa, M. Manfait. J. Raman Spectrosc. **25**, 13 (1994).

71. R.Z. Muggli, M.E. Andersen. Solid State Technology, **28**, 287 (1985).

5 Micro-Raman stress measurement results

5.1 Stress distribution in ELO GaN

Up to now the crystal structure, defect distribution and the effects of process steps on the crystal structure of the ELO GaN have been studied extensively [1-4]. Unfortunately, relatively little research has been carried out on the stress distribution in ELO GaN epilayers [5-6], despite the fact that stress has important effects on the performance and reliability of devices [7]. The aim of this work was to study the stress distribution in the ELO GaN layers on sapphire by the use of the micro-Raman spectroscopy technique.

Each spectrum in this study was obtained with 3 accumulation times to improve signal-to noise ratios. The GaN E_2 (high, it will be simply referred to as E_2 later) Raman peak positions presented in this paper were obtained from the original experimental spectrum with a Gauss/Lorentz fitting function using the software provided by the equipment manufacturer.

5.1.1 ELO GaN stress measurement results and discussion

Fig. 5.1 shows a typical two dimensional GaN E_2 Raman peak position mapping of the sample in a rectangular area of 36.1×20 μm from region c (i.e. fill factor: 0.571, refer to Section 3.2.5) of the ELO GaN epilayer. This mapping was abstracted from more than 7000 original GaN Raman spectra measured in this area. The X axis of Fig. 5.1 is set perpendicular to the SiO_2 stripe direction, and the Y axis is parallel to the SiO_2 stripe direction. It can be seen from Fig. 5.1 that the GaN E_2 Raman peak position shift in this ELO GaN sample exhibits a regular wave-like shape, which means the stress in the ELO GaN changes regularly in accordance with the periodicity of the structure along the X axis. The wave-like valleys (i.e. lower stress region) are usually located over midpoints of the SiO_2 stripes (i.e. at the regions of adjacent wing coalescence, which are indicated with arrows in Fig. 5.1), and the wave-like peaks (i.e. higher stress region) are usually located at the window positions. Each spectrum from the measured region exhibits a GaN E_2 Raman peak higher than 568 cm^{-1}. This indicates that the ELO GaN epilayer is under a
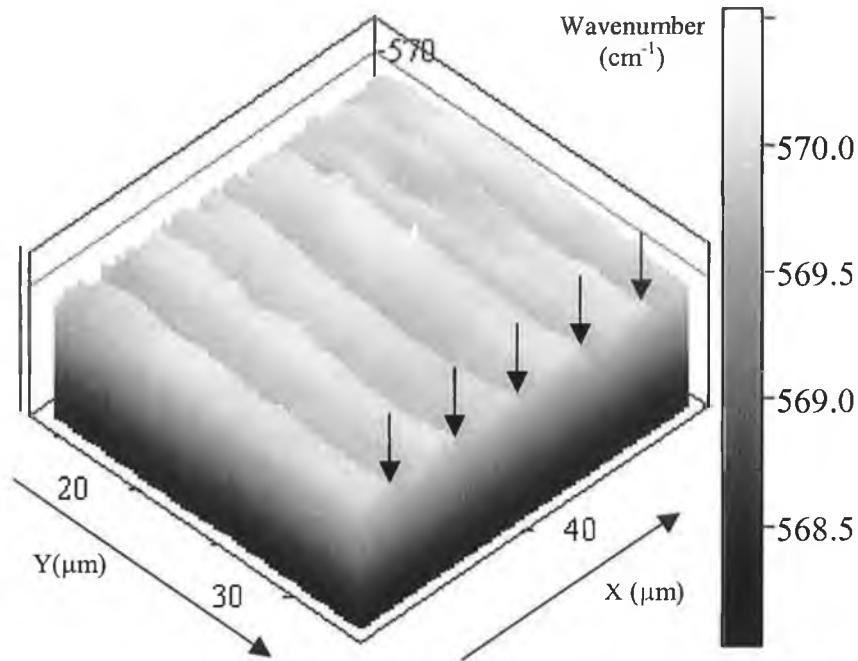
Figure 5.1 GaN E_2 Raman peak mapping of the ELO GaN epilayer in region c obtained with micro-Raman spectroscopy. The regions where the ELO wings coalesce are indicated by the arrows.

compressive stress [8-9], as is expected from the difference of thermal expansion coefficients of GaN and the underlying sapphire substrate. The statistical average GaN E_2 Raman peak position of this region is 569.89 cm^{-1}, so an average biaxial compressive stress of 450 MPa exists in the epilayer (calculated using equation (4.18)).

Fig. 5.2 shows a typical stress distribution measured along the X axis. The window and coalesced regions are also indicated in Fig. 5.2. The wave-shaped stress distribution along the X direction is very clear. The GaN E_2 Raman peak at the coalesced regions usually shifts to a value about 0.25 cm^{-1} lower than the average position for this sample. This implies the existence of a lower compressive stress by about 60 MPa at the coalesced region compared to the average stress in the ELO GaN epilayer. An average compressive stress difference of about 120 MPa between the window and coalesced regions exists in the studied samples.

Holtz *et al.* [10] found that the epitaxial lateral overgrown region showed a slightly lower compressive stress compared to the window region. In their research
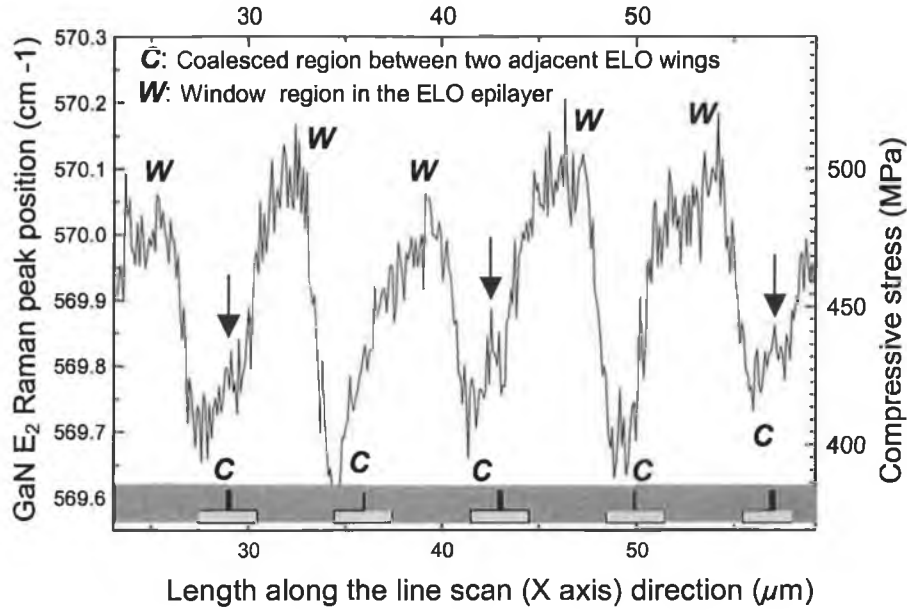
Figure 5.2 GaN E_2 Raman peak shift and compressive stress distribution along the line perpendicular to the SiO_2 mask stripe direction in region *c*. The cross sectional view of the ELO GaN epilayer is schematically shown at the bottom of the diagram. Voids at the coalesced regions, i.e. at the midpoints of the SiO_2 mask stripes, are schematically indicated with the black short bars.

isolated hexagonal GaN islands were grown by selective area overgrowth. The compressive stress in the overgrown region relaxed because of the free overgrown edge. The situation for our sample is different, as continuous ELO GaN epilayer was formed. However voids usually exist in the two coalesced wing regions [1, 11], and they are close to the mask surface at the front where two adjacent wings merge. These voids are generated due to the limited flow of reactants along the side walls of merging layers. Moreover, it has been shown that the creation of voids is easier if two merging wings are tilted in opposite directions [1, 12-13].

As indicated in Section 3.2.6, white beam synchrotron X-ray topography measurements of the sample indicated that the crystal planes of the overgrown wings tilted relative to the crystal planes in the window regions [2-3]. Thus, generation of voids at the coalescence fronts cannot be avoided in our sample. It is quite possible that the lower regions of the ELO GaN epilayer in this sample are actually partially separated from each other at the coalesced areas by these voids, despite the fact that a

continuous ELO GaN epilayer is formed at the upper part. Similar to the result of Holtz *et al* [10], in the area around the voids, i.e. the coalesced wing regions, the compressive stress of the epilayer will be partially relaxed. Consequently, a lower compressive stress in the coalesced regions was observed in our sample. Finite element analysis by Benyoucef *et al*. [14] showed that the compressive stress relaxed faster in the wing area compared to the window region. Their micro-Raman stress measurement result in MOVPE grown ELO GaN on sapphire substrate confirmed this trend [6, 14]. In agreement with the data shown in Fig. 5.1 and Fig. 5.2, they have found a maximum of stress located in the GaN grown vertically from the seeding window and significant stress relaxation in the wing areas. Similar behaviour has been also found in thick ELO GaN layers grown on sapphire by hydride vapour phase epitaxy [15-16].

Occasionally a small compressive stress increase is observed near the coalescence front for adjacent wings as indicated with arrows in Fig. 5.2. A similar finding was reported in [6, 14] and the presence of voids at the coalescence region was again thought as the local source of this increased compressive stress. It has been shown by finite element analysis that compressive stress arises in GaN on sapphire ELO structures close to the tip of the void at the coalescence boundary [14]. Therefore, it is reasonable to attribute the local compressive stress increase at the midpoints of the SiO_2 stripes (Fig. 5.2) to void induced stress. It is important to point out here that the magnitude of stress generated by the voids has been found to increase with their size [14]. The wing tilt and size of void at the seam lines is unlikely to be identical across the entire ELO GaN sample. Most probably, the appearance of areas with a local increase of compressive stress on the micro-Raman map in Fig. 5.1 is consistent with a void distribution that differs from region to region. If the voids are too small the stress they induce is below the sensitivity of our measurements and they are not visible on the map.

5.1.2 Effects of the Epitaxial Lateral Overgrowth on the GaN epilayer stress

Fig. 5.3 shows the typical GaN E_2 Raman peak position mapping in region *b* (i.e. fill factor: 0.5) similar to Fig. 5.1. Also, the one dimensional GaN E_2 Raman peak position shift along the X axis is shown in Fig. 5.4. The length of this scanned
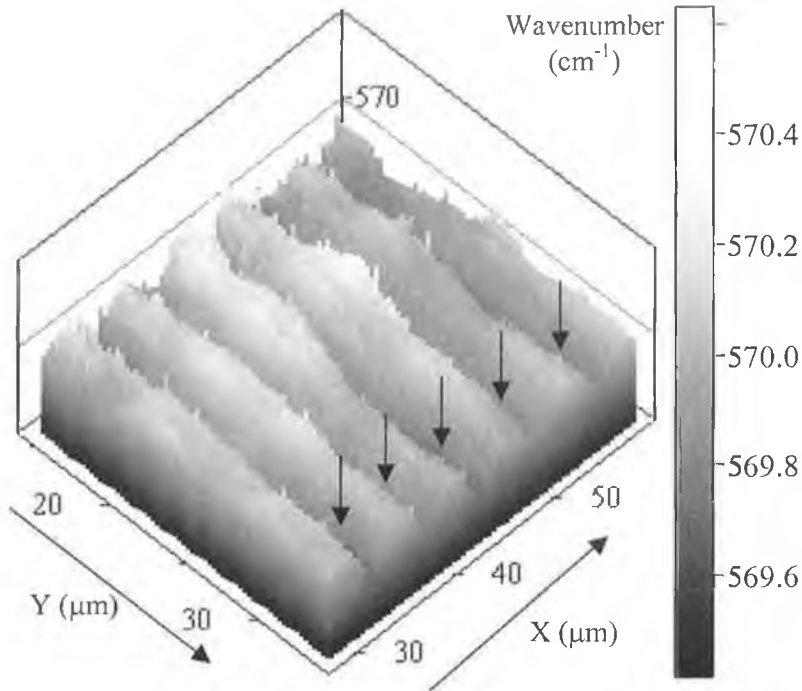
Figure 5.3 GaN E₂ Raman peak mapping of the ELO GaN epilayer in region *b* obtained with micro-Raman spectroscopy. The regions where the ELO wings coalesce are indicated by the arrows.
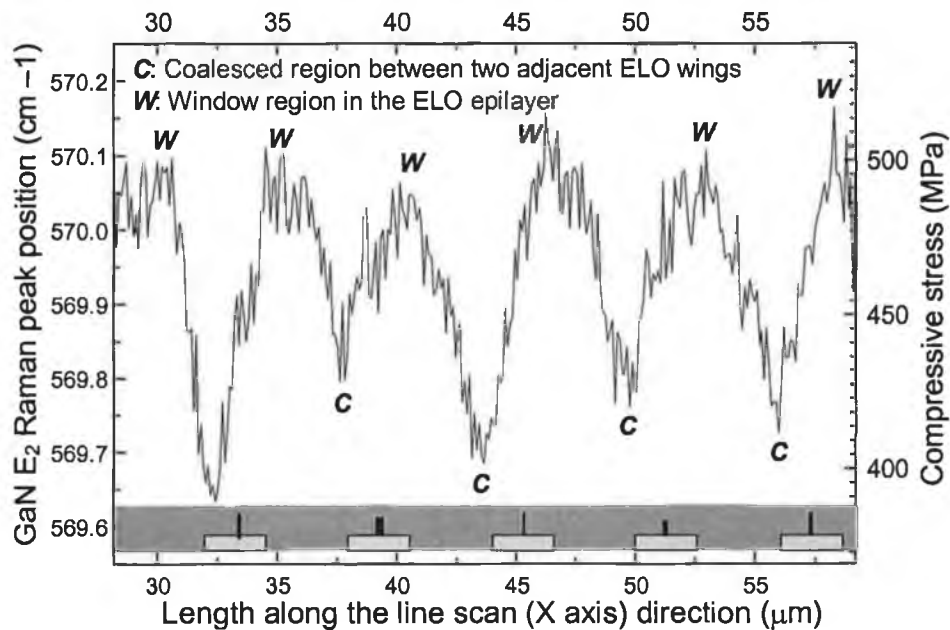

Figure 5.4 GaN E₂ Raman peak position shift and stress distribution of the ELO GaN epilayer along the line perpendicular to the SiO₂ stripes (X axis) in region *b*. The cross sectional view of the ELO GaN epilayer is schematically shown at the bottom of the diagram. Voids at the coalesced regions, i.e. at the midpoints of the SiO₂ mask stripes, are schematically indicated with the black short bars.

line for Fig. 5.4 was 31 μm and it consists of 310 individual spectra along this line scan. The window and the coalesced regions of the ELO GaN epilayer are also indicated in Fig. 5.4. Again both Fig. 5.3 and Fig. 5.4 indicate the wavy stress distribution in region b, but in this region, the measured average GaN E_2 Raman peak position across the scanned area is 569.93 cm^{-1}. The average compressive stress in this ELO GaN epilayer is calculated to be 460 MPa, which is very close to the average stress in region c, 450 MPa. The stress difference between the coalesced regions and the window regions is also similar to that in region c, being about 120 MPa.

For comparison, the average compressive stress in the Non-ELO GaN epilayer, i.e. region a, of the sample is measured to be about 350 MPa. The wavy stress distribution does not appear in this region. A GaN E_2 Raman peak mapping at the boundary area of region a and region b is shown in Fig. 5.5. Wavy stress distributions only appear in the ELO epilayer region. This clearly shows that the
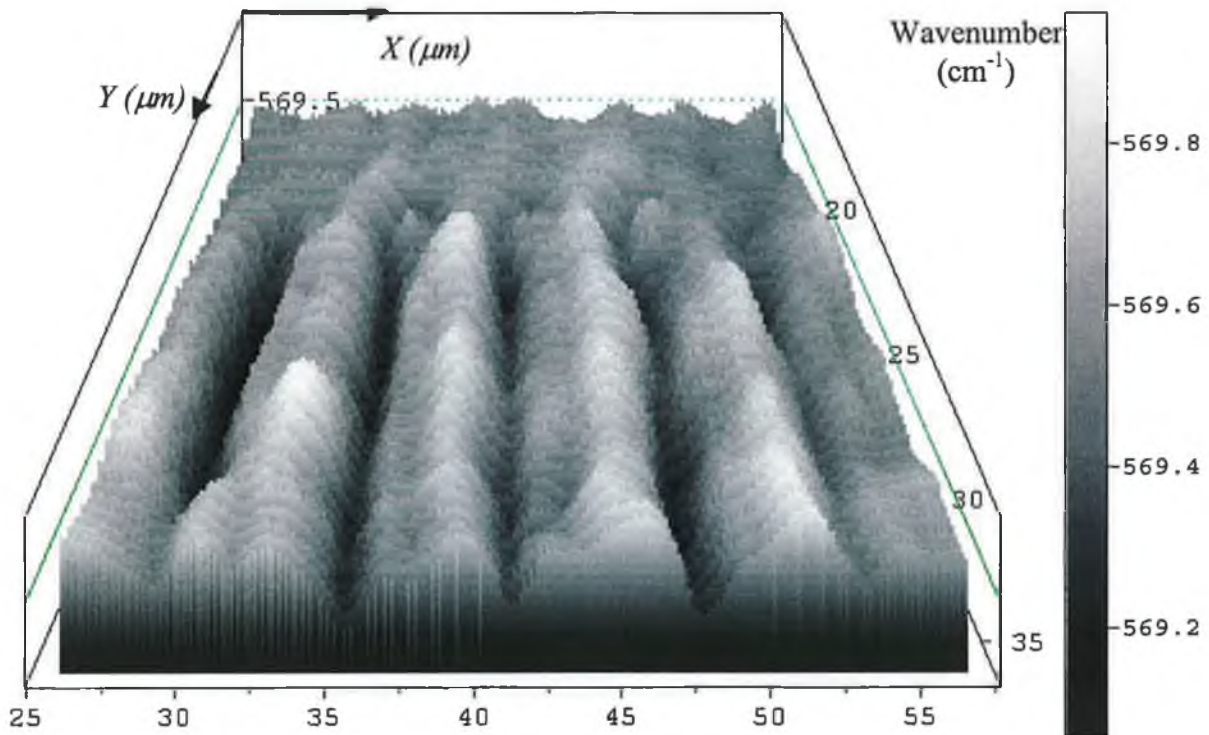

Figure 5.5 GaN E_2 Raman peak mapping at the boundary area of region a (upper part of this mapping, non-ELO epilayer) and region b (lower part, ELO epilayer with a fill factor of 0.5).

126

presence of the SiO₂ mask in our ELO process increases the residual compressive stress in the GaN epilayer. There are many possible reasons for this, such as the thermal expansion coefficients of materials, moisture level and the deposition technique of the film, dislocation density, etc. can affect the stress of the epilayer.

5.1.3 Correlation between the micro-Raman stress measurement and X-ray topography results

Discussions about the "fuzzy" lattice misorientational features in the ELO GaN topograph in Section 3.2.6 are based on the assumption that the interplanar spacing, d_{hkl}, of the lattice planes remains unchanged or is small enough in the studied sample. According to equations (3.9) and (3.10), the "fuzzy" feature in the topographs (as shown in Figs. 3.11-3.13) and the two side peaks in the X-ray rocking curves (Fig. 3.14) can also be caused in principle by an interplanar spacing change as a result of the stress which exists in the ELO GaN epilayer. In this case, as the side peaks appear on both sides of the normal peak in the rocking curves, or for the topographs, the "fuzzy" feature appears above and below the normal GaN topograph position at the same time (see Figs. 3.11 and 3.13. For the large area topographs, only the lower fuzzy feature is shown in Fig. 3.12 due to the limitation of the minimum image magnification of the CCD camera used in this study). Thus the interplanar spacing of the reflecting GaN crystal planes increases in some parts of the sample, and decreases in other parts of the same sample, i.e. both tensile and compressive stress are expected to exist in the GaN epilayer. As pointed out previously, the micro-Raman spectroscopy stress measurement results showed [17] that a compressive stress with the value of about 450~460 MPa exists in the epilayer in the ELO GaN epilayer. Despite the wavy stress field was observed in this study, no tensile stress was detected in this sample.

The 488 nm Ar⁺ laser light source was used as the exciting source for the µRS measurement for this ELO GaN sample. The penetration depth of the light in GaN is more than 2 µm [18], which is almost equal to the ELO GaN layer thickness, thus the average stress information over the whole thickness of the ELO GaN epilayer is obtained with the µRS technique. The topographs and rocking curves also show the overall epilayer structures along the whole thickness of the sample, and consequently

it is reasonable to conclude that the "fuzzy" features in the topographs and the side peaks of the rocking curves shown previously are caused by the GaN crystal misorientation rather than the epilayer stress.

5.2 Stress in the $Si_{1-x}Ge_x$ virtual substrate and the device cap layer

5.2.1 Significance of $Si_{1-x}Ge_x$ virtual substrate and the strained Si device layer

Epitaxially grown lattice mismatched heterostructures are increasingly used for both microelectronic and optoelectronic applications. Silicon-germanium (Si-Ge) epitaxial heterostructures are becoming increasingly important for high frequency microelectronics applications. One option under serious consideration is that of using relaxed SiGe buffer layers, i.e. Si-Ge virtual substrates. They are compositionally graded layers, either linearly graded layers or stepped graded layers, designed to accommodate the lattice mismatch between the underlying Si substrate and the overlying active epilayers(s).

Since Si and Ge are completely miscible over the whole composition range, crystal properties such as bandgap and lattice constant can be varied continuously. For the $Si_{1-x}Ge_x$ alloys, Vegard's law is a reasonable approximation [19], the lattice parameter $\alpha_{Si_{1-x}Ge_x}$ of relaxed $Si_{1-x}Ge_x$ varies linearly with the Ge concentration, and can be expressed as [20]:

$$\alpha_{Si_{1-x}Ge_x} = (1-x)\alpha_{Si} + x\alpha_{Ge} \tag{5.1}$$

where α_{Si} and α_{Ge} are lattice parameters for crystal silicon and germanium respectively, x is the germanium concentration in the alloy, whose value lies in the range $0\% \leq x \leq 100\%$. Thus the lattice parameter of $Si_{1-x}Ge_x$ can be adjusted by alternating the germanium concentration in the alloy. This is lattice constant engineering for unstrained layer overgrowth.

Some devices require a virtual substrate with a defined lattice constant for unstrained layer overgrowth. For example, the integration of GaAs-based epitaxial devices with Si technology can be possible via a $Si_{1-x}Ge_x$ virtual substrate graded to pure Ge, as the lattice constants of Ge and GaAs have very close values [21].

Many other devices call for a virtual substrate with an adjustable lattice constant in order to provide the appropriate strain required to achieve specific properties, such as high speed, etc. By engineering the lattice mismatch between the $Si_{1-x}Ge_x$ layer and the Si substrate, as well as the lattice mismatch between individual $Si_{1-x}Ge_x$ layers of different compositions, a multitude of new electronic properties and advanced devices based on bandgap and strain engineering have been enabled. For example, when thin, fully strained, Si is grown over the relaxed $Si_{1-x}Ge_x$ capping

layer, the electron and hole mobility of Si improves because of the effective mass reduction and/or the band structure modification by the in-plane tensile strain [22-23]. This structure enables improvements in circuit speeds at lower prices than III-V's used so far, and at high levels of integration, and have led to increased interest in silicon-based heterojunction field effect transistors using conventional Si-processing technology [24]. However if the strain in the device layers relaxes through the introduction of misfit dislocations, the carrier mobility of the resulting devices will decrease due to the strain loss [22] and scattering effects by the misfit dislocations [22-23, 25]. In addition, the leakage currents of the devices will also increase by the introduction of misfit and threading dislocations in the device layer [23, 26]. Thus it is important to preserve the strain regime and epilayer quality in the Si device layers.

Virtual substrates can also be used to confine holes in Ge and SiGe layers under biaxial compression [21].

Simulation results indicate that devices incorporating Si and SiGe layers grown on $Si_{1-x}Gi_x$ virtual substrates offer noteworthy advantages in performance [27]. They are used for high electron mobility transistors, metal-oxide-semiconductor field effect transistors and for the integration of III-V devices on Si [28-29].

High quality strain-relaxed $Si_{1-x}Ge_x$ virtual substrates assist in the prevention of the development of misfit and threading dislocations in the overlying heterostructures which can impact adversely on the active device regions. They offer a new degree of freedom in strain and bandstructure engineering for devices via lattice mismatched templates for strained layer overgrowth.

As the lattice constant of Ge is 4.2% larger than that of Si [20], a strain relaxed SiGe buffer layer can only be achieved with the creation of misfit dislocations, and some of these misfit dislocations will penetrate towards the sample surface as threading dislocations [27]. The high threading dislocation densities in the relaxed $Si_{1-x}Ge_x$ virtual substrates may be avoided by using a series of interfaces with low mismatch and increasing the Ge concentration in steps, or linearly with a relatively high growth temperature [24, 30]. Since the gradual increase of the lattice mismatch in the virtual substrate induces a misfit dislocation network distributed over the range of compositional grading, rather than being concentrated at the interface with the Si substrate, the threading dislocation density is reduced by three orders of magnitude. Typically, the threading dislocation densities drop from 10^8-10^{10} cm^{-2} for uniform SiGe layers on Si substrate to 10^5-10^6 cm^{-2} for virtual substrates [23-24]. However

high growth temperatures for the virtual substrate, which can lead to 3D growth and can result in a rough surface morphology [24], and which may affect lithography steps in subsequent device processing, are desired for a low threading dislocation density. Material scientists are trying to optimise the virtual substrate process to reduce this threading dislocation density to obtain high quality $Si_{1-x}Ge_x$ virtual substrates [21].

Research has shown that an incomplete strain relaxation in the underlying $Si_{1-x}Ge_x$ virtual substartes would induce strain relaxation in the Si device layers [23]. Thus, the ability to monitor the strain (stress) state of the Si device layer(s) and the underlying $Si_{1-x}Ge_x$ virtual substrate is essential for the development of Si - $Si_{1-x}Ge_x$ heterostructures and related devices.

As indicated in Section 3.2, besides micro-Raman spectroscopy [5, 17], high resolution X-ray diffraction [24, 31-33] and TEM [34-37] methods can also be used for the stress characterization. In some studies, the selective etching method was used as an indirect method to infer the fully strained state of the Si channel [22] via the absence of misfit dislocations at the interface. However this method is destructive for the studied sample and provides only indirect evidence of the stress.

In this study, the high resolution micro-Raman spectroscopy method was used to study the stress both in the Si device layer(s) and the underlying $Si_{1-x}Ge_x$ layers[5].
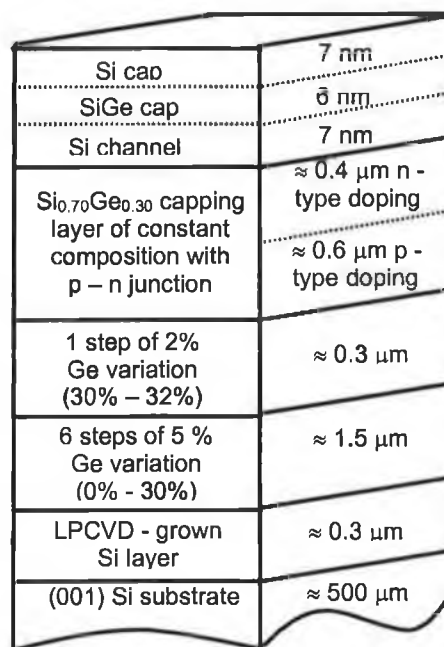
5.2.2 $Si_{1-x}Ge_x$ virtual substrate and the overlying Si device layer structure and preparation

The analysed heterostructure was grown using low pressure chemical vapour deposition (LPCVD) in the University of Southampton, U.K. The LPCVD system used is of the cold-wall type (using water for cooling), thus producing the least amount of chamber coating. The sample substrates are heated by a 300 mm diameter graphite meander mounted on the top flange of the chamber. In order to minimise possible carbon contamination during growth, every new heating element is coated with silicon at high temperature before any device layers are grown. During growth, the substrates are continuously rotated in order to ensure uniformity. Epitaxial growth can be carried out in the temperature range from 1000°C down to less than 700°C. The sample studied in this study was grown at 750 °C. The LPCVD system for growing this sample uses gaseous sources, which can be replenished without

needing to disturb the vacuum in the growth chamber. The lowest base pressure in this LPCVD machine is 10^{-3} Torr. The LPCVD technique used provides control over both the growth pressure and the source gas flow, thus enabling additional control over the growth rates. The growth pressure values can be varied between 0.03 - 1 Torr and the heterostructures for this study were grown at 0.5 Torr.

The growth sequence for this SiGe virtual substrate-based heterostructures is as follows:

- *Ex-situ* chemical clean (standard RCA), which leaves the wafers oxide terminated;
- Very brief dip in dilute $HF:H_2O$ (1:100), which thins the 'RCA' oxide, thus allowing its reliable desorption at lower temperatures;
- Load wafer into the growth chamber through the load lock;
- Purge the chamber with hydrogen, at 900 °C, to thermally desorb the 'RCA' oxide that covers the wafer surface;
- LPCVD of the SiGe heterostructures using as gaseous sources: silane (SiH_4) and germane (GeH_4); for the dopants: diborane (B_2H_6) for p-type, and phosphine (PH_3) for n-type; and as carrier gas, hydrogen;

Figure 5.5 Schematic of the sample structure.

- Purge the growth chamber with hydrogen again at the end of the process, before transferring the wafer to the load lock;
- Unload the wafer ready to be analysed and further processed.

More details about the sample preparation can be found in reference [21]. The sample structures are shown in Fig. 5.5. Both a 488 nm wavelength visible Ar$^+$ laser and a 325 nm HeCd UV laser were used as excitation sources for the measurements, which were performed at room temperature [5].

5.2.3 Stress in the device layers and the underlying Si$_{1-x}$Ge$_x$ virtual substrate

Fig. 5.6 is a typical Raman spectrum obtained from the sample with the 488 nm Ar$^+$ laser source. The standard strain free Si Raman spectrum with the 488 nm Ar$^+$
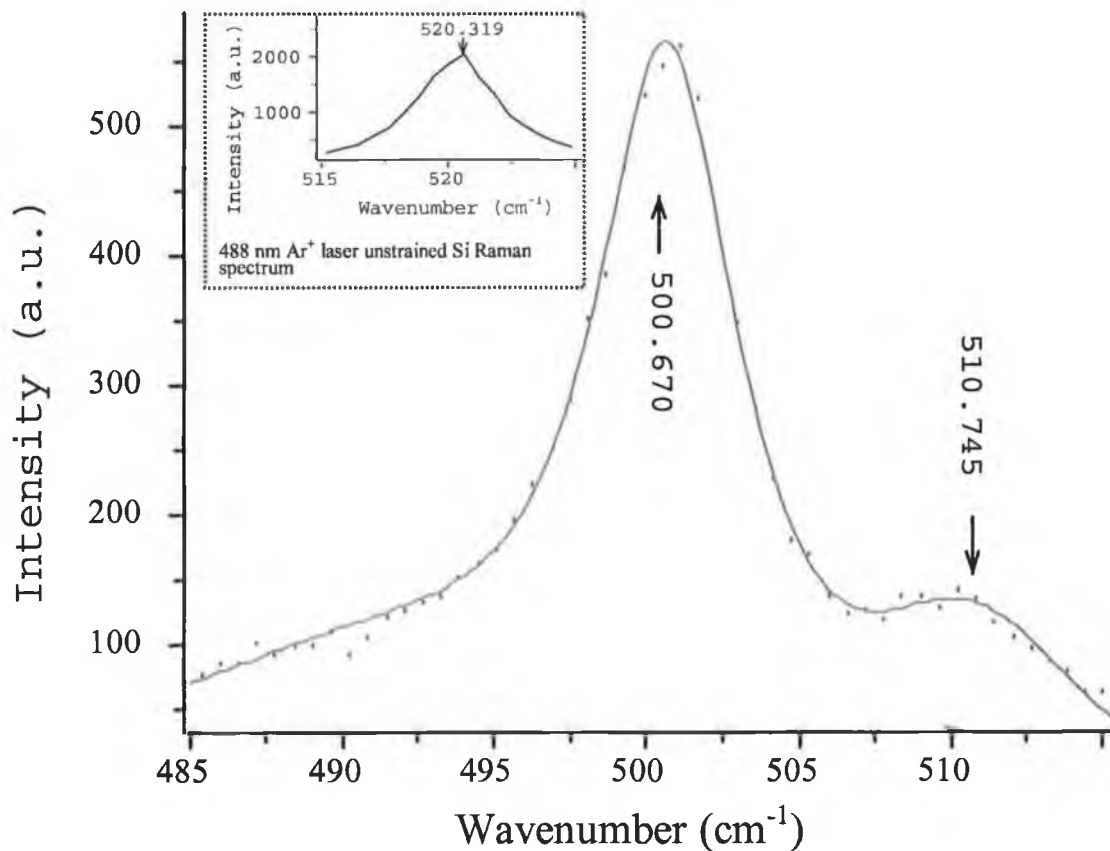

Figure 5.6 Typical Raman spectrum of the sample with the 488 nm Ar$^+$ laser. Dots are experimental results and solid line is software fitted curve with a Gauss/Lorentz function.

laser source is included in the inset of Fig. 5.6. Software fitting of the spectrum with the Gauss/Lorentz function indicates a strong peak located ~500.7 cm^{-1}, plus one weak peak located at ~ 510.7 cm^{-1} in the measured spectrum.

The penetration depth d_p of the laser in the measured sample is estimated according to (4.28). The calculated penetration depths for the 488 nm laser light in Si and Ge crystals are listed in Table 5.1. For $Si_{1-x}Ge_x$, the penetration depth depends on the composition and lies between those of Si and Ge. It can be estimated with the following equation [18]:

$$d_{p-SiGe} = (1-x)d_{p-Si} + xd_{p-Ge} \qquad\qquad (5.2)$$

For the 488 nm laser light, its penetration depth in $Si_{0.70}Ge_{0.30}$ is estimated to be 396 nm. Considering the penetration depth of the 488 nm laser light in different materials and the sample structure as indicated in Fig. 5.5, it can be concluded that the strong Raman peak at ~500.7 cm^{-1} in Fig. 5.6 is the Si-Si phonon mode of the $Si_{0.70}Ge_{0.30}$ capping layer. The weak Raman peak at ~510.7 cm^{-1} is the Si Raman signal of the Si cap and channel layers, which is supported by the UV laser micro-Raman measurement results, and will be explained later. As the penetration depth for the 488 nm laser light is much larger than the thickness of the top Si device layers, the Si Raman signal from these layers constitutes only a small part of the whole Raman signal presented in Fig. 5.6.

For $Si_{1-x}Ge_x$ alloys, the Si-Si phonon mode peak position depends both on the alloy composition and strain of the epilayer [18, 38-39]. The Ge content causes the Si-Si phonon mode peak position to shift from the strain free Si Raman peak position ($\Delta\omega_{Si-Si}$). For relaxed $Si_{1-x}Ge_x$ alloys it is reported to be $\Delta\omega_{Si-Si} = -68x$ [18]; $\Delta\omega_{Si-Si} =$

Table 5.1 Absorption coefficient (α) and penetration depth (d_p) in crystalline Si and Ge for 325 nm and 488 nm laser excitation sources

Crystal sample	Laser wavelength (nm)	Laser energy (eV)	$10^{-3}\alpha$ (cm^{-1})	d_p (nm)
Si	325	3.81	1235.18	9
	488	2.54	20.61	558
Ge	325	3.81	1159.28	10
	488	2.54	605.94	19

−69x [38] or $\Delta\omega_{Si-Si}$= −70x [39]. This means that a higher Ge content induces a downward shift of the Si-Si phonon mode peak position in Si$_{1-x}$Ge$_x$ alloys. In contrast, a compressive strain in the Si$_{1-x}$Ge$_x$ epilayer increases the Si-Si phonon mode peak position [18], i.e. decreases the measured $\Delta\omega_{Si-Si}$ value. In this study the Si-Si phonon mode peak position shift of the Si$_{0.70}$Ge$_{0.30}$ cap layer relative to the strain-free Si Raman peak position is 21.32 cm^{-1}, which is the average result of more than 400 spectra obtained for an area scan with the 488 nm wavelength laser. This value is very close to the expected Si-Si phonon mode peak position shift for a relaxed Si$_{0.70}$Ge$_{0.30}$ epilayer using the relation: $\Delta\omega_{Si-Si}$= −70x [39]. Thus, it is reasonable to conclude that the Si$_{0.70}$Ge$_{0.30}$ virtual substrate capping layer and the Si$_{1-x}$Ge$_x$ virtual substrate are fully relaxed.

Fig. 5.7 is a typical Raman spectrum obtained from the sample with the 325 nm UV laser excitation. A sharp Raman peak at ~510.9 cm^{-1} is observed in this spectrum. A corresponding strain free Si Raman spectrum is also included in the inset of Fig. 5.7. The calculated penetration depths for the 325 nm laser light in Si
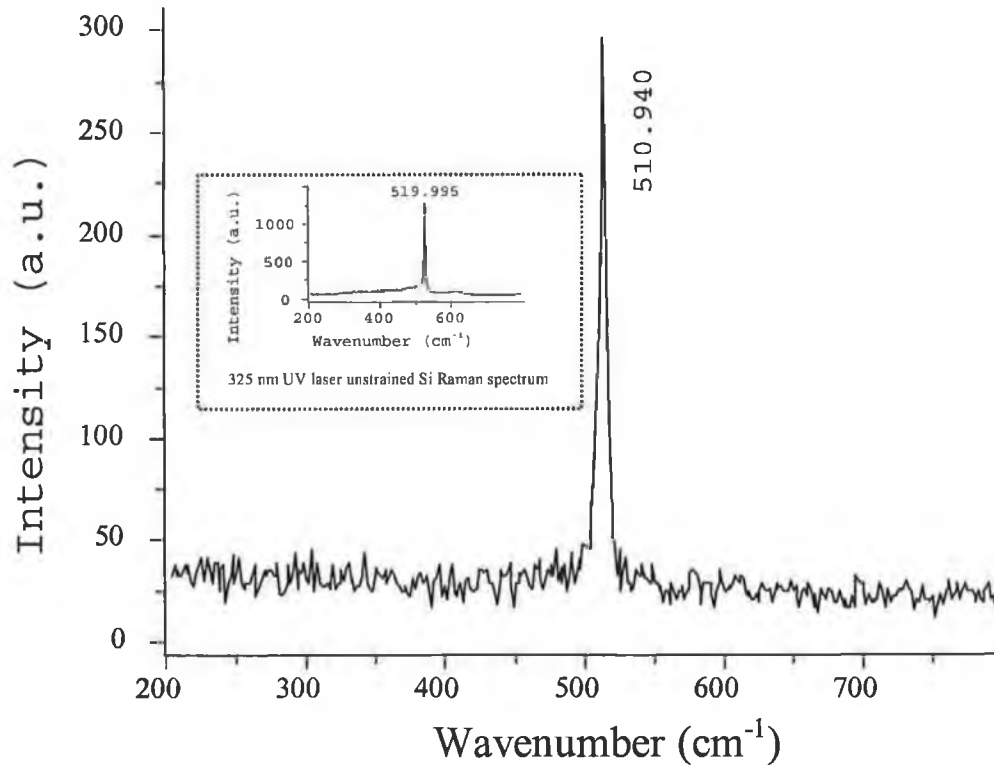

Figure 5.7 Typical Raman spectrum of the sample with the 325 nm UV laser. The Raman peak position is fitted with a Gauss/Lorentz function.

and Ge crystals are also listed in Table 5.1. Table 5.1 shows that the penetration depth of 325 nm wavelength light in Si is estimated to be 9 nm, which means that only the top surface of the sample contributes to the UV laser Raman signal, i.e. most of the Raman signal in Fig. 5.7 comes from the top Si cap layer. Thus, only the Si Raman signal from the Si cap layer was detected. The measured Si Raman peak position at ~510.9 cm^{-1} supports our previous assertion that the weak peak at ~510.7 cm^{-1} in Fig. 5.6 is the Si Raman signal from the top Si device layers. The Si Raman peak position of the top Si cap layer shifts to a much lower position when compared to that of the strain free Si sample, which is usually located around 520 cm^{-1} as indicated in the inset of Fig. 5.7. This large downward shift of the Si Raman peak position, $\Delta\omega_{Si_{UV}}$ with the UV laser (or $\Delta\omega_{Si}$ with the visible laser), of the device cap layer indicates an extremely high tensile stress in this layer. The average $\Delta\omega_{Si_{UV}}$ value obtained in the line scan, which is composed of 30 spectra, in this study is 9.53 cm^{-1}. This average $\Delta\omega_{Si}$ value obtained with the 488 nm laser data in the aforementioned area scan is 9.70 cm^{-1}, also very close to the UV laser result. By applying the relationship between the UV Si Raman peak position shift $\Delta\omega_{Si_{UV}}$ and the in-plane biaxial stress σ_{xx} and σ_{yy} [7], which is expressed in (4.17), the tensile stress in the Si cap layer is estimated to 2.38 GPa.

As seen from Fig. 5.5, the device layers are much thinner than the Si substrate. In the case of a fully strained Si cap layer, the tensile stress σ_f in the Si cap can be estimated with the following equation [40]:

$$\sigma_f = Y_f \, m/(1-v) \tag{5.3}$$

where Y_f is the film Young's modulus, m is the misfit between the film and the substrate lattice parameters and v is Poisson's ratio of the film. As the $Si_{0.70}Ge_{0.30}$ virtual substrate capping layer is fully relaxed, its lattice parameter (not the parameter of Si) should be used in the misfit calculation. The lattice parameters of Si and Ge are 0.543089 nm and 0.565754 nm respectively [41]. The lattice parameter for the fully relaxed $Si_{0.70}Ge_{0.30}$ virtual substrate capping layer is estimated to be 0.549889 nm according to Vegard's Law. So the misfit between the Si cap layer and the substrate is about 1.25%. The Young's modulus and Poisson's ratio for the Si crystal are 130.2 GPa and 0.28, respectively [42]. Thus the tensile stress for a fully strained Si cap layer is estimated to be 2.26GPa, which is very close to the tensile

stress in this layer measured in this study. This suggests strongly that the Si cap layer in the studied sample is fully strained.

References

1. K. Hiramatsu, J. Phys.: Condens. Matter. **13**, 6961 (2001).

2. W.M. Chen, P.J. McNally, K. Jacobs, T. Tuomi, A.N. Danilewsky, Z.R. Zytkiewicz, D. Lowney, J. Kanatharana, L. Knuuttila, J. Riikonen, J. Cryst. Growth, **243**, 94 (2002).

3. W.M. Chen, P.J. McNally, K. Jacobs, T. Tuomi, A.N. Danilewsky, D. Lowney, J. Kanatharana, L. Knuuttila, J. Riikonen, Mat. Res. Soc. Symp. Proc., **693**, 141 (2002).

4. P. Fini, H. Marchand, J. P. Ibbetson, S. P. DenBaars, U. K. Mishra, J. S. Speck. J. Cryst. Growth, **209**, 581 (2000).

5. W.M. Chen, G.D.M. Dilliway, P.J. McNally, T. Tuomi, A.F.W. Willoughby, J. Bonar, J. Mater. Sci. - Mater. Electron, **14**, 455 (2003).

6. M. Kuball, M. Benyoucef, B. Beaumont, P. Gibart, J. Appl. Phys. **90**, 3656 (2001).

7. I. De Wolf, Semicond. Sci. Technol. **11**, 139 (1996).

8. V.Yu. Davydov, N.S. Averkiev, I.N. Goncharuk, D.K. Nelson, I.P. Nikitina, A.S. Polkovnikov, A.N. Smirnov, M.A. Jacobson, O.K. Semchinova, J. Appl. Phys. **82**, 5097 (1997).

9. P. Perlin, C. Jauberthie-Carillon, J.P. Itie, A. San Miguel, I. Grzegory, A. Polian, Phys. Rev. B **45**, 83 (1992).

10. M. Holtz, M. Seon, T. Prokofyeva, H. Temkin, R. Singh, A. Chin, Appl. Phys. Lett. **75**, 1757 (1999).

11. Z.R. Zytkiewicz Thin Solid Films **412**, 64 (2002).

12. T.S. Zheleva, W.M. Ashmawi, Nam. Ok-Hyun, R.F. Davis, Appl. Phys. Lett. **74**, 2492 (1999).

13. Q. Liu, A. Hoffmann, A. Kaschner, C. Thomsen, J. Christen, P. Veit, R. Clos, Jpn. J. Appl. Phys., Part 2 **39**, L958 (2000).

14. M. Benyoucef, M. Kuball, G. Hill, M. Wisnom, B. Beaumont, and P. Gibart, Appl. Phys. Lett. **79**, 4127 (2001).

15. F. Bertram, T. Riemann, J. Christen, A. Keschner, A. Hoffmann, C. Thomsen, T. Shibata, N. Sawaki, Appl. Phys. Lett. **74**, 359 (1999).

16. A. Kaschner, A. Hoffmann, C. Thomsen, F. Bertram, T. Riemann, J. Christen, K. Hiramatsu, T. Shibata, N. Sawaki, Appl. Phys. Lett. **74**, 3320 (1999).

17. W.M. Chen, P.J. McNally, K. Jacobs, T. Tuomi, J. Kanatharana, D. Lowney, L. Knuuttila, J. Riikonen, J. Toivonen, J. Mater. Sci. - Mater. Electron, **14**, 283 (2003).

18. European commission, directorate general science, research and development, EUR 18595, "Raman and Luminescence Spectroscopy for Microelectronics".

19. S. Jain, M. Willander, R Van Overstraeten, Compound Semiconductors Strained layers and Devices (Electronic materials Series) (Boston: Kluwer), 2000.

20. S.C. Jain, S. Decoutere, M. Willander, H.E. Maes, Semicond. Sci. Technol. **16**, R51 (2001).

21. G. Dilliway, PhD Thesis, University of Southampton, 2002.

22. M.T. Currie, C.W. Leitz, T.A. Langdo, G. Taraschi, E.A. Fitzgerald, D.A. Antoniadis, J. Vac. Sci. Technol. B, **19**, 2268 (2001) and references therein.

23. S.B. Samavedam, W.J. Taylor, J.M. Grant, J.A. Smith, P.J. Tobin, A. Dip, A.M. Phillips, R. Liu, J. Vac. Sci. Technol. B, **17**, 1424 (1999).

24. C.K. Maiti, L.K. Bera, S. Chattopadhyay, Semicond. Sci. Technol. **13**, 1225(1998)

25. Ismail, K., J. Vac. Sci. Technol. **B14**, 2776 (1996).

26. Beam III, E. A., Temkin, H. and Mahajan, S., Semicond. Sci. Technol., **7**, A229 (1992).

27. G. Wöhl, V. Dudek, M. Graf, H. Kibbel, H.-J. Herzog, M. Klose, Thin Solid Films, **369**, 175 (2000), and reference therein.

28. W.S. Wang, J.B. Bhat, J. Electron mater. **24**, 1047 (1995).

29. Y.H. Luo, J.L. Liu, G. Jin, J. Wan, K.L. Wang, C.D. Moore, M.S. Goorsky, C. Chih, K.N. Tu, Appl. Phys. Lett., **78**, 1219 (2001), and reference therein.

30. E.A. Fitzgerald, Y.H. Xie, M.L. Green, D. Brasen, A.R. Kortan, J. Michel, Y.J. Mii, B.E. Weir, Appl. Phys. Lett., **59**, 811 (1991).

31. B. Hollander, St. Lenk, S. Mantl, H. Trinkaus, D. Kirch, M. Luysberg, T. Hackbarth, H.-J. Herzog, P.F.P. Fichtner, Nucl. Instr. ans Meth. B **175-177**, 357 (2001).

32. J. Lu, D. Retraint. J. Strain Anal. Eng. Des. **33**, 127 (1998).

33. D. Buttard, D. Bellet, G. Dolino, J. Appl. Phys. **79**, 8060 (1996).

34. A. Armigliato, R. Balboni, A. Benedetti, S. Frabboni, A. Tixier, J. Vanhellemont J. Phys. III, **7**, 2375 (1997).

35. J. Yuan, J.W. Corbett, S.N. Voronkov, I.V. Verner, Radiat Eff. Defects Solids, **125**, 275 (1993).

36. T. Okuyama, M. Nakayama, Y. Tomokiyo, O. Van der Biest, Microsc. Microanal. **8**, 11 (2002).

37. J. Demarest, R. Hull, K.T. Schonenberg, K.G.F. Janssens, Appl. Phys. Lett. **77**, 412 (2000).

38. C.H. Perry, L. Feng, F. Namavar, Solid State Commun. **88**, 613(1993)

39. M.I. Alonso, K. Winer, Phys. Rev. B **39**, 10056(1989).

40. B. Pichaud, M. Putero, N. Burle, Phys. Stat. Sol. (A), **171**, 251(1999)

41. E.K. Liu, B.S. Zhu, J.S. Luo, Physics of semiconductor, Chinese Defence Technology Press, 1995

42. S.C. Jain, K. Pinardi, H.E. Maes, R. Van Overstraeten, M. Willander, Semicond. Sci. Technol. **13**, 864(1998)

6 Conclusion

In this study, non-destructive white beam synchrotron X-ray topography and high resolution micro-Raman spectroscopy (μRS) are used to characterize three types of crystal materials, i.e. sapphire, epitaxial lateral overgrowth (ELO) of GaN over a sapphire substrate and Si/SiGe on $Si_{1-x}Ge_x$ virtual substrates. For the X-ray topography technique, both transmission and back reflection methods in either large area or section modes are employed; for the high resolution micro-Raman spectroscopy, two laser sources (488 nm Ar^+ blue laser and a 325 nm HeCd UV laser) are used. Information about the general wafer quality, Burgers vectors of dislocations, crystal misorientation in the ELO GaN epilayer and the stress in the $Si_{1-x}Ge_x$ virtual substrate and the overlying Si device layers, etc. are obtained in this study. The conclusions for each kind of material are listed as follows:

(1) SAPPHIRE WAFERS:

Overall, the sapphire wafers measured in this study are of good quality. Discrete dislocation lines have been discerned in all samples, which implies that the dislocation density in the wafer is below 10^5 cm^{-2} or thereabouts.

Sapphire wafers grown with the HEM method have fewer dislocations compared with the sapphire wafers grown with the MCM method. In some regions of the HEMEX samples, no dislocations were detected. For a typical MCM wafer the dislocation density near the centre was found to be higher than that near the edge. The highest dislocation density is about 9.0×10^4 cm^{-2}.

The Burgers vectors for dislocations in high quality (0001) HEM sapphire wafers are analysed. Most dislocations in the HEM sapphire can be identified unambiguously in one exposure with the white beam synchrotron X-ray topography technique. For the samples measured in this study, most of the dislocations in the sapphire possess Burgers vectors which belong to the two groups of $<2\,\bar{1}\,\bar{1}\,0>$ and $<1\,0\,\bar{1}\,0>$. Three types of dislocations, i.e. screw, edge and mixed dislocations are found in the HEM sapphire, but most are of mixed type.

Stacking faults represent another common defect in the sapphire wafers, they exist in most samples, even in regions with no dislocation lines.

Pendellösung fringes are found in many samples even with numerous stacking faults, which indicates that the overall crystal quality is high, despite the presence of these stacking faults.

The reflectivity of sapphire X-ray optics is affected by its quality. With an increase of the dislocation density, its reflectivity decreases.

(2) EPITAXIAL LATERAL OVERGROWTH OF GaN:

The low quality of the GaN buffer due to its high lattice misfit to the substrate and tilting of ELO wings due to their interaction with the underlying mask were simultaneously observed within a single white beam synchrotron X-ray topographic image of the sample. The wing tilt was determined by measuring the length of streaks observed in the section topographs. An increase of the GaN wing tilt with an increase of the fill factor and wing tilt asymmetry for all fill factors were found in this study. The WBSXT method gives the maximum wing tilt in the measured samples and its measured results are confirmed by the X-ray rocking curve method. The average wing tilt reaches approximately 1600 arcsec measured using the X-ray rocking curve method at a fill factor of 0.625, but the maximum wing tilts can reach values as large as 2400 arcsec measured by SXRT when the fill factor is only 0.571. The crystallographic misorientation in the window region and the seed GaN was found to be not as serious as that in the wing region, being approximately one tenth of the wing tilt. The sapphire substrates used for the growth of ELO GaN in this study are not relatively very high quality, the dislocation density being $\sim 10^6 \text{cm}^{-2}$.

A regular two dimensional wave-like stress distribution was observed in the ELO GaN epilayer via micro-Raman spectroscopy. An average compressive stress of about 450~460 MPa was observed in the ELO GaN epilayer. The ELO GaN coalesced regions usually exhibit a lower compressive stress by about 60 MPa compared to the average stress in the ELO GaN epilayer. The ELO process increases the compressive stress in the GaN epilayer.

(3) Si/SiGe ON THE $Si_{1-x}Ge_x$ VIRTUAL SUBSTRATE:

The $Si/Si_{0.70}Ge_{0.30}/Si_{1-x}Ge_x$ system measured in this study reveals a fully relaxed $Si_{1-x}Ge_x$ virtual substrate with the formation of two perpendicular <110> misfit crosshatches, while the top Si device layers are fully strained. Both the visible and UV laser micro-Raman spectroscopy measurements exhibit similar results. The

tensile stress in the top Si device layers is as large as 2.4 GPa. The step grade of Ge combined with the LPCVD technique proved to be an effective method in making excellent $Si_{1-x}Ge_x$ virtual substrates.

POSSIBLE FUTURE RESEARCH DIRECTIONS FOR THIS PROJECT:

Correlations between sapphire wafer quality and sapphire crystal manufacturing processes enable us to learn more about the origin of defects in sapphire crystal materials. Thus higher quality sapphire wafers can be produced. These efforts can be continued through cooperation with crystal manufacturers, such as Crystal System Inc.

For the ELO GaN epilayer, the effects of different mask materials and process parameters, such as temperature, pressure, etc. on the wing tilts require further study to improve the epilayer quality.

The critical thickness measurement for the Si device layers over $Si_{1-x}Ge_x$ virtual substrates with the μRS is an interesting and useful area; correlations between the stress relaxation and different process parameters may provide useful information for the development of high quality $Si/Si_{0.70}Ge_{0.30}/Si_{1-x}Ge_x$ materials systems.

APPENDIX A:

Refereed journal publication from this research

1. W.M. Chen, P.J. McNally, Yu.V. Shvyd'ko, T. Tuomi, M. Lerche, A.N. Danilewsky, J. Kanatharana, D. Lowney, M. O'Hare, L. Knuuttila, J. Riikonen, R. Rantamäki, *phys. status solidi (a)*, **186,** 365 (2001).
2. W.M. Chen, P.J. McNally, K. Jacobs, T. Tuomi, A.N. Danilewsky, Z.R. Zytkiewicz, D. Lowney, J. Kanatharana, L. Knuuttila, J. Riikonen, *J. Cryst. Growth*, **243,** 94 (2002).
3. W.M. Chen, P.J. McNally, K. Jacobs, T. Tuomi, A.N. Danilewsky, D. Lowney, J. Kanatharana, L. Knuuttila, J. Riikonen, *Mat. Res. Soc. Symp. Proc.*, **693,** 141 (2002).
4. W.M. Chen, P.J. McNally, Yu.V. Shvyd'ko, T. Tuomi, A.N. Danilewsky, M. Lerche, *J. Cryst. Growth*, **252,** 113 (2003).
5. W.M. Chen, G.D.M. Dilliway, P.J. McNally, T. Tuomi, A.F.W. Willoughby, J. Bonar, *J. Mater. Sci. - Mater. Electron.,* **14,** 455 (2003).
6. W.M. Chen, P.J. McNally, K. Jacobs, T. Tuomi, J. Kanatharana, D. Lowney, L. Knuuttila, J. Riikonen, J. Toivonen, *J. Mater. Sci. - Mater. Electron.,* **14,** 283 (2003).
7. J Toivonen, T Tuomi, J Riikonen, L Knuuttila, T Hakkarainen, M Sopanen, H Lipsanen, PJ McNally, W Chen, D Lowney, *J. Mater. Sci. - Mater. Electron.,* **14,** 267 (2003).
8. J. Kanatharana, J.J. Pérez-Camacho, T. Buckley, P.J. McNally, T. Tuomi, A.N. Danilewsky, M. O'Hare, D. Lowney and W. Chen, *Mat. Res. Soc. Symp. Proc.,* **682E,** 2002
9. J Kanatharana, J J Pérez-Camacho, T Buckley, P J McNally, T Tuomi, J Riikonen, A N Danilewsky, M O'Hare, D. Lowney, W. Chen, R Rantamäki, L Knuuttila, *Semicond. Sci. Technol.* **17,** 1255 (2002).
10. T. Tuomi, L. Knuuttila, J. Riikonen, P.J. McNally, W.M. Chen, J. Kanatharana, M. Neubert, P. Rudolph, *J. Cryst. Growth*, **237-239,** 350 (2002).
11. J. Kanatharana, J. J. Pérez-Camacho, T. Buckley, P. J. McNally, T. Tuomi, A. N. Danilewsky, M. O'Hare, D. Lowney, W. Chen, R. Rantamäki, L. Knuuttila, J. Riikonen, *Microelectron. Eng.,* **65,** 209 (2002).

APPENDIX B:

Award received from this research

3rd placed best poster for **"Stress characterization of device layers and the underlying $Si_{1-x}Ge_x$ virtual substrate with high resolution micro-Raman spectroscopy"**, W.M. Chen, G.D.M. Dilliway, P.J. McNally, T. Tuomi, A.F.W. Willoughby and J. Bonar, at the *4th Int. Conf. on Materials for Microelectronics & Nanoengineering (MFMN2002)*, Helsinki, Finland, June, 2002.